

MICRO-MECHANICAL MODELING OF BROWNIAN SPHEROIDS IN OSCILLATORY SHEAR FLOW

Submitted in partial fulfillment of the requirements for the degree of

Doctor of Philosophy
in
Chemical Engineering

Toni M. Bechtel

B.S., Chemical Engineering, The Pennsylvania State University

Carnegie Mellon University
Pittsburgh, PA

May 2018

© Toni M. Bechtel, May 2018
All Rights Reserved

Acknowledgements

I would like to thank my thesis adviser, Aditya Khair, whose constant support, guidance, and positive demeanor were most helpful and appreciated. Over these past few years, he has helped me to become a better researcher and greatly improve my communication skills. I would also like to thank my thesis committee, Shelley Anna, Stephen Garoff, and Lynn Walker, for their insight and help in my thesis proposal and defense.

During my time at Carnegie Mellon and in Pittsburgh, I have made some amazing friends who made pursuing my PhD a more enjoyable experience, both academically and personally. Specifically, I'd like to thank Sarah, Nicholas, Javier, Ben, and Rob, all previous group members. Their help in endlessly listening to my many practice presentations and simply chatting in the office were greatly beneficial. I'd also like to thank Kevin, whose superior computer knowledge helped me to complete some of my numerical calculations toward the end of my thesis. I'd like to thank the many great friends I have made in Pittsburgh, specifically, Alex, Nick, Khalid, Brittany, Travis, Blake, Emily, Sarah, and Yuan, for supporting me, and each other, and always finding a way to make every moment fun and memorable.

I would also like to thank my family for their support and encouragement through my many years of education, especially my mother, whose ability to endure some of life's greatest hardships, with a smile on her face, has been a true inspiration. And last, but not least, I would like to thank Nicholas Surdyka for his unwavering love, support, and laughs, which made this journey possible.

Funding

I acknowledge financial support from the Camille Dreyfus Teacher-Scholar Award Program. Additionally, I received two fellowships while working on this thesis, the PPG Graduate Fellowship in Chemical Engineering and the John and Claire Bertucci Graduate Fellowship in Engineering.

Abstract

We calculate the stress response, or rheology, of a micro-mechanical model suspension of rigid, Brownian spheroids in a Newtonian fluid in an oscillatory shear flow. The straining and rotation components of a linear flow affects the microstructure, or particle orientation in space and time, and thus, the suspension stress. A statistical description of the microstructure is given by an orientation probability distribution function, which quantifies the likelihood of a particle possessing a particular orientation at an instance in time. The evolution of the microstructure results from the memory of the material, advection from the flow, and rotational Brownian motion. The macroscopic stress response is calculated from ensemble averages of the stresslet weighted by the orientation distribution function. First, we calculate the linear stress response of a dilute suspension of rigid, spheroidal, self-propelled particles under a small-amplitude oscillatory shear deformation using regular perturbation theory. The particle activity leads to a direct contribution to the material stress, via self-propulsion, and an indirect contribution due to correlated tumbling events. The mechanism and strength of self-propulsion and correlation between tumbling events can be determined from the linear stress response of an active suspension. Next, we develop a framework for determining the relaxation moduli of a viscoelastic material through the combination of a memory integral expansion and a multimode-frequency oscillatory shear flow. We analytically determine the first nonlinear relaxation modulus of the model suspension through a comparison of the second normal stress difference from the microstructural stress response, calculated via regular perturbation theory, and a co-rotational memory integral expansion. The stress response of the system is reconstructed for the start-up and cessation of steady simple shear and uniaxial extension. Finally, we numerically calculate the nonlinear viscoelasticity of the model system subject to a large-amplitude oscillatory shear flow. In a sufficiently strong flow with oscillation frequency comparable to the material relaxation rate, secondary overshoots in the stress response occur. We attribute the origin of secondary overshoots to particles undergoing a Jeffery orbit during a (half) cycle of the oscillation, analogous to the case of non-Brownian spheroids in steady shear flow.

Table of Contents

List of Figures	vii
List of Tables	ix
1 Introduction	1
2 Linear Viscoelasticity of a Dilute Suspension of Active Particles	9
2.1 Introduction	9
2.2 Governing Equations	12
2.3 Asymptotic Expansion for Linear Viscoelasticity	14
2.4 Linear Viscoelasticity	16
2.5 Comparison to Previous Work	22
2.5.1 Steady shear of active, slender rods ($r \rightarrow \infty$)	22
2.5.2 Experimental results for suspensions of <i>E. coli</i>	24
2.6 Summary	27
3 Nonlinear Relaxation Modulus via Dual-Frequency Medium Amplitude Oscillatory Shear	29
3.1 Introduction	29
3.2 Memory Integral Expansion and Nonlinear Viscoelasticity	32
3.3 General Framework	39
3.3.1 Co-rotational Memory Integral Expansion for Dual-Frequency MAOS	39
3.3.2 Micromechanics of a Dilute Suspension of Rigid Spheroids	41
3.3.3 Determining the Relaxation Moduli	47
3.4 Prediction of Nonlinear Stress Response from MAOS Relaxation Modulus	50
3.4.1 Start-up and Cessation of Simple Shear Flow	51

3.4.2	Start-up and Cessation of Uniaxial Extensional Flow	53
3.5	Discussion	55
3.A	Appendix	59
3.A.1	Coefficients of N_2 from the co-rotational memory integral expansion	59
3.A.2	Frequency-dependent coefficients of ψ_2	61
3.A.3	Two-dimensional inverse Fourier cosine transform to determine G_{II}	63
4	Nonlinear Viscoelasticity of a Dilute Suspension of Brownian Spheroids in Oscillatory Shear	66
4.1	Introduction	66
4.2	Micro-mechanical Model	72
4.2.1	Problem setup	72
4.2.2	Oscillatory Shear Flow	78
4.3	Numerical Solution Method	82
4.4	Results	86
4.4.1	Linear viscoelastic response: $Wi \ll 1$	87
4.4.2	Quasi-linear Response: $Wi > 1, Wi/De \ll 1$	90
4.4.3	Quasi-steady response: $De \rightarrow 0$	92
4.4.4	Nonlinear Viscoelastic Response, $Wi \gtrsim 1$ and $Wi/De \gtrsim 1$	95
4.5	Discussion	100
4.A	Appendix	107
4.A.1	Expressions for normal stress differences and birefringence parameters	107
4.A.2	Convergence and Condition of Numerical Solution Method	109
5	Summary	112
5.1	Future Work	114
	References	116

List of Figures

1.1	Schematic of prolate and oblate spheroid	1
1.2	Viscoelastic phase map of the $Wi - De$ space	4
2.1	Effect of correlated tumbling on the viscous and elastic complex viscosities	18
2.2	Schematic of the stresslet for a prolate spheroid in steady shear flow for puller and pusher self-propulsion mechanisms	21
2.3	Viscous and elastic complex viscosities for a dilute suspension of active prolate spheroids ($r = 3$)	22
2.4	Viscous and elastic complex viscosities for a dilute suspension of active oblate spheroids ($r = 0.25$)	23
2.5	Cox-Merz rule for active suspensions	24
2.6	Comparison of the linear viscoelasticity of a suspension of pushers to experimental measurements of the steady shear viscosity of <i>E. coli</i>	25
3.1	Sketch of velocity streamlines for steady shear flow in a fixed and co-rotational frame of reference.	33
3.2	MAOS relaxation modulus of a dilute suspension of Brownian rods ($B = 1$) in the frequency and time-domain	49
3.3	Second normal stress difference for a dilute suspension of rigid rods ($B = 1$) and rigid disks ($B = -1$) subject to a start-up and cessation of simple shear flow.	53

3.4	Extensional viscosity for a dilute suspension of rigid rods ($B = 1$) and rigid disks ($B = -1$) subject to a start-up and cessation of uniaxial extensional flow.	55
4.1	General schematic of the stress response of a material in the $Wi - De$ parameter space	71
4.2	Definition of spherical coordinates	74
4.3	Jeffery orbits for prolate and nearly-spherical particles	75
4.4	Pipkin diagram: Lissajous curves of hydrodynamic and Brownian shear stress contributions over a range of Wi and De	87
4.5	Non-equilibrium orientation distribution in the linear viscoelastic regime	89
4.6	Hydrodynamic and Brownian shear stress, orientation angle, and linear dichroism in the linear viscoelastic regime	90
4.7	Non-equilibrium orientation distribution function in the quasi-linear viscoelastic regime	91
4.8	Hydrodynamic and Brownian shear stress, orientation angle, and linear dichroism in the quasi-linear viscoelastic regime	92
4.9	Non-equilibrium orientation distribution function in the quasi-steady viscoelastic regime	94
4.10	Hydrodynamic and Brownian Stress, orientation angle, and linear dichroism in the quasi-steady viscoelastic regime	95
4.11	Non-equilibrium orientation distribution function in the non-linear viscoelastic regime	98
4.12	Normalized shear stress as a function of time and normalized strain-rate	99

4.13	Lissajous plots of shear stress, first normal stress difference, orientation angle, and linear dichroism	100
4.14	Microstructural origins of stress over-shoot: non-equilibrium orientation distribution function, shear stress, first normal stress difference, orientation angle, linear dichroism, for $Wi = 20$ and $De = 1$	105
4.15	Microstructure for prolate ($r = 20$) and oblate ($r = 0.05$) spheroids at $Wi = 10$ and $De = 1$	106
4.16	Hydrodynamic and Brownian shear stress for prolate ($r = 20$) and oblate ($r = 0.05$) spheroids at $Wi = 10$ and $De = 1$	106
4.17	Solution methodology for accessing the $Wi - De$ parameter space	110
4.18	Condition number as a function of De at $Wi = 10$	111

List of Tables

2.1	Volume fraction-dependent self-propulsion parameters of <i>E. coli</i>	27
3.1	Viscometric functions for steady shear, planar extension, and uniaxial extension flows, as determined from a co-rotational memory integral expansion	35

1. Introduction

The central theme of this thesis is to calculate the stress response, or rheology, of a micro-mechanical model suspension of a monodisperse, rigid, Brownian spheroidal particles in a Newtonian fluid subject to an oscillatory shear flow. This is accomplished through a combination of perturbation theory and numerical computation. The particles are force- and torque-free, and the suspension is assumed dilute such that hydrodynamic interparticle interactions can be neglected. We also assume that the Reynolds number, defined by the size of a particle, is vanishingly small; thus, the Stokes equations describe the disturbance to the ambient flow caused by a particle. A spheroidal particle is characterized by a symmetry (major) axis of length 2ℓ , and two equivalent semi-axes of length $2a$; the ratio of the length of the major to semi-axis is the aspect ratio, $r = \ell/a$. Prolate spheroids have $r > 1$, whereas oblate spheroids have $r < 1$ (Figure 1.1); nearly-spherical particles are defined as $r \approx 1$. This micro-mechanical model system is relevant as many suspensions are comprised of non-spherical, (roughly) axisymmetric particles¹, such as glass fibers², actin filaments³, and kaolin clay⁴. Furthermore, for particles of (effectively) infinite aspect ratio ($r \rightarrow \infty$), this micro-mechanical model reduces to the rigid dumbbell model used in polymer kinetic theory, which has been studied extensively⁵⁻⁸.

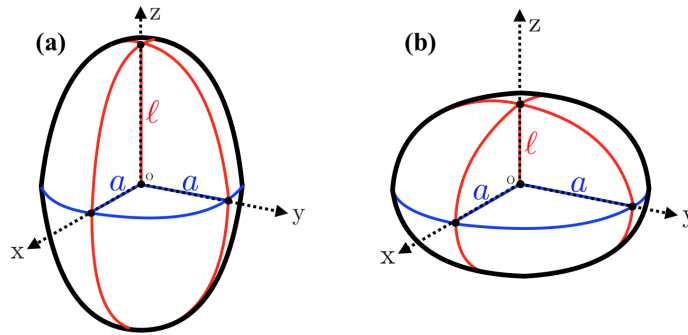


Figure 1.1: Schematic of (a) prolate ($r > 1$) and (b) oblate spheroid ($r < 1$). The aspect ratio of a spheroid is the ratio of the major (symmetry) axis to the minor axis, $r = \ell/a$.

In a linear flow field, a non-spherical particle is effected by both the straining and vorticity components of the flow. The straining component of the flow acts to align the particle along the principal axes of strain, whereas the vorticity component of the flow acts to rotate the particle.

Here, we are considering rigid particles that are unable to stretch or deform, which leads to a force dipole (stresslet) exerted by the particle onto the fluid, affecting the stress of the suspension. The imposed flow, however, cannot orient spherical particles and they will simply translate with the flow and rotate at half the ambient vorticity. Jeffery⁹ determined (analytically) that the orientation of a non-Brownian spheroidal particle, characterized by an orientation unit vector, \mathbf{p} , in a steady shear flow will rotate indefinitely along a closed path that traces the surface of a unit sphere, referred to as a Jeffery orbit. The specific orbit a particle traces is dependent upon its initial orientation. However, most colloidal suspensions are comprised of sufficiently small particles that are affected by random thermal collisions with solvent molecules, and are thus subject to Brownian forces and torques. The model suspension is homogeneous and thus translational Brownian motion does not impact the overall material stress. Rotational Brownian motion acts to randomize the microstructure of the suspension, and has a direct contribution to the stress. This leads to a steady orientation probability distribution, and steady stress, for axisymmetric particles in a steady shear flow^{10,11}.

With the inclusion of rotational Brownian motion, the orientation of a particle is no longer deterministic and a statistical description of the microstructure, which refers to the spatio-temporal orientation evolution, is required. We describe the microstructure of the suspension as an ensemble via an orientation probability distribution function, $\psi(\mathbf{p}, t)$, which quantifies the relative likelihood of a particle oriented along \mathbf{p} at a given time, t ¹². The orientation probability distribution function satisfies the Fokker-Planck equation, which is a conservation equation that balances the effects of the memory of the material, advection arising from the imposed flow, and relaxation via rotational Brownian motion^{6,12,13}. The particle contribution to the stress of the suspension is determined from the moments of the orientation probability distribution function^{12,14,15}. Thus, from a statistical description of the microstructure we can calculate the macroscopic stress response of the model micro-mechanical suspension.

Most complex fluids, including suspensions of rigid, anisotropic particles, are viscoelastic, meaning that they simultaneously exhibit viscous (liquid-like) and elastic (solid-like) characteristics when deformed. Quantifying the viscoelasticity of a material over varied types and rates

of deformations is important, for instance, in polymer melt processing. A melt will pass through numerous processing operations, such as die extrusion or film blowing, all of which will involve different geometries and likely occur over varying time-scales¹⁶. Thus, an overarching goal of rheologists is to develop a general stress-strain relationship, or constitutive equation, for a material, which quantifies viscoelasticity, such that the behavior of the material is predictable over a wide range of conditions (i.e. flow type/geometry and flow strength). A common method of characterizing the viscoelasticity of a material is to subject it to an oscillatory simple shear flow and calculate (or measure) the stress response of the material¹⁷. Here, the material is subjected to a sinusoidal strain, $\gamma = \gamma_0 \sin(\omega t)$, where γ_0 is the strain amplitude, ω is the oscillation frequency, and t is time. An experimental advantage of oscillatory shear rheology is that one can average the measured response over multiple oscillation cycles, mitigating experimental noise associated with the start-up or cessation of a flow.

The magnitude of the strain amplitude indicates the extent of the deformation. In general, when $\gamma_0 \ll 1$ the material is subjected to a small deformation and only slightly shifted out of equilibrium. Conversely, when $\gamma_0 \gg 1$, the material is undergoing a large deformation and is likely far from equilibrium. In experimental work, the strain amplitude is typically reported as a percentage as opposed to a fraction; for example, $\gamma_0 = 0.5 = 50\%$. There are two relevant time scales for this type of deformation: the oscillation time scale, $1/\omega$, and the flow time scale, $1/\dot{\gamma}_0$, where $\dot{\gamma}_0 = \omega\gamma_0$ is the strain-rate amplitude. Here the strain-rate is, $d\gamma/dt \equiv \dot{\gamma} = \dot{\gamma}_0 \cos(\omega t)$. From these time scales, two dimensionless groups can be formed: a Weissenberg number, $Wi = \dot{\gamma}_0\lambda$, and a Deborah number, $De = \omega\lambda$, where $1/\lambda$ is a characteristic rate of relaxation of a material. The strain-amplitude is then given by, $\gamma_0 = Wi/De$. Most materials have a spectrum of relaxation rates, the smallest being the most relevant for the long-time rheological response. For simplicity, we assume a single relaxation time.

Wi is the ratio of the rate of deformation to the rate of relaxation within a material. For $Wi \ll 1$, the rate of deformation is small relative to the intrinsic material relaxation rate, and the material remains in a near-equilibrium state; this regime is typically referred to as the linear

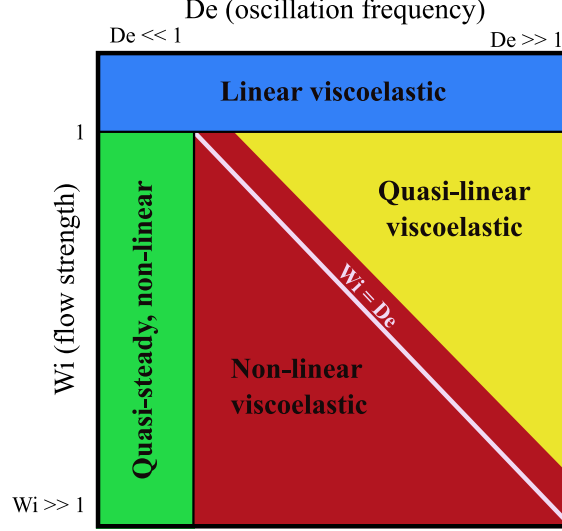


Figure 1.2: Viscoelastic phase map of the $Wi-De$ space for a general complex fluid, such as a colloidal suspension or polymer solution. This generalization, for example, would likely not apply to a liquid-crystalline material, which is non-isotropic at rest, or yield-stress fluid, which only deforms about a critical stress.

viscoelastic regime. For $Wi \gg 1$, the rate of deformation is large relative to the rate of relaxation of the material, and the material is shifted far from equilibrium. De is the ratio of the frequency of an oscillation cycle to the rate of relaxation within the material. For $De \ll 1$, the oscillation frequency is much less than the rate of relaxation of the material, and the deformation is quasi-steady; $De \equiv 0$ is equivalent to a steady shear deformation. For $De \gg 1$, the oscillation frequency is much greater than the rate of relaxation of the material. In this limit, the imposed flow oscillates so rapidly that the material is not given sufficient time to deform, leaving the material in a near-equilibrium state. However, when $De \sim O(1)$, the oscillation frequency is comparable to the rate of relaxation of the material and the unsteady viscoelasticity of the material is probed. A general viscoelastic phase map of the $Wi - De$ parameter space is given in Figure 1.2.

Under a small amplitude oscillatory shear (SAOS) deformation, $Wi \ll 1$, the linear viscoelasticity of a material is probed over a range of De . Here, the shear stress, τ_{yx}^{SAOS} , is linear in the strain-rate amplitude (and also the strain amplitude) and has a frequency-dependent component in-phase and out-of-phase with the imposed flow,

$$\tau_{yx}^{\text{SAOS}} = \dot{\gamma}_0 \left[\eta'(De) \cos(De t) + \eta''(De) \sin(De t) \right], \quad (1.1)$$

where, η' is the viscous (dynamic) component of the complex viscosity and η'' is the elastic (loss) component of the complex viscosity. Higher order contributions (i.e. $O(Wi^2)$) to the stress, which would contribute to normal stress differences, are negligible. The linear relaxation modulus can then be determined from an inverse Fourier transform of either the viscous or elastic components of the complex viscosity. From the linear relaxation modulus, one can predict the linear viscoelastic response of the material under any *small* amplitude deformation, such as the start-up of steady shear or planar extensional flow. By probing the linear viscoelasticity of a material, one can determine, for example, the time-scale of stress relaxation or the time (frequency)-dependent configuration of the microstructure¹⁷. For instance, a dilute suspension of polymer molecules can be in a random-coil or rod-like configuration, giving rise to markedly different frequency-dependent components of the complex viscosity¹⁷. However, the linear relaxation modulus is incapable of predicting the nonlinear material stress response beyond the small Wi regime.

Having laid out a general introduction, we now proceed to describe the chapters of this thesis. Active, or self-propelled, particles, such as synthetic colloidal motors or biological microorganisms, have recently received much attention for their potential applications in micro- or nano-scale batteries, chemical and biological sensors, and drug delivery, to name a few¹⁸⁻²³. One question that naturally arises in these applications is: How does the activity of a self-propelled particle change the rheology of a material? Furthermore, what can the stress of an active suspension tell us about the individual particles? To address these questions, in Chapter 2²⁴, the linear viscoelasticity of a dilute suspension of active rigid spheroidal particles is calculated under a SAOS deformation. The microstructure relaxes via two independent mechanisms: rotational Brownian motion and correlated tumbling; the combination of which results in an increased rate of stress relaxation, relative to a suspension that relaxes solely by either mechanism. Tumbling is the act of a particle abruptly changing its orientation, which is fundamentally different from a change in orientation due to an imposed flow or rotary Brownian motion. We assume tumbling events are correlated, meaning that the change in orientation is dependent upon the previous orientation and any magnitude of change can occur; uncorrelated tumbling is restricted to 90° changes in orientation. We explicitly cal-

culate the non-equilibrium orientational microstructure due to the SAOS deformation, rotational diffusion, and tumbling. From this, we determine the linear viscoelasticity of the suspension from the orientationally averaged stresslet, which arises from the imposed flow, rotational diffusion, and particle activity (self-propulsion). Next, we demonstrate that a modified Cox-Merz rule is applicable to a dilute, active suspension via a comparison of our linear viscoelasticity results to a theoretical prediction of the steady shear viscosity of active, slender rods²⁵. Finally, through a comparison of our results to experiments on *E. coli*²⁶, we show that the linear viscoelasticity of an active suspension can be utilized to determine the mechanism of self-propulsion, and estimate the strength of self-propulsion and correlation between tumbling events.

Commonly, complex fluids are processed or utilized at conditions far from equilibrium, such as in polymer melt processing¹⁶, impact-resistant suits and armor^{27,28}, or chewing food²⁹. All of these instances involve deformations far beyond the linear viscoelastic regime. However, one cannot predict nonlinear phenomena, such as shear-rate dependent viscosity or normal stress differences, from linear viscoelasticity. Thus additional information about a material is required. One approach to modeling the nonlinear, transient stress response of a material is to employ a memory integral expansion, which expresses the stress response of a material as a series of integrals of the deformation history, which depend upon material-specific relaxation moduli³⁰. A memory integral expansion can be useful when probing the weakly nonlinear stress response of a material, where the stress response is asymptotic in Wi , as $Wi \rightarrow 0$. The first term in a memory integral expansion encodes the linear viscoelasticity of the material. The subsequent terms account for the weakly nonlinear material response, and we generally refer to the relaxation moduli in these terms as the nonlinear relaxation moduli. In Chapter 3³¹, a framework for determining the first nonlinear relaxation modulus of a viscoelastic fluid from a medium-amplitude oscillatory shear (MAOS) deformation is constructed. The MAOS regime is defined as by $Wi \ll 1$, where the shear stress scales as Wi and normal stress differences are non-zero and scale as Wi^2 . Knowledge of this “MAOS relaxation modulus” allows one to predict the weakly nonlinear stress response of a material under an arbitrary transient deformation via a memory integral expansion. Our framework

is demonstrated by explicitly determining the MAOS relaxation modulus for a dilute suspension of Brownian spheroids subject to a dual-frequency oscillatory shear flow. We first calculate the second normal stress difference for such a deformation from a co-rotational memory integral expansion. Second, the microstructural stress response of the model system of Brownian spheroids is determined via a regular perturbation expansion of the orientation probability distribution function for $Wi \ll 1$. An analytical expression for the MAOS relaxation modulus is resolved by comparing the second normal stress difference results of the memory integral expansion and microstructural stress calculation. Finally, using the MAOS relaxation modulus, we reconstruct the stress response of the model system for the start-up and cessation of simple shear and uniaxial extension. This framework offers an approach to utilizing medium-amplitude oscillatory shear results to predict nonlinear stress dynamics of viscoelastic fluids in other transient flows.

Large amplitude oscillatory shear (LAOS) has become a popular rheological tool for probing the transient, nonlinear viscoelasticity of material and has been applied to a variety of systems, such as polymer solutions^{16,32,33}, colloidal dispersions^{34–36}, and worm-like micelles^{37–40}. An advantage of LAOS is that one is able to discern microstructural differences between materials that may be unpronounced in the linear or weakly nonlinear viscoelastic regime. For instance, the linear viscoelastic and nonlinear steady shear response of a suspension of linear polystyrene and a suspension of star-branched polystyrene are nearly indistinguishable, even though their molecular architecture is quite different. However, the LAOS response of the two materials is markedly unique due to differences in the extent of branching and reptation⁴¹.

In Chapter 4 the nonlinear viscoelasticity of a dilute suspension of Brownian spheroids subject to a LAOS deformation is calculated numerically. This is achieved by solving the Fokker-Planck equation for the orientation probability distribution function using a numerical solution method that combines a finite-difference approximation in space and a Fourier series in time. From an ensemble average of moments of the orientation probability distribution function, the entire stress tensor and relevant birefringence parameters, namely the average orientation angle and linear dichroism, are calculated over a range of Wi and De . This approach is demonstrated for prolate spheroids of

aspect ratio $r = 20$; however, our methodology is general and can be applied to spheroids of arbitrary aspect ratio. We provide results in four viscoelastic regimes: linear viscoelastic ($Wi \ll 1$), quasi-linear viscoelastic ($Wi > 1$ and $Wi/De \ll 1$), quasi-steady viscoelastic ($De \rightarrow 0$), and finally the nonlinear viscoelastic regime ($Wi \gtrsim 1$ and $Wi/De \gtrsim 1$), which is our main emphasis. For $Wi > 1$ and $De \sim O(1)$, where the nonlinear and unsteady viscoelasticity of the material is probed, multiple overshoots are observed in the shear stress and first normal stress difference. We demonstrate that the origin of these secondary (and potentially additional) stress overshoots is analogous to a particle undergoing a Jeffery orbit under steady shear in the absence of Brownian motion. This is achieved by simultaneously analyzing the microstructure, shear stress, first normal normal stress difference, and birefringence parameters specifically for $Wi = 20$ and $De = 1$. In this case, the period of a Jeffery orbit is comparable to the period of an oscillation cycle, allowing sufficient time for a single Jeffery orbit to occur during an oscillation half-cycle. Finally, we briefly provide results for oblate spheroids of aspect ratio $r = 0.05$ and compare to the results for $r = 20$. We find that the Brownian shear stress is qualitatively similar for both prolate and oblate suspensions. However, a suspension of oblate spheroids tend to have less hydrodynamic viscoelasticity compared to a suspension of prolate particles. The work detailed in Chapter 4 is the first instance in which the (macro-scale) nonlinear oscillatory shear rheology of a micro-mechanical complex fluid model has been computed over essentially the entire range of Wi and De .

Finally, in Chapter 5 we conclude with an overall summary of our work and potential future ideas. Chapters 2–4 are self-contained works and can be read independently from the rest of the thesis. These chapters are also published in, or nearing submission to, peer-reviewed journals: Chapter 2 is published in *Rheologica Acta*²⁴; Chapter 3 is published in the *Journal of Rheology*³¹; and Chapter 4 is in preparation to be submitted to the *Journal of Rheology*.

2. Linear Viscoelasticity of a Dilute Suspension of Active Particles

2.1 Introduction

Recently, there has been an intense interest in the dynamics of active, self-propelled particles, such as biological micro-organisms and synthetic colloidal motors¹⁸⁻²³. Self-propelled particles have potential biomedical applications, including targeted drug delivery⁴²⁻⁴⁴, where a drug is transported in or on an active particle through the bloodstream directly to a predetermined location: e.g. a cancerous tumor or region of inflammation. Furthermore, suspensions of self-propelled micro-scale particles serve as a paradigmatic model for active matter, which is inherently out of thermal equilibrium due to the activity of the particles⁴⁵⁻⁴⁸. A natural question that arises is: How does the activity of the particles impact the rheology, or state of the stress, in a flowing suspension? For example, how would the addition of active particles, for use in drug delivery, impact the rheology and subsequent blood flow in a patient? Conversely, what can the stress of an active suspension tell us about the activity (e.g. mechanism or strength of self propulsion) of the particles in suspension?

In general, micro-scale self-propelled particles, at low Reynolds number, can be divided into two categories: pullers and pushers. Pullers, such as *Chlamydomonas reinhardtii* (CR), generate thrust from the front of their body; whereas, pushers, such as *Escherichia coli* (*E. coli*) or *Bacillus subtilis* (*B. subtilis*), generate thrust from their rear⁴⁹. Steady shear experiments on a dilute suspension of CR have shown that the effective viscosity of the suspension is increased, relative to both the viscosity of the suspending medium and the viscosity of a suspension of the same immotile (i.e. dead) bacteria^{50,51}. Experiments conducted on dilute suspensions of pushers, *E. coli*^{26,52} and *B. subtilis*⁵³, reported a steady shear viscosity less than that of a suspension of the same immotile bacteria and, more surprisingly, also less than the steady shear viscosity of the suspending medium. This indicates a negative particle contribution to the overall suspension viscosity.

From these experimental results, it is evident that the activity of the particles affects the stress in the suspension. The activity of the particles has an indirect effect on the stress by altering the microstructure, or spatio-temporal arrangement, of the suspension through tumbling, which acts to randomize the particle orientation, as observed in *E. coli*⁵⁴. The activity of the particles also has a direct effect on the stress via the force dipole (stresslet) generated from self-propulsion^{25,47,48}. One methodology to predict the stress of an active suspension is to calculate the disturbance flow created by the active particles. Then, from the energy dissipation associated with this, the effective viscosity can be inferred. Haines et al.⁵⁵ utilized a two-dimensional hydrodynamics simulation to calculate the disturbance flow, and hence rheology, of a dilute, active suspension of disks. Hatwalne et al.⁵⁶ utilized a coarse-grained model based on the field theory of nematic liquid crystals to predict the linear viscoelasticity of a dilute suspension of active disks or rods. Alternatively, one can explicitly determine how the activity of the particles affects the microstructure of the suspension and from there predict the microstructurally-averaged stress. In this vein, Saintillan²⁵ utilized a kinetic theory model to calculate the change in the orientational microstructure of a dilute suspension of active, slender rods, resulting from an imposed steady shear flow, rotational Brownian motion, and uncorrelated tumbling events (i.e. 90° changes in orientation due to tumbling). Bozorgi and Underhill⁵⁷ calculated the stress in a dilute suspension of slender, active rods subject to a large-amplitude oscillatory shear (LAOS) deformation. They assumed that the tumbling events did not affect the microstructure of the suspension, but did include the direct stress contribution arising from the particle activity.

In this work, we calculate the linear viscoelasticity of a dilute suspension of active, spheroidal particles, of arbitrary aspect ratio, subject to a small-amplitude oscillatory shear (SAOS) deformation. We explicitly account for microstructural relaxation due to both rotational Brownian motion and correlated tumbling, as this is relevant for many biological systems. For instance, *E. coli* are Brownian, prolate bodies with an average change in orientation due to tumbling of $58 \pm 40^\circ$ ⁵⁴. Oscillatory shear experiments are useful in that they allow for one to average the measured signal over multiple oscillation cycles and avoid step changes that occur during the start-up and cessation

of a steady flow. SAOS experiments effectively allow one to take a spectral fingerprint of the linear response of a material. The frequency-dependent results obtained from a SAOS deformation can be used to predict steady shear behavior via the empirical Cox-Merz rule, which states that the magnitude of the frequency dependent complex viscosity is equivalent to steady shear viscosity⁵⁸. Thus, information from a SAOS deformation can be utilized to predict the steady shear viscosity of a material, which is advantageous as it is typically simpler to experimentally perform a frequency-sweep as opposed to a shear-rate sweep¹⁷. This could be especially true for active suspensions of biological organisms, where large shear rates could be detrimental to the organisms and inhibit activity. Gachelin et al.⁵² observed that the effective steady shear viscosity of both a motile and immotile dilute suspension of *E. coli* were equivalent at high shear rates, indicating that the active contribution to the steady shear viscosity is negligible compared to the passive contribution in this regime. There are cases where the Cox-Merz rule breaks down, namely colloidal dispersions at high shear rate and frequency⁵⁹, and thus it should be viewed as a ‘rule-of-thumb’ rather than a strict rule.

For a homogeneous, oscillatory shear deformation, the strain-rate is given by $\dot{\gamma} = \dot{\gamma}_0 \cos(\omega t)$, where $\dot{\gamma}_0$ is the strain-rate amplitude and ω is the oscillation frequency. Two time-scales arise: 1) the oscillation time scale, $1/\omega$; and 2) the flow time scale, $1/\dot{\gamma}_0$. The active suspension is also characterized by two independent relaxation mechanisms: Brownian rotation and tumbling. Therefore, we can form two ratios of the flow to relaxation time scales, or Weissenberg numbers: $Wi_D = \dot{\gamma}_0/D_r$ and $Wi = \dot{\gamma}_0/\tau^{-1}$, where D_r is the rotary diffusion coefficient and τ^{-1} is frequency of tumbling. Furthermore, a relative rate of relaxation can be defined as $\lambda = Wi/Wi_D = D_r/\tau^{-1}$. For a dilute suspension of *E. coli*, $\lambda \sim 0.1$ (using $D_r \sim 0.1 \text{ s}^{-1}$ and $\tau^{-1} \sim 1 \text{ s}^{-1}$ ^{10,52}) and tumbling is therefore the dominant mode of microstructural relaxation. SAOS requires that the rate of relaxation is much greater than the rate of deformation, $Wi \ll 1$. Thus, the linear viscoelasticity of a dilute suspension of active spheroids is examined in this regime.

In Section 2.2 we detail the governing equations required to calculate the microstructure and linear viscoelasticity of the active suspension. In Section 2.3 a solution for the microstructure is

obtained via an asymptotic analysis for $Wi \ll 1$. In Section 2.4 the deviatoric particle contribution to the suspension stress is calculated, and the combined effects of the imposed flow, Brownian rotation, and tumbling are discussed. Finally, in Section 2.5 we demonstrate that a Cox-Merz rule can be applied to an active particle suspension by comparing our linear viscoelastic results to: 1) a theoretical prediction of the steady shear viscosity of active, slender rods²⁵ and 2) experimental data for the steady shear viscosity of a dilute suspension of *E. coli*²⁶. We also demonstrate that from the linear viscoelasticity one can determine the method of self-propulsion (pusher or puller), and estimate the strength of self-propulsion and correlation between tumbling events.

2.2 Governing Equations

A suspension of active particles is modeled as an ensemble of Brownian, rigid spheroids in a Newtonian fluid of viscosity μ_s and density ρ . The particles are assumed to be free of any externally applied force or torque and are characterized by an aspect ratio, r , defined as the ratio of the major (ℓ) to minor (a) axes, $r = \ell/a$. The hydrodynamic sphericity of the particles is given by the Bretherton constant,

$$B = \frac{r^2 - 1}{r^2 + 1}, \quad (2.1)$$

which is negative for oblate spheroids, positive for prolate spheroids, and zero for spheres. The suspension is assumed to be dilute, such that interparticle interactions can be neglected. Thus, $c = 4\pi n\ell a^2/3 \ll 1$, where c is the particle volume fraction and n is the number density. We will consider an oscillatory shear flow with velocity field $\mathbf{v} = \dot{\gamma}_0 y \cos(\alpha \tilde{t}) \mathbf{e}_x$, and velocity gradient $\nabla \mathbf{v} = \dot{\gamma}_0 \cos(\alpha \tilde{t}) \mathbf{e}_y \mathbf{e}_x$, where \mathbf{e}_x , \mathbf{e}_y , \mathbf{e}_z are Cartesian unit vectors in the flow, flow-gradient, and vorticity directions, respectively, α is the dimensionless oscillation frequency, and \tilde{t} is dimensionless time ($\alpha = \omega\tau$, $\tilde{t} = t/\tau$).

The microstructure of the suspension is characterized by the orientation distribution function, $\psi(\mathbf{p}, t)$, where $\psi(\mathbf{p}, t) \sin\theta d\theta d\phi$ represents the probability of finding a particle ensemble in a differential region about (θ, ϕ) ^{11,12}. Here, \mathbf{p} is a unit vector along the particle axis of symmetry, in spherical coordinates, and θ and ϕ are the polar and azimuthal angles, respectively. The orientation

distribution function satisfies a conservation, or Fokker-Planck, equation⁶⁰,

$$\frac{\partial \psi}{\partial t} + \nabla_{\mathbf{p}} \cdot (\dot{\mathbf{p}} \psi) = D_r \nabla_{\mathbf{p}}^2 \psi - \tau^{-1} \left(\psi - \int K(\mathbf{p}|\mathbf{p}') \psi(\mathbf{p}', \tilde{t}) dS' \right), \quad (2.2)$$

where $\nabla_{\mathbf{p}}$ is the surface gradient operator, and $\dot{\mathbf{p}}$ is the deterministic evolution of the particle orientation due to the ambient shear^{9,12,13},

$$\dot{\mathbf{p}} = B(\mathbf{I} - \mathbf{p}\mathbf{p}) \cdot \mathbf{H} \cdot \mathbf{p}, \quad (2.3)$$

where \mathbf{I} is the identity tensor and $\mathbf{H} = B^{-1}\boldsymbol{\Omega} + \mathbf{E}$. Here, $\boldsymbol{\Omega}$ is the vorticity tensor and \mathbf{E} is the rate of strain tensor, such that $\nabla \mathbf{v} = \mathbf{E} + \boldsymbol{\Omega}$. For an oscillatory shear deformation, $\mathbf{H} = \dot{\gamma}_0 \cos(\alpha \tilde{t}) \check{\mathbf{H}}$, where,

$$\check{\mathbf{H}} = \frac{1}{2} \left[(1 - B^{-1}) \mathbf{e}_x \mathbf{e}_y + (1 + B^{-1}) \mathbf{e}_y \mathbf{e}_x \right]. \quad (2.4)$$

The first term on the right-hand-side (RHS) of (2.2) accounts for the randomization of particle orientation due to rotational Brownian diffusion. The last terms on the RHS, in parentheses, of (2.2) model the randomization of particle orientation due to tumbling events. Specifically, tumbling events are treated as a Poisson process⁶⁰. Here, $K(\mathbf{p}|\mathbf{p}')$ is a conditional probability density function characterizing a tumble from orientation \mathbf{p}' to orientation \mathbf{p} , where the apostrophe indicates the pre-tumble orientation, and $dS' = \sin \theta' d\theta' d\phi'$ is the pre-tumble differential solid angle. Conservation of probability requires that,

$$\int K(\mathbf{p}|\mathbf{p}') dS = \int K(\mathbf{p}|\mathbf{p}') dS' = 1. \quad (2.5)$$

Following Subramanian and Koch⁶⁰, we choose

$$K(\mathbf{p}|\mathbf{p}') = \frac{\beta}{4\pi \sinh \beta} \exp(\beta \mathbf{p} \cdot \mathbf{p}'), \quad (2.6)$$

where β is parameter that gauges the correlation between pre- and post-tumble configurations. In the limit of $\beta \rightarrow 0$, $K = 1/4\pi$, corresponding to uncorrelated tumbles (90° changes in orientation), and the term in parentheses on the RHS of (2.2) reduces to the relaxation-time approximation used in the kinetic theory of gases^{61,62}. This limit was previously investigated by Saintillan²⁵ for slender, active rods in steady shear. In the limit of $\beta \rightarrow \infty$, each tumbling event results in an infinitesimal change in orientation, and thus microstructural relaxation is dominated by rotational diffusion. This regime was investigated by Bozorgi and Underhill⁵⁷. The inclusion of finite, non-zero values of β allows one to account for correlated tumbles. For instance, the average change in orientation due to tumbling ($\langle \theta \rangle$) for an *E. coli* cell is $58 \pm 40^\circ$ ⁵⁴, which corresponds to $\beta \sim 1.5$, where⁶⁰,

$$\langle \theta \rangle = \frac{\beta}{2 \sinh \beta} \int_0^\pi e^{\beta \cos \theta} \theta \sin \theta d\theta. \quad (2.7)$$

A dimensionless conservation equation can be obtained by normalizing \mathbf{H} by the strain-rate amplitude ($\mathbf{H} = \dot{\gamma}_0 \tilde{\mathbf{H}}$). Substitution of (2.3) into (2.2) yields,

$$\frac{\partial \psi}{\partial \tilde{t}} + BWi \nabla_{\mathbf{p}} \cdot \left[(\mathbf{I} - \mathbf{p}\mathbf{p}) \cdot \tilde{\mathbf{H}} \cdot \mathbf{p} \psi \right] = \lambda \nabla_{\mathbf{p}}^2 \psi - \left(\psi - \int K(\mathbf{p}|\mathbf{p}') \psi(\mathbf{p}', \tilde{t}) dS' \right), \quad (2.8)$$

The orientation distribution function is also subject to a normalization condition, $\int \psi(\mathbf{p}, t) dS = 1$.

2.3 Asymptotic Expansion for Linear Viscoelasticity

The conservation equation (2.8) is to be addressed in the limit of weak deformation rate, $Wi \ll 1$. In this regime, the microstructure remains in a near-equilibrium state, and the orientation distribution function can be expressed as a regular perturbation expansion,

$$\psi(\mathbf{p}, t) = \frac{1}{4\pi} \left(1 + Wi \psi_1(\mathbf{p}, t) + O(Wi^2) \right), \quad (2.9)$$

where $W_i\psi_1$ represents the leading order departure from equilibrium. Substitution of (2.9) into (2.8) yields,

$$\frac{\partial\psi_1}{\partial\tilde{t}} = 3B \cos(\alpha\tilde{t}) \mathbf{pp} : \check{\mathbf{E}} + \lambda \left[(\mathbf{I} - \mathbf{pp}) : \frac{\partial^2\psi_1}{\partial\mathbf{p}\partial\mathbf{p}} - 2\mathbf{p} \cdot \frac{\partial\psi_1}{\partial\mathbf{p}} \right] - \left(\psi_1 - \int K\psi_1(\mathbf{p}', \tilde{t}) dS' \right), \quad (2.10)$$

subject to $\int \psi_1 dS = 0$. Here, $\mathbf{E} = \dot{\gamma}_0 \cos(\alpha\tilde{t}) \check{\mathbf{E}}$ and $\check{\mathbf{E}} = \frac{1}{2} (\mathbf{e}_x \mathbf{e}_y + \mathbf{e}_y \mathbf{e}_x)$. The solution to (2.10) should oscillate at the input frequency, α , and linearly depend on the imposed flow through the quadrupolar forcing $3B \cos(\alpha\tilde{t}) \mathbf{pp} : \check{\mathbf{E}}$, which acts to align the microstructure along the principle axes of strain. Hence, we pose,

$$\psi_1(\mathbf{p}, \tilde{t}) = \left(h_1 e^{i\alpha\tilde{t}} + \hat{h}_1 e^{-i\alpha\tilde{t}} \right) \mathbf{pp} : \check{\mathbf{E}}, \quad (2.11)$$

where hatted quantities indicate complex conjugates. Substitution of (2.11) into (2.10) yields an algebraic equation for h_1 , with solution,

$$h_1 = \frac{3B}{2} \left[\frac{1 - J(\beta) + 6\lambda - i\alpha}{\alpha^2 + (1 - J(\beta) + 6\lambda)^2} \right], \quad (2.12)$$

where $i = \sqrt{-1}$ and

$$J(\beta) = \frac{(3 + \beta^2) \sinh \beta - 3\beta \cosh \beta}{\beta^2 \sinh \beta}. \quad (2.13)$$

To determine (2.12) and (2.13), we have used the result: $\int K\mathbf{p}'\mathbf{p}' : \check{\mathbf{E}} dS' = J(\beta)\mathbf{pp} : \check{\mathbf{E}}$. A derivation of this relation can be found in Appendix B of Subramanian and Koch⁶⁰; in their equation (B8), the coefficient of $\sinh \beta$ is incorrect and should read $-(3\beta^2 + 6)$. The expression in (2.13) is even and is bounded by $J(\beta) = [0, 1)$, corresponding to $\beta = [0, \pm\infty)$. Next, we utilize our asymptotic solution to the orientation distribution function to calculate the linear viscoelasticity of the suspension.

2.4 Linear Viscoelasticity

The particle contribution to the deviatoric stress of the suspension ($\boldsymbol{\tau}^P$) is obtained from an ensemble average of the stresslet, which can be decomposed into three contributions arising from: the imposed flow ($\boldsymbol{\tau}^F$), rotational Brownian motion ($\boldsymbol{\tau}^B$), and the active nature (self-propulsion) of the particles ($\boldsymbol{\tau}^A$),

$$\boldsymbol{\tau}^P = \boldsymbol{\tau}^F + \boldsymbol{\tau}^B + \boldsymbol{\tau}^A. \quad (2.14)$$

The contribution from the imposed flow is given by^{11,12},

$$\frac{\boldsymbol{\tau}^F}{2\mu_s c} = 2A_H \langle \mathbf{pppp} \rangle : \mathbf{E} + 2B_H \left(\mathbf{E} \cdot \langle \mathbf{pp} \rangle + \langle \mathbf{pp} \rangle \cdot \mathbf{E} + \frac{2\mathbf{I}}{3} \mathbf{E} : \langle \mathbf{pp} \rangle \right) + C_H \mathbf{E} \quad (2.15)$$

where the angled brackets are orientational averages,

$$\langle \mathbf{pp} \rangle = \int \mathbf{pp} \psi(\mathbf{p}, \tilde{t}) dS, \quad (2.16)$$

and similarly for $\langle \mathbf{pppp} \rangle$. The torque generated from rotational Brownian motion leads to the following stress contribution^{11,12},

$$\boldsymbol{\tau}^B = 2\mu_s c F_H D_r \left(\langle \mathbf{pp} \rangle - \frac{\mathbf{I}}{3} \right). \quad (2.17)$$

Here, A_H , B_H , C_H , and F_H are known scalar functions of the particle aspect ratio, r ,^{11,12}. Finally, the self-propulsion of the particles exerts a force-dipole onto the fluid, resulting in the active stress contribution⁶³,

$$\boldsymbol{\tau}^A = n\sigma_0 \left(\langle \mathbf{pp} \rangle - \frac{\mathbf{I}}{3} \right), \quad (2.18)$$

where σ_0 is a scalar dipole strength, in units of energy. The sign of σ_0 indicates the mechanism of self-propulsion (i.e. $\sigma_0 < 0$ for pushers and $\sigma_0 > 0$ for pullers) and the magnitude of σ_0 scales with the swimming speed of the particle⁶³.

Substitution of (2.11) and (2.12) into (2.15), (2.17), and (2.18) yields for the shear component of the stress, τ_{yx} ,

$$\frac{\tau_{yx}^F}{\dot{\gamma}_0 \mu_s c} = \left(\frac{4A_H}{15} + \frac{2B_H}{3} + C_H \right) \cos(\alpha \tilde{t}) + O(Wi), \quad (2.19)$$

$$\begin{aligned} \frac{\tau_{yx}^B}{\dot{\gamma}_0 \mu_s c} = \frac{2F_H B \lambda}{5} & \left[\frac{1 - J(\beta) + 6\lambda}{\alpha^2 + (1 - J(\beta) + 6\lambda)^2} \cos(\alpha \tilde{t}) \right. \\ & \left. + \frac{\alpha}{\alpha^2 + (1 - J(\beta) + 6\lambda)^2} \sin(\alpha \tilde{t}) \right] + O(Wi), \end{aligned} \quad (2.20)$$

and

$$\begin{aligned} \frac{\tau_{yx}^A}{\dot{\gamma}_0 \mu_s c} = \frac{zB}{5} & \left[\frac{1 - J(\beta) + 6\lambda}{\alpha^2 + (1 - J(\beta) + 6\lambda)^2} \cos(\alpha \tilde{t}) \right. \\ & \left. + \frac{\alpha}{\alpha^2 + (1 - J(\beta) + 6\lambda)^2} \sin(\alpha \tilde{t}) \right] + O(Wi). \end{aligned} \quad (2.21)$$

Note that the shear component of the stress is all that is obtained from linear viscoelasticity; normal stress differences can be obtained at $O(Wi^2)$, requiring knowledge of ψ_2 . Here, $z = \sigma_0 \tau / \mu_s V_p$ is a dimensionless dipole moment and V_p is the volume of a single particle. For $\lambda < 1$ ($\lambda > 1$), the frequency of tumbling is greater (less) than the frequency of rotational Brownian motion; the dominant relaxation mechanism is tumbling (rotational Brownian motion). The overall particle contribution to the deviatoric stress can be expressed as the sum of a viscous and elastic response,

$$\frac{\tau_{yx}^P}{\dot{\gamma}_0} = \eta'(\alpha) \cos(\alpha \tilde{t}) + \eta''(\alpha) \sin(\alpha \tilde{t}) + O(Wi), \quad (2.22)$$

where η' and η'' are the viscous and elastic components of the complex viscosity ($\eta^* = \eta' + i\eta''$),

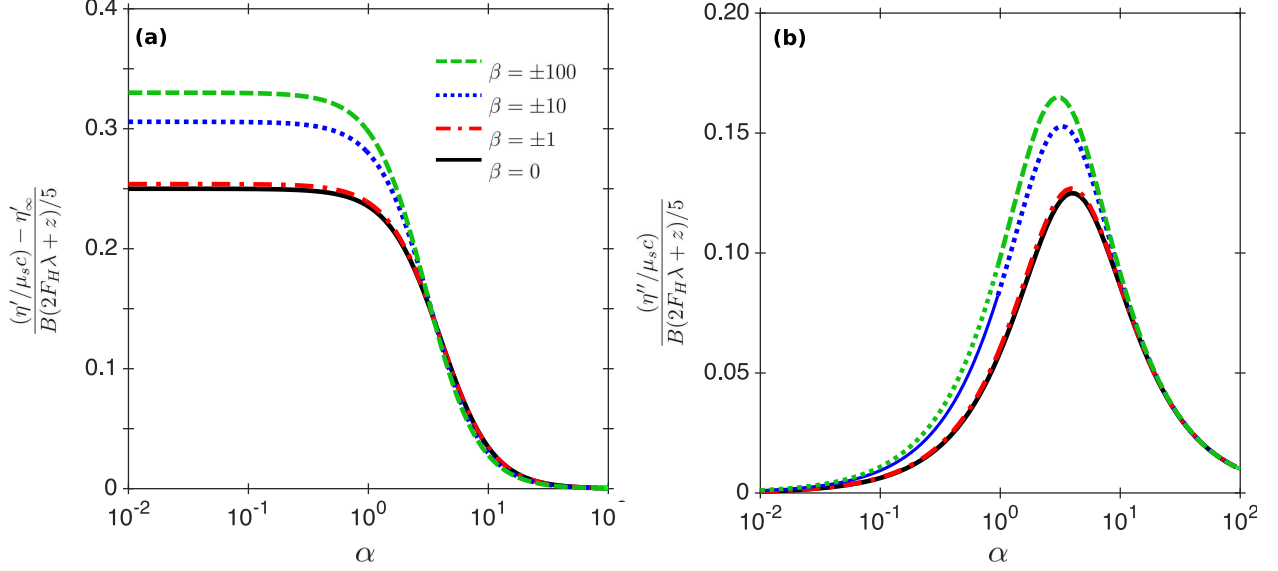


Figure 2.1: Effect of correlated tumbling ($\beta \neq 0$) on: **(a)** the viscous and **(b)** elastic components of the complex viscosity for $\lambda = 0.5$. Here, $\eta'_{\infty} = 4A_H/15 + 2B_H/3 + C_H$ is the viscous complex viscosity in the limit of $\alpha \rightarrow \infty$. Correlated tumbling events increase the magnitude of the Brownian and active stress contribution at small to moderate frequency values ($\alpha \lesssim 10$), resulting in an increased magnitude of the viscous and elastic components.

respectively, which are given by,

$$\frac{\eta'}{\mu_{sc}} = \frac{4A_H}{15} + \frac{2B_H}{3} + C_H + \frac{B}{5} (2F_H\lambda + z) \frac{1 - J(\beta) + 6\lambda}{\alpha^2 + (1 - J(\beta) + 6\lambda)^2}, \quad (2.23)$$

and

$$\frac{\eta''}{\mu_{sc}} = \frac{B}{5} (2F_H\lambda + z) \frac{\alpha}{\alpha^2 + (1 - J(\beta) + 6\lambda)^2}. \quad (2.24)$$

Figure 2.1 shows the effect of correlated tumbling ($\beta \neq 0$) on the magnitude of the viscous and elastic components of the complex viscosity. Correlated tumbling events increase the magnitude of the Brownian and active stress response, compared to uncorrelated tumbling events, at small and moderate frequency values ($\alpha \leq O(10)$).

Since z can be positive or negative, depending on the mechanism of self-propulsion, we can define a critical dipole strength, z^* , at which the particle contribution to the zero-frequency viscous

complex viscosity is zero ($\eta'(0) = 0$),

$$z^* = \frac{5}{B(1 - J(\beta) + 6\lambda)} \left(\frac{4A_H}{15} + \frac{2B_H}{3} + C_H \right) + 2F_H\lambda, \quad (2.25)$$

which is positive for prolate spheroids and negative for oblate spheroids, the latter since $B, F_H < 0$ for $r < 1$. Thus, a dispersion of prolate pushers with dipole strength $z < -z^*$ can have a negative contribution to the overall viscosity of the suspension, as previously predicted^{25,55,56} and observed^{26,52,53}. However, we are not aware of prior experimental work indicating a negative contribution to the overall viscosity for oblate pullers, as is predicted here.

Figure 2.2 shows a schematic representation of the stresslet (force dipole exerted by the particle onto the fluid) for a prolate spheroid subject to a shear flow. The passive contribution to the stresslet, resulting from the imposed flow and Brownian rotation, always results in a compressional stresslet and therefore a positive contribution to the suspension viscosity. However, the active contribution, arising from the thrust force and compensating drag force generated from self-propulsion, can result in either a compressional or extensional stresslet, depending on the mechanism of self-propulsion. Prolate pullers, which generate thrust from the front, always have a compressional active stresslet, and therefore a compressional overall stresslet (Figure 2.2a) and positive contribution to the suspension viscosity. Weak prolate pushers, which generate thrust from behind and are characterized by the dipole strength $-z^* < z < 0$, will have an extensional active stresslet, but a compressional overall stresslet (Figure 2.2b). This results in a positive contribution to the suspension viscosity, but the magnitude of the viscosity increase is less than that of a passive suspension. Strong prolate pushers, characterized by $z < -z^* < 0$, will have an extensional active stresslet of greater magnitude than the passive stresslet contribution, resulting in an extensional overall stresslet (Figure 2.2c) and a negative contribution to the suspension viscosity. Note that the overall viscosity of the suspension (η), which includes the contribution of the suspending medium (μ_s), will remain positive for a dilute suspension of prolate pullers or pushers, regardless of the magnitude of the dipole, as $\eta = \mu_s + c\eta^p$, where η^p is the particle contribution to the overall

viscosity and $c (\ll 1)$ is the particle volume fraction

The linear relaxation modulus, $G_I(s)$, is defined as¹⁷,

$$G_I(s) = \frac{2}{\pi} \int_0^\infty \eta'(\alpha) \cos(\alpha s) ds, \quad (2.26)$$

and can be determined from (2.23) to be,

$$G_I(\tilde{t}) = \left(\frac{8A_H}{15} + \frac{4B_H}{3} + 2C_H \right) \delta(\tilde{t}) + \frac{B}{5} \left(2F_H \lambda + z \right) e^{-(1-J(\beta)+6\lambda)\tilde{t}}. \quad (2.27)$$

The linear relaxation modulus has the functional form of the Jeffrey's model: an instantaneous response combined with stress relaxation via an exponentially fading memory, similar to that of passive spheroids^{31,64,65}. In contrast to a suspension of passive spheroids, the rate of stress relaxation, $1/t_r$, which is defined from the argument of the exponential in (3.55), is

$$\frac{1}{t_r} = \frac{1}{t_T} + \frac{1}{t_B}, \quad (2.28)$$

where $t_T = \tau/[1 - J(\beta)]$ is the time-scale of tumbling events and $t_B = 1/6D_r$ is the time-scale of rotational Brownian motion. This combination of two stress relaxation mechanisms is analogous to a pair of resistors in parallel in an electrical circuit, where the overall resistance of the system (R_{total}) is the reciprocal of the sum of the reciprocal resistance of each resistor (R_i), $1/R_{total} = \sum_i 1/R_i$. Here, the overall rate of stress relaxation is the sum of the reciprocal of the time-scale of each relaxation mechanism. The combination of stress relaxation from tumbling events and rotational Brownian motion increases the overall rate of stress relaxation, relative to a suspension of non-Brownian, active particles or a suspension of Brownian, inactive particles.

Figures 2.3 and 2.4 depict the complex viscosity of a dilute suspension of prolate ($r = 3$) and oblate ($r = 0.25$) spheroids, respectively, as a function of self-propulsion mechanism, z , and relative importance of tumbling to rotational Brownian motion, λ . For both prolate and oblate spheroids, the plateau frequency, which is defined as the frequency at which the material response

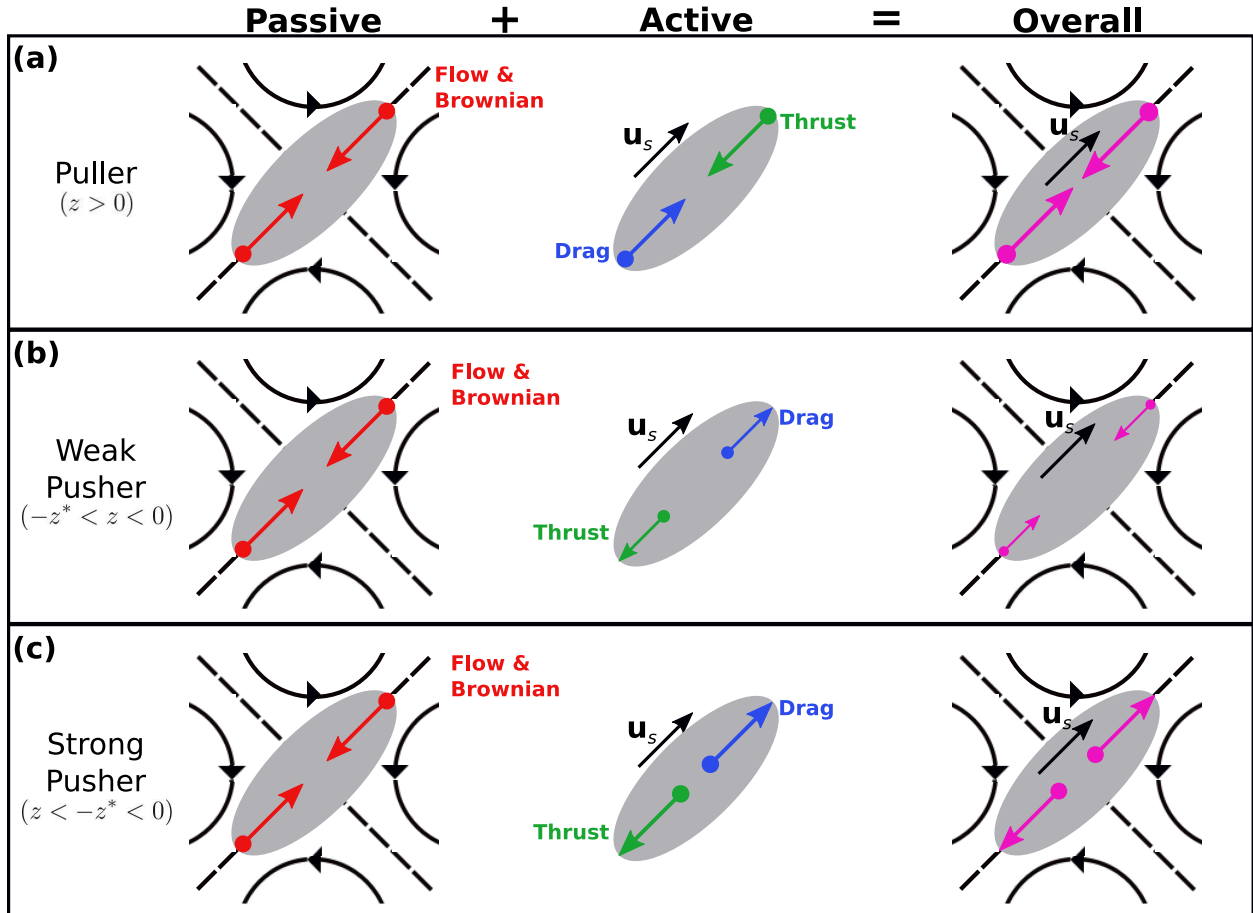


Figure 2.2: Schematic of the stresslet for a prolate spheroid in steady shear flow for different self-propulsion mechanisms: **(a):** Puller ($0 < z$), **(b):** Weak Pusher ($-z^* < z < 0$), and **(c):** Strong Pusher ($z < -z^* < 0$). The solid black lines represent the straining component of the flow and the dashed black lines the principle axes of strain. In the limit of $Wi \ll 1$, the flow, to leading order, acts to align the microstructure along the principle axes of strain. The passive contribution (left, red) to the stresslet, from the imposed flow and rotational Brownian motion, always results in a compressional force-dipole from the particle onto the fluid. However, the active contribution (middle, green and blue) to the stresslet can be either compressional or extensional, depending on the mechanism of self-propulsion. Thus, for pullers and weak pushers, the overall stresslet (right, magenta) is compressional. Whereas, for strong pushers, the overall stresslet is extensional, resulting in a negative viscosity contribution. Here, u_s indicates the self-propelled swimming speed of particle.

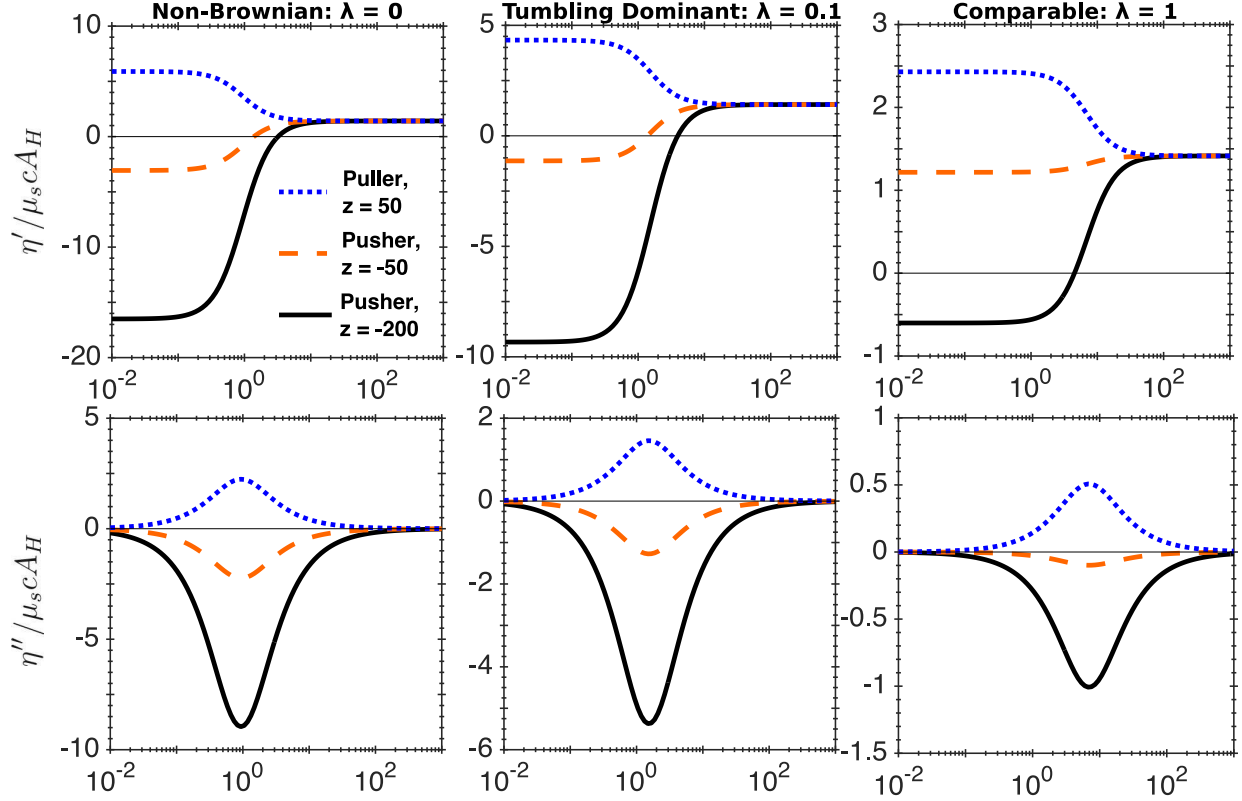


Figure 2.3: Viscous (η' , top) and elastic (η'' , bottom) components of the complex viscosity for a dilute suspension of active prolate spheroids ($r = 3$) for 1) a puller: $z = 50$, 2) a weak pusher: $z = -50$, and 3) a strong pusher: $z = -200$. Here, the ratio of tumbling frequency to rotational Brownian motion is varied: (a): $\lambda = 0$, (b): $\lambda = 0.1$, and (c): $\lambda = 1$ and $z^* = -150.4$, using $\lambda = 1$ and $\beta = 1$.

no longer changes, increases as the strength of rotational Brownian motion increases (i.e. as λ increases). Furthermore, we also observe that prolate pullers and oblate pushers will always have a positive viscous and elastic response, independent of frequency. Whereas, prolate pushers and oblate pullers with a dipole strength greater than the critical dipole strength, defined in (2.25), can have a negative viscous and elastic response at low frequency.

2.5 Comparison to Previous Work

2.5.1 Steady shear of active, slender rods ($r \rightarrow \infty$)

The particle contribution to the steady shear viscosity of a dilute suspension of active, slender rods ($r \rightarrow \infty$) was previously calculated by Saintillan²⁵ for uncorrelated tumbling events ($\beta = 0$). We

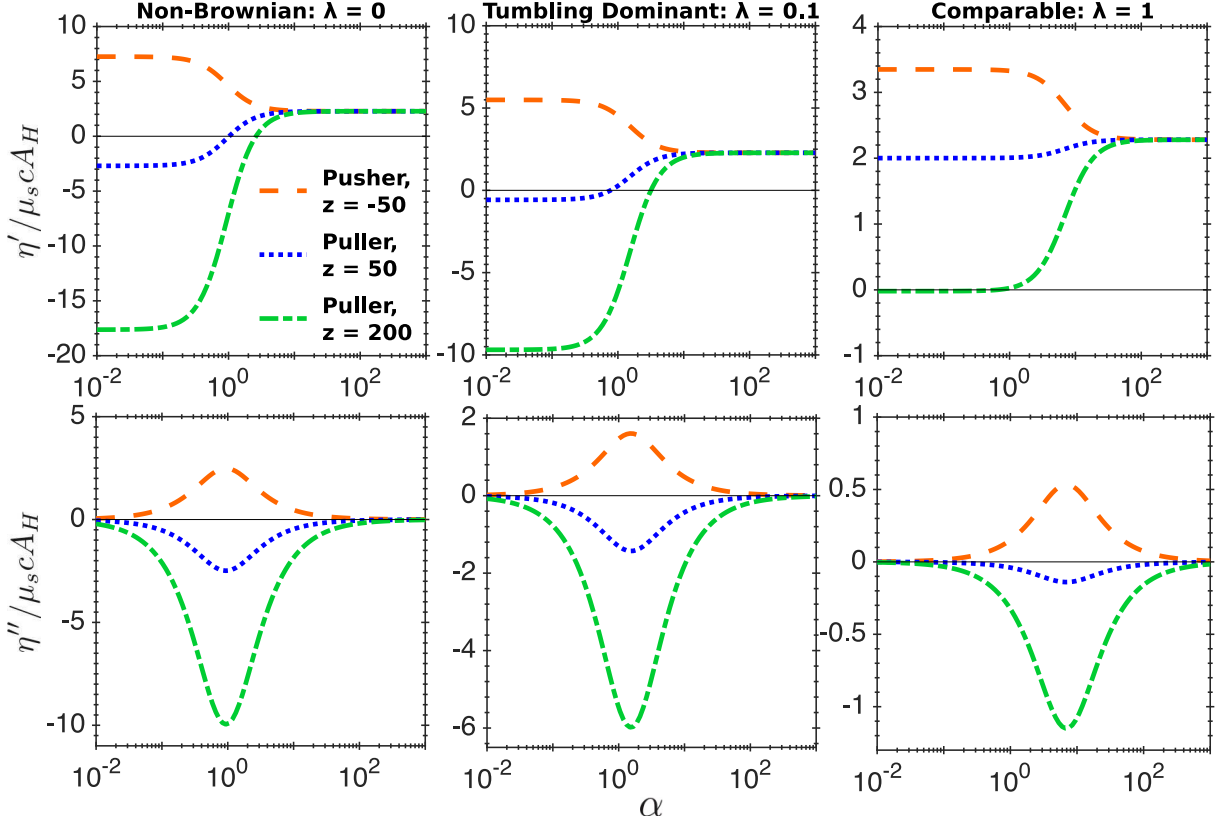


Figure 2.4: Viscous (η' , top) and elastic (η'' , bottom) components of the complex viscosity for a dilute suspension of active oblate spheroids ($r = 0.25$) for 1) a pusher: $z = -50$, 2) a weak puller: $z = 50$, and 3) a strong puller: $z = 200$. Here, the ratio of tumbling frequency to rotational Brownian motion is varied: (a): $\lambda = 0$, (b): $\lambda = 0.1$, and (c): $\lambda = 1$ and $z^* = 198.5$, using $\lambda = 1$ and $\beta = 1$.

can compare these steady shear results to our linear viscoelastic response, via the Cox-Merz rule,

$$\eta(Wi) = |\eta^*(\alpha)|, \quad (2.29)$$

which states that, for $Wi = \alpha$, the steady shear viscosity is equal to the magnitude of the frequency-dependent complex viscosity. Figure 2.5 shows a comparison of the linear viscoelasticity and the steady shear viscosity for a puller and a pusher at $\lambda = 0.5$. In Figure 2.5a, we observe that the Cox-Merz rule holds fairly well for prolate pullers, with a qualitative agreement overall all frequencies. For prolate pushers, which have a negative contribution to the overall viscosity of the suspension, the Cox-Merz rule does not hold, as the magnitude of the complex viscosity is always a positive quantity (Figure 2.5b). However, we observe agreement between the steady shear viscosity and the

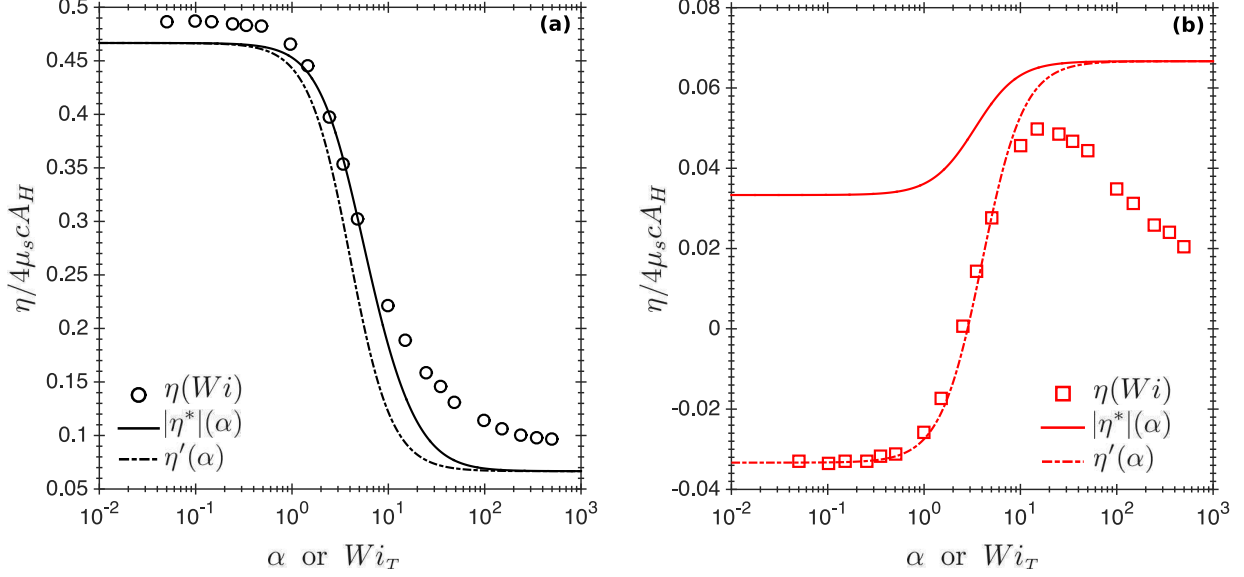


Figure 2.5: Cox-Merz rule for active suspensions. Here, we compare our theoretical prediction to that of²⁵ (see his Figure 5a) for $r \rightarrow \infty$, $\beta = 0$, $\lambda = 0.5$ (corresponding to $\tilde{\tau} = 5$ and $\tilde{d}_r = 0.1$ in the notation of²⁵) for (a): puller ($z = 4A_H$) and (b): pusher ($z = -4A_H$). The symbols (\circ , \square) are the digitized numerical results for the steady shear viscosity from Saintillan 2010. The solid line is the magnitude of the complex viscosity, from (2.23)-(2.24), and the dot-dashed line is the viscous component of the complex viscosity, from (2.23).

viscous component of the complex viscosity up to $O(10)$ in the shear rate (Wi) or frequency (α). This indicates that the particle contribution to the steady shear viscosity is akin to the linear viscous response for an active suspension, up to moderate shear rate. That is, $\eta(\dot{\gamma}_0) = \eta'(\omega)$ is applicable beyond the zero-shear and zero-frequency limit and can be viewed as a modified Cox-Merz rule for active suspensions with a negative viscosity increment. The deviation between the steady shear and both the viscous complex viscosity and magnitude of the complex viscosity, at larger Wi and frequency, is consistent with passive colloidal systems⁵⁹.

2.5.2 Experimental results for suspensions of *E. coli*

Now that we have demonstrated that a modified Cox-Merz rule is applicable to a dilute, active suspension, at least to moderate frequency and shear rate, we can extend our comparison to an experimental system. In Figure 2.6 we show the digitized steady shear viscosity measurements of López et al.²⁶ for *E. coli* suspensions (symbols), which includes the contribution of the suspending medium, compared to the viscous component of the complex viscosity (2.23), at varied volume

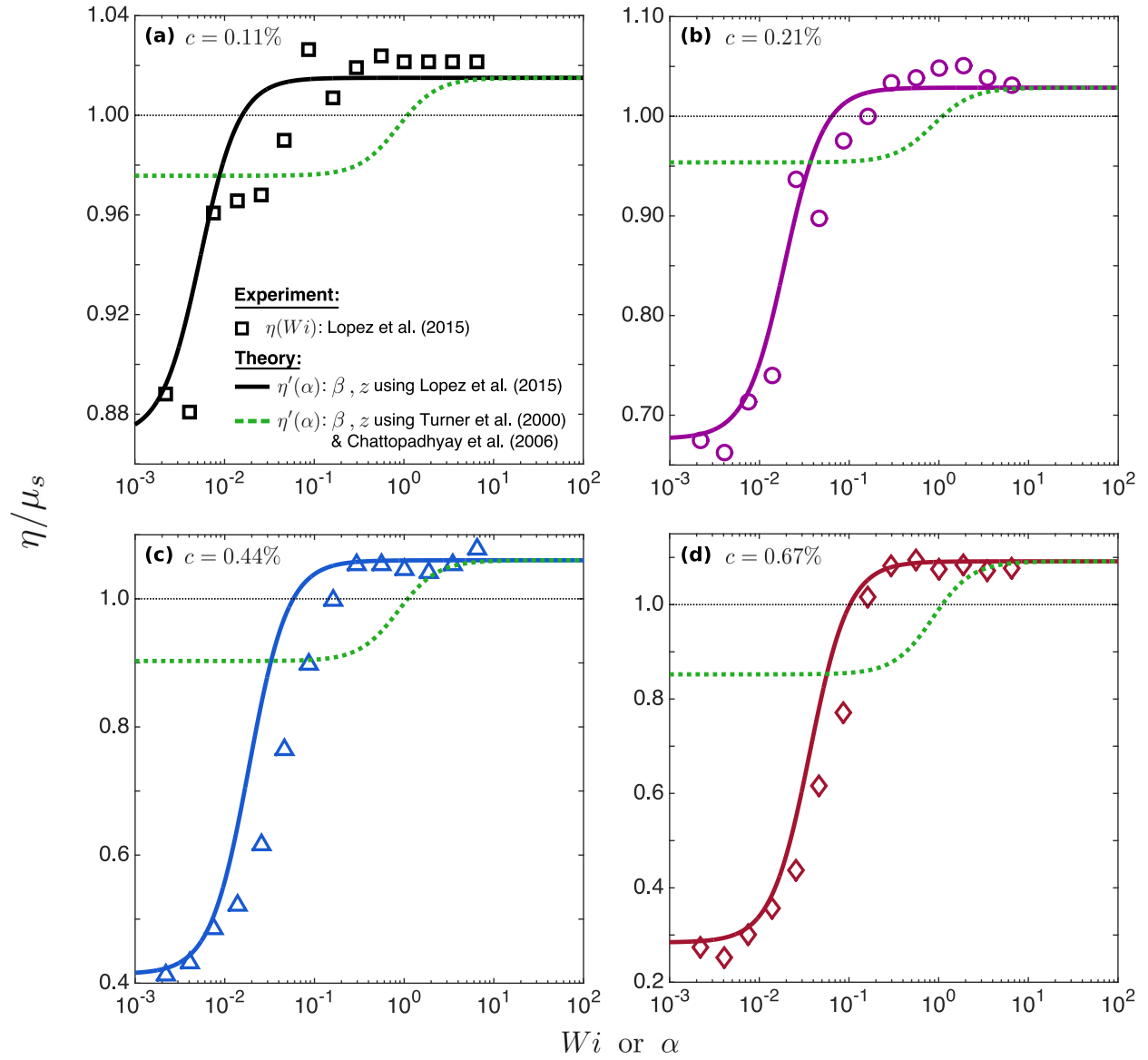


Figure 2.6: Comparison of the linear viscoelasticity of a suspension of pushers to experimental measurements of the steady shear viscosity of *E. coli*, which include the contribution of the suspending medium, for cell volume fractions, c , of (a): 0.11%, (b): 0.21%, (c): 0.44%, and (d): 0.67%. The symbols are experimental data from López et al.²⁶ (see their Figure 1b) for $\mu_s = 1.4$ mPa, and $T = 298$. The solid line is the viscous complex viscosity in (2.23) using $r = 20$, $\tau = 0.1$ s, $\lambda = 9 \times 10^{-4}$, and the appropriate β and z values from Table 2.1. The volume fraction-dependent values of β and z were obtained from the steady shear viscosity measurements at $Wi = 0.002$ and $Wi = 0.007$. The dotted line is the viscous complex viscosity from (2.23), now using $\beta = 1.64$, which was obtained from fluorescence microscopy⁵⁴, and $z = -155.5$, which was obtained from optical trapping measurements⁶⁶.

fractions (solid lines). The experimental parameters reported by López et al.²⁶ utilized in (2.23) are: $\tau^{-1} = 10$ Hz, $T = 298$ K, and $\mu_s = 1.4$ mPa. To determine the relative frequency of Brownian rotation to tumbling (λ), we first calculated the rotational diffusion coefficient for a single particle¹⁰,

$$D_r = \frac{k_B T}{4\mu_s V_p} \left(\frac{r^2 K_3(r) + K_1(r)}{r^2 + 1} \right), \quad (2.30)$$

where,

$$K_1(r) \equiv \int_0^\infty \frac{r \, ds}{(r^2 + s)^{1/2} (1 + s)^2}, \quad (2.31)$$

$$K_3(r) \equiv \int_0^\infty \frac{r \, ds}{(r^2 + s)^{3/2} (1 + s)}, \quad (2.32)$$

and k_B is the Boltzmann constant. Substitution of the given values for temperature and suspending medium viscosity, along with an estimate of aspect ratio of an *E. coli* cell, $r = 20$ ($\ell \sim 5 \mu\text{m}$ and $a \sim 0.25 \mu\text{m}$ ^{26,52,67}), into (2.30) yields $D_r = 0.009 \text{ s}^{-1}$. Thus, $\lambda = D_r/\tau^{-1} = 9 \times 10^{-4}$ and tumbling is the dominant mode of microstructural relaxation. Here, the estimate of the aspect ratio of an *E. coli* cell includes the length of the flagella tail that is responsible for self-propulsion and tumbling. Next, we utilized the steady shear viscosity measurements at $Wi = 0.002$ and $Wi = 0.007$ and the modified Cox-Merz rule via (2.23) to obtain a system of two equations and two unknowns (β and z); solving this system of equations simultaneously obtains β and z , which are listed for each volume fraction in Table 2.1. The dotted line in Figure 2.6 is the viscous complex viscosity given in (2.23) for $\beta = 1.64$, corresponding to $\langle \theta \rangle = 58^\circ$ ⁵⁴, and $z = -155.5$, corresponding to a thrust force, $F_{\text{thrust}} = \sigma_0/\ell = 0.57 \text{ pN}$ ⁶⁶.

From Figure 2.6 we see a qualitative agreement between the steady shear viscosity measurements of López et al.²⁶ and our prediction of the linear viscoelasticity, using the values of β and z in Table 2.1 at all values of Wi and α . However, the use of β obtained from fluorescence mi-

Table 2.1: Volume fraction-dependent self-propulsion parameters of *E. coli*. The values of β and z were obtained by applying the modified Cox-Merz rule discussed in Section 5.1 and equating the steady shear viscosity measurements of López et al.²⁶ at $Wi = 0.002$ and 0.007 to the viscous component of the complex viscosity, given in (2.23), for $r = 20$, $\tau^{-1} = 10$ Hz, $\lambda = 9 \times 10^{-4}$, $\mu_s = 1.4$ mPa, and $T = 298$ K.

c	β	$\langle \theta \rangle$	z	F_{thrust} (pN)
0.11%	∞	0°	-4.2	0.015
0.21%	223	4.8°	-16.9	0.062
0.44%	233	4.7°	-14.5	0.053
0.67%	96	7.3°	-22.9	0.084

croscopy⁵⁴ and z from optical trapping of a single cell⁶⁶ does not provide a reasonable agreement to the experimental data. This suggests that the measured self-propulsion characteristics of an active suspension are sensitive to the volume fraction of particles. Furthermore, the cell volume fractions utilized by²⁶ are arguably beyond the dilute regime, where hydrodynamic interactions between cells is negligible; collective motion has been observed in suspensions of *E. coli* for $n = O(10^8)$ cells/mL⁶⁸, which corresponds to $c \sim 0.01\%$. Despite the fact that the data reported by López et al.²⁶ is at volume fractions above this threshold, we surprisingly observe good agreement between their experimental results and our dilute theory. Thus, the results from the SAOS of a dilute, active suspension are able to provide the self-propulsion characteristics of active particles; namely, the self-propulsion mechanism (pusher or puller), dipole strength ($|\sigma_0|$), and correlation between tumbling events (β).

2.6 Summary

We calculated the linear viscoelasticity of a dilute suspension of active spheroids of arbitrary aspect ratio subject to a SAOS deformation. The active suspension is characterized by two relaxation mechanisms: rotational Brownian motion and correlated tumbling. For weak deformation ($Wi \ll 1$), the particle contribution to the stress was determined from ensemble averages of the stresslets due to the imposed flow, rotational Brownian motion, and tumbling. From a comparison to the steady shear result of Saintillan²⁵ for slender rods, we show that a modified Cox-Merz rule is applicable to a dilute active suspension. Furthermore, through a comparison with the ex-

perimental results of López et al.²⁶ for *E. coli*, we demonstrated that from the SAOS of an active suspension, one can determine the mechanism of self-propulsion (pusher or puller) and estimate the strength of the dipole moment ($|\sigma_0|$) and correlation between tumbling events (β) of the particles. A natural extension to the present work would be to quantify how correlated tumbling affects the nonlinear rheology of an active suspension: e.g. shear-thinning (or thickening) and normal stress coefficients.

3. Nonlinear Relaxation Modulus via Dual-Frequency Medium Amplitude Oscillatory Shear

3.1 Introduction

The viscoelasticity of complex fluids is most commonly measured using oscillatory shear rheometry, where a fluid is subjected to a sinusoidal, simple shear deformation¹⁷. Oscillatory testing is experimentally useful as it allows one to average signals over multiple periods and avoid step changes such as in the start-up or cessation of a flow. The strain is typically given by $\gamma = \gamma_0 \sin(\omega t)$, where γ_0 is the strain amplitude, ω is the oscillation frequency, and t is time. For this deformation, two time-scales arise: 1) the flow time scale, $1/\dot{\gamma}_0$, where $\dot{\gamma}_0 = \gamma_0\omega$ is the strain-rate amplitude; and 2) the oscillation time scale, $2\pi/\omega$. Assuming that the material is characterized by a single relaxation time, λ , two dimensionless numbers can be obtained, which characterize the state of the stress in the material. The first is the ratio between the relaxation and oscillation time scales, or the Deborah number $De = \lambda\omega$. The second is the ratio of the relaxation to the flow time scales, or the Weissenberg number $Wi = \lambda\dot{\gamma}_0$. Small amplitude oscillatory shear (SAOS) requires $Wi \ll 1$, where the rate of relaxation ($1/\lambda$) is much greater than the rate of deformation ($\dot{\gamma}_0$), and the system remains in a near-equilibrium state. The linear viscoelasticity of the material is probed over a range of Deborah numbers (in practice by varying ω). In this regime, the measured stress is proportional to the strain amplitude and will have a component in-phase and out-of-phase with the oscillatory strain^{17,69}.

Complex fluids are also subjected to strong deformations, where Wi is not small and nonlinear stress responses are observed. Here, the stress is not proportional to the strain amplitude. For example, large amplitude oscillatory shear (LAOS) has gained recent interest as a means of char-

acterizing the nonlinear, transient stress response of complex fluids; for a sinusoidal input strain one often observes stress waveforms with multiple frequency overtones^{70,71}. The LAOS regime requires that the rate of deformation is comparable to or larger than the rate of relaxation, $Wi > 1$. Furthermore, the strain amplitude, $\gamma_0 = Wi/De$, cannot be small. If $Wi/De \ll 1$, the rate of oscillation is much greater than the rate of deformation and the resulting material response is linear in the strain amplitude⁷². LAOS experiments can be used to determine the nonlinear model parameters of constitutive equations, such as the Giesekus model^{37,73}, the Doi-Edwards model⁷⁴, and the Phan-Thien/Tanner model⁷⁵. LAOS can also be utilized to measure the degree of long chain branching in polymer melts, where branching causes a resistance to the stretching of a polymer, or strain hardening³³. The combination of LAOS and 2D-SAXS allows for the kinetic study of the orientation/reorientation in microphase-separated lamellae of block copolymers^{76,77}. Furthermore, LAOS can be utilized to probe the dynamics of shear banding in soft entangled materials, such as worm-like micelle solutions^{37,38,78}.

However, it is unclear how to utilize the information obtained from a LAOS experiment to predict the material stress response under other transient, nonlinear deformations. The primary goal of the present paper is to address this issue. In the SAOS regime, one can determine the linear relaxation modulus from either the in-phase or out-of-phase shear stress response via an inverse Fourier transform¹⁷. The linear relaxation modulus can then be utilized to determine the stress response under any small amplitude deformation history⁶⁵. Beyond the small amplitude regime, the stress response is strongly dependent on flow type. For example, a dilute suspension of orientable particles will exhibit shear thinning behavior, but also extensional thickening of the effective viscosity⁷⁹. Therefore, one should not expect the response of a material subject to LAOS to be directly applicable to predicting the response in other transient, nonlinear deformations. Thus, our goal is to develop a framework for translating LAOS data to other time dependent deformations, which would naturally broaden the utility of LAOS. This could be beneficial, for example, in polymer melt processing, where the processibility of a new melt is empirically tested using industrial-scale equipment along the entire process, which includes transient, large amplitude shear and extensional

flows¹⁶.

One approach to modeling the nonlinear transient stress response of a complex fluid is to utilize the co-rotational memory integral expansion^{65,80}, which is applicable to “simple fluids”⁸¹. A simple fluid satisfies four postulates: 1) the stress in a material element is solely dependent on the past deformation of that material element; 2) the stress-deformation relationship is independent of a rigid-body rotation (material frame indifference); 3) the material has a fading memory; and 4) the material is isotropic at rest. Many constitutive equations satisfy these postulates, such as the second-order fluid model, co-rotational Jeffreys model, Oldroyd eight-constant model, and the Giesekus model^{1,65,82}. Liquid crystalline materials, for example, would not be considered a simple fluid as they are non-isotropic at equilibrium. The stress from the co-rotational memory integral expansion is a function of the rate of strain tensor (in a co-rotational frame of reference) and nonlinear relaxation moduli, which are, in general, unknown for specific materials or constitutive equations. The main result of our work is a general methodology for determining the first nonlinear relaxation modulus from a medium amplitude oscillatory shear (MAOS) deformation. The MAOS regime is defined by small Weissenberg number, $Wi \ll 1$, where the shear stress scales as Wi and the normal stress differences scale as Wi^2 ; hence, the stress is asymptotically expanded in Wi ^{83,84}. We showcase our approach for a micro-mechanical model system composed of a dilute suspension of rigid, Brownian spheroids homogeneously dispersed in a Newtonian fluid. For this model system, we demonstrate that a dual-frequency MAOS deformation can exactly recover the first nonlinear relaxation modulus, referred to here as the MAOS relaxation modulus. Importantly, we suggest that our methodology is not limited to this specific micro-mechanical model; in particular, it could be used for other micro-mechanical models, constitutive relations, or experimental data.

This article is organized as follows. In Section 3.2 the pertinent information regarding the co-rotational memory integral expansion is reviewed. In Section 3.3 we detail the general methodology for determining the MAOS relaxation modulus from a dual-frequency MAOS deformation using specific calculations for our model system of Brownian spheroids. Using the MAOS relaxation modulus, we reconstruct the stress response of our model system for the start-up and cessation

of simple shear and uniaxial extension. In Section 3.5 we discuss the experimental feasibility and general applicability of our methodology.

3.2 Memory Integral Expansion and Nonlinear Viscoelasticity

In order to predict the nonlinear stress response of a material, a nonlinear constitutive equation that relates the material stress response to the deformation history is required. This can be achieved by utilizing a co-rotational memory integral expansion⁶⁵,

$$\begin{aligned} \boldsymbol{\tau}(\mathbf{x}, t) = & 2 \int_{-\infty}^t G_I(t-t') \check{\mathbf{E}}' dt' + 2 \int_{-\infty}^t \int_{-\infty}^t G_{II}(t-t', t-t'') (\check{\mathbf{E}}' \cdot \check{\mathbf{E}}'' + \check{\mathbf{E}}'' \cdot \check{\mathbf{E}}') dt'' dt' \\ & + 4 \int_{-\infty}^t \int_{-\infty}^t \int_{-\infty}^t \left[2 G_{III}(t-t', t-t'', t-t''') (\check{\mathbf{E}}' : \check{\mathbf{E}}'') \check{\mathbf{E}}''' \right. \\ & \left. + G_{IV}(t-t', t-t'', t-t''') (\check{\mathbf{E}}' \cdot \check{\mathbf{E}}'' \cdot \check{\mathbf{E}}''' + \check{\mathbf{E}}''' \cdot \check{\mathbf{E}}'' \cdot \check{\mathbf{E}}') \right] dt''' dt'' dt' + \dots, \end{aligned} \quad (3.1)$$

where $\boldsymbol{\tau}(\mathbf{x}, t)$ is the deviatoric stress at the current position \mathbf{x} of a material element at time t ; $G_I, G_{II}, G_{III}, \dots$ are relaxation moduli, which are material parameters and independent of the imposed deformation; $\check{\mathbf{E}}$ is the rate of strain tensor in a co-rotating frame of reference (Figure 3.1); and t', t'', t''', \dots are sequential past times in the deformation history ($-\infty < t''' \leq t'' \leq t' < t$). The nonlinearity in (3.1) arises due to the contractions of the co-rotational rate of strain tensors. The co-rotational rate of strain tensor is,

$$\check{\mathbf{E}}' = \check{\mathbf{E}}(\mathbf{x}, t, t') = \mathbf{R}(\mathbf{x}, t, t') \cdot \mathbf{E}(\mathbf{x}, t') \cdot \mathbf{R}^T(\mathbf{x}, t, t'), \quad (3.2)$$

where the superscript “ T ” denotes the matrix transpose and $\mathbf{E}(\mathbf{x}, t')$ is the rate of strain tensor in a fixed Cartesian frame,

$$\mathbf{E}(\mathbf{x}, t') = \frac{1}{2} \left[\nabla \mathbf{v}(\mathbf{x}, t') + (\nabla \mathbf{v}(\mathbf{x}, t'))^T \right]. \quad (3.3)$$

Here, $\mathbf{v}(\mathbf{x}, t')$ is the velocity of a fluid element in a fixed Cartesian frame at past time t' . Finally, \mathbf{R} is a matrix that describes the rotation of a fluid element \mathbf{x} from time t' to t . The rotation matrix

is defined as,

$$\begin{aligned} \mathbf{R}(\mathbf{x}, t, t') = & \mathbf{I} - \int_{t'}^t \boldsymbol{\Omega}'' dt'' + \int_{t'}^t \int_{t''}^t \boldsymbol{\Omega}''' \cdot \boldsymbol{\Omega}'' dt''' dt'' \\ & - \int_{t'}^t \int_{t''}^t \int_{t'''}^t \boldsymbol{\Omega}^{iv} \cdot \boldsymbol{\Omega}''' \cdot \boldsymbol{\Omega}'' dt^{iv} dt''' dt'' + \dots \end{aligned} \quad (3.4)$$

Here, \mathbf{I} is the identity matrix and $\boldsymbol{\Omega}'' = \boldsymbol{\Omega}(\mathbf{x}, t'')$ is the vorticity tensor ($\nabla \mathbf{v} = \mathbf{E} + \boldsymbol{\Omega}$) of a fluid element at a past time t'' .

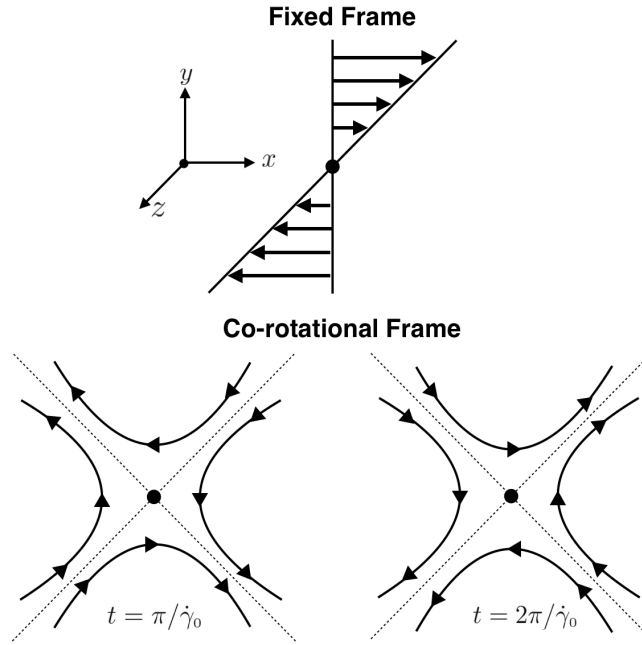


Figure 3.1: Sketch of velocity streamlines for steady simple shear in a fixed frame ($\mathbf{v} = \dot{\gamma}_0 y \mathbf{e}_x$) and co-rotational frame ($\mathbf{v} = (\dot{\gamma}_0/2)[(x \sin(\dot{\gamma}_0 t) + y \cos(\dot{\gamma}_0 t)) \mathbf{e}_x + (x \cos(\dot{\gamma}_0 t) - y \sin(\dot{\gamma}_0 t)) \mathbf{e}_y]$). An observer in the co-rotational frame of reference moves with the local fluid vorticity, ensuring that the reported stress is independent of a rigid-body rotation⁶⁵. In steady shear the observer sees a time dependent extensional flow that oscillates with period $2\pi/\dot{\gamma}_0$.

Equation (3.1) is capable of describing rheological phenomena for many “simple fluids,” as discussed above, including materials of practical interest: e.g. colloidal dispersions or polymer solutions. However, the main challenge is in determining – either experimentally or theoretically – the relaxation moduli for a given material. In the linear viscoelastic regime, $Wi \ll 1$, (3.4) can

be approximated as the identity matrix, to leading order. Thus, (3.1) simplifies to,

$$\boldsymbol{\tau}(t) = 2 \int_{-\infty}^t G_I(t-t') \mathbf{E}(t') dt' + O(|\mathbf{E}|^2), \quad (3.5)$$

where G_I is commonly known as the linear relaxation modulus, which can be determined from a small amplitude oscillatory shear (SAOS) deformation with rate of strain tensor,

$$\mathbf{E}(t') = \frac{\dot{\gamma}_0}{2} \cos(\omega t') (\mathbf{e}_x \mathbf{e}_y + \mathbf{e}_y \mathbf{e}_x), \quad (3.6)$$

where \mathbf{e}_x , \mathbf{e}_y , and \mathbf{e}_z are Cartesian unit vectors in the flow, flow-gradient, and vorticity directions, respectively. Substitution of (3.6) into (3.5) yields for the shear stress,

$$\tau_{yx} = \dot{\gamma}_0 \left[\eta'(\omega) \cos(\omega t) + \eta''(\omega) \sin(\omega t) \right] + O(\dot{\gamma}_0^2), \quad (3.7)$$

where,

$$\eta'(\omega) = \int_0^{\infty} G_I(s) \cos(\omega s) ds, \quad (3.8)$$

and

$$\eta''(\omega) = \int_0^{\infty} G_I(s) \sin(\omega s) ds. \quad (3.9)$$

Here, $\eta'(\omega)$ and $\eta''(\omega)$ are the real and imaginary components of the complex viscosity and are related to the viscous and elastic nature of the material, respectively. The relations in (3.8) and (3.9) are the Fourier cosine and sine transforms, respectively, of the linear relaxation modulus. Therefore, the shear stress response from a SAOS deformation can be used to determine the linear relaxation modulus by an inverse Fourier cosine (sine) transform of the out-of-phase (in-phase)

Table 3.1: Viscometric functions for three steady flows determined from (3.1). The fluid velocity is defined as follows. Simple shear, $\mathbf{v} = \dot{\gamma}_0(y, 0, 0)$; planar extension, $\mathbf{v} = \dot{\epsilon}(x/2, -y/2, 0)$; and uniaxial extension, $\mathbf{v} = (\dot{\epsilon}/2\sqrt{3})(-x, -y, 2z)$. The viscosity is defined in (3.11) and the normal stress differences, N_1 and N_2 , are defined as, $N_1 = \tau_{xx} - \tau_{yy}$ and $N_2 = \tau_{yy} - \tau_{zz}$. The linear relaxation modulus, G_I , only gives the leading order expression for these functions. The MAOS relaxation modulus, G_{II} , provides a correction to N_2 in simple shear and μ_e in uniaxial extension.

Steady Flow	Viscometric Function
Simple Shear	$\mu = \int_0^\infty G_I(s) \cos(\dot{\gamma}_0 s) ds + O(\dot{\gamma}_0^2)$ $N_1 = 2\dot{\gamma}_0 \int_0^\infty G_I(s) \sin(\dot{\gamma}_0 s) ds + O(\dot{\gamma}_0^3)$ $N_2 = -\dot{\gamma}_0 \int_0^\infty G_I(s) \sin(\dot{\gamma}_0 s) ds + \dot{\gamma}_0^2 \int_0^\infty \int_0^\infty G_{II}(s, q) \cos[\dot{\gamma}_0(q - s)] dq ds + O(\dot{\gamma}_0^3)$
Planar Extension	$\mu_e = \int_0^\infty G_I(s) ds + O(\dot{\epsilon}^2)$
Uniaxial Extension	$\mu_e = \int_0^\infty G_I(s) ds + \frac{\dot{\epsilon}}{\sqrt{3}} \int_0^\infty \int_0^\infty G_{II}(s, q) dq ds + O(\dot{\epsilon}^2)$

frequency-dependent stress response. That is,

$$G_I(s) = \frac{2}{\pi} \int_0^\infty \eta'(\omega) \cos(\omega s) d\omega = \frac{2}{\pi} \int_0^\infty \eta''(\omega) \sin(\omega s) d\omega. \quad (3.10)$$

The results from SAOS (η' or η'') can be utilized to recover $G_I(t)$, which can then be used in (3.5) to determine the material stress response to an arbitrary small amplitude deformation history. However, the linear relaxation modulus cannot describe the stress response beyond the small amplitude limit. For example, Table 3.1 shows the relevant viscometric functions for three steady flows: simple shear, planar extension, and uniaxial extension, as calculated from (3.1). The viscosity of each flow is defined as,

$$\mu = \frac{\boldsymbol{\tau} : \mathbf{E}}{2(\mathbf{E} : \mathbf{E})} \quad (3.11)$$

where $\sqrt{2(\mathbf{E} : \mathbf{E})}$ is the characteristic rate of deformation, which is the strain-rate amplitude, $\dot{\gamma}_0$, for shear flow and the rate of extension, $\dot{\epsilon}$, for extensional flows⁷⁹. It is evident that the linear relaxation modulus, G_I , gives the leading order terms of the second normal stress difference in shear and the extensional viscosity from uniaxial extension. However, the MAOS relaxation modulus, G_{II} , is required to determine higher order contributions in the strain-rate amplitude. A general methodology to determine G_{II} , from a MAOS deformation, is the main outcome of this work. Note that Table 3.1 gives the steady viscometric functions for three idealized flows that are convenient for experimental testing. However, in practical applications one would likely have mixed, transient flows for which, in general, G_{II} provides the first nonlinear stress response.

The linear relaxation modulus, which is a function of a single past time of the deformation history, can be determined from (3.5)-(3.10) via a single frequency-dependent input strain and 1-D inverse Fourier Transform, as discussed above. From (3.1), it is evident that the next term in the co-rotational memory integral expansion requires a relaxation modulus that is a function of *two* independent past times of the deformation history, $G_{II}(t-t', t-t'')$. Therefore, we require a deformation that oscillates at two independent frequencies, such that a two-dimensional inverse Fourier Transform can be applied. We will consider a parallel superposition, dual-frequency oscillatory shear deformation,

$$\mathbf{E}(t') = \frac{\dot{\gamma}_0}{2} \left[\cos(\omega_1 t') + \cos(\omega_2 t') \right] (\mathbf{e}_x \mathbf{e}_y + \mathbf{e}_y \mathbf{e}_x), \quad (3.12)$$

where ω_1 and ω_2 are chosen such that the flow is described by a single strain-rate amplitude, $\dot{\gamma}_0 = \gamma_1 \omega_1 = \gamma_2 \omega_2$. Here, γ_1 and γ_2 are the individual harmonic strain amplitudes, such that the overall strain is given by, $\gamma(t) = \gamma_1 \sin(\omega_1 t) + \gamma_2 \sin(\omega_2 t)$.

When a linear amplifier is subjected to an input oscillation at two frequencies, ω_1 and ω_2 , the output response will oscillate at the frequencies ω_1 and ω_2 . However, a nonlinear amplifier will have both a linear and nonlinear output response. The linear response will, again, oscillate at the applied frequencies ω_1 and ω_2 . In contrast, the nonlinear response will oscillate at twice the applied

frequencies, $2\omega_1$ and $2\omega_2$, along with oscillations at “combination tones,” $\omega_1 \pm \omega_2$. This phenomena is commonly observed in musical instruments and the cochlea of the inner ear^{85,86}. Complex fluids, when subjected to an oscillating input strain above a critical strain amplitude, also exhibit a nonlinear stress response. This is observed, for instance, in electrorheological (ER) fluids⁸⁷, solutions of tri-block copolymers⁸⁸, and suspensions of worm-like micelles⁸⁹. In the following sections we demonstrate that it is the stress response of a complex fluid at these combination tones that allow one to determine the MAOS relaxation modulus. Briefly, the general methodology for determining the MAOS relaxation modulus, G_{II} , is: 1) Evaluate the co-rotational memory integral expansion in (3.1) for a dual-frequency MAOS deformation (Section 3.3.1); 2) Calculate (or measure) the shear stress and second normal stress difference of the material subjected to a dual-frequency MAOS deformation (Section 3.3.2); 3) Compare the calculated (or measured) stress response to the co-rotational memory integral expansion to determine G_I and G_{II} (Section 3.3.3). Once the relaxation moduli are determined, one can then predict nonlinear rheological properties in other transient flows (Section 3.4).

Before continuing, we note that a co-rotational frame of reference is not the only objective frame that can be used in a memory integral expansion. One can also use a co-deformational (or convective) memory integral expansion⁹⁰⁻⁹² for which the stress is,

$$\begin{aligned} \boldsymbol{\tau}(\mathbf{x}, t) = & \int_{-\infty}^t G_I(t-t') \boldsymbol{\gamma}^{[1]'} dt' + \\ & \frac{1}{2} \int_{-\infty}^t \int_{-\infty}^t G_{II}(t-t', t-t'') \left(\boldsymbol{\gamma}^{[1]'} \cdot \boldsymbol{\gamma}^{[1]''} + \boldsymbol{\gamma}^{[1]''} \cdot \boldsymbol{\gamma}^{[1]'} \right) dt'' dt' + \\ & \frac{1}{2} \int_{-\infty}^t \int_{-\infty}^t \int_{-\infty}^t \left[2G_{III}(t-t', t-t'', t-t''') \boldsymbol{\gamma}^{[1]'} \left(\boldsymbol{\gamma}^{[1]''} : \boldsymbol{\gamma}^{[1]'''} \right) \right. \\ & \left. + G_{IV}(t-t', t-t'', t-t''') \left(\boldsymbol{\gamma}^{[1]'} \cdot \boldsymbol{\gamma}^{[1]''} \cdot \boldsymbol{\gamma}^{[1]'''} + \boldsymbol{\gamma}^{[1]'''} \cdot \boldsymbol{\gamma}^{[1]''} \cdot \boldsymbol{\gamma}^{[1]'} \right) \right] dt''' dt'' dt' + \dots, \end{aligned} \quad (3.13)$$

where, $\boldsymbol{\gamma}^{[1]'} = \boldsymbol{\gamma}^{[1]}(\mathbf{x}, t, t')$ is the rate of strain tensor in a frame of reference deforming with a fluid element⁶⁵. For example, for a transient shear flow of the form $v_x = f(t)y$, $v_y = v_z = 0$, the

co-deformational rate of strain tensor is,

$$\gamma^{[1]'} = f(t') \left(\mathbf{e}_x \mathbf{e}_y + \mathbf{e}_y \mathbf{e}_x + 2 \mathbf{e}_y \mathbf{e}_y \int_t^{t'} f(s) ds \right). \quad (3.14)$$

For a dual-frequency MAOS deformation, the shear stress and second normal stress difference from the co-rotational and co-deformational memory integral expansions are equivalent to $O(Wi^2)$ in the weakly nonlinear regime. In the following sections, we demonstrate that the linear and MAOS relaxation moduli are determined from the shear stress and second normal stress difference, respectively. Therefore, one can determine the linear and MAOS relaxation moduli by using the memory integral expansion in either frame of reference, since both will recover the same results. However, when predicting the stress response, the choice of frame of reference becomes important.

Both expansions represent the stress of a rheologically simple fluid and will predict the same stress response if an infinite number of terms in the expansions could be retained. Obviously, this is impractical and only a finite number of terms in either expansion can be retained (or even obtained), resulting in a different stress response for each expansion, as the scalar products of the rate of strain tensors in each frame of reference are, in general, unequal. The convergence properties of (3.1) and (3.13) were analyzed by Bird et al.⁹³ for a dilute suspension rigid dumbbells in steady simple shear and steady uniaxial extension. They found that the co-rotational memory integral expansion has a higher rate of convergence than the co-deformational memory integral expansion under both flow conditions; that is, fewer relaxation moduli in the co-rotational expansion, compared to the co-deformational expansion, are required to achieve a qualitatively accurate result, compared to a numerical approximation⁹⁴. We suggest that the co-rotational frame of reference in (3.1) might be best suited for materials composed of a rigid microstructure, such as rigid Brownian spheroids, considered herein, where the particles are affected by the rotation and strain of the imposed flow, but are incapable of stretching. Whereas, the co-deformational frame of reference in (3.13) might be best suited for materials composed of a deformable microstructure, such as a polymer solution, where the flexible polymer chains are also capable to stretch or deform under an imposed flow.

3.3 General Framework

3.3.1 Co-rotational Memory Integral Expansion for Dual-Frequency MAOS

The rotation matrix, $\mathbf{R}(\mathbf{x}, t, t')$ for a homogenous, unsteady shear flow of the form $v_x(t) = f(t)y$, $v_y = v_z = 0$ is⁶⁵,

$$\begin{aligned} \mathbf{R}(t, t') = & \cos\left(\frac{1}{2}\int_{t'}^t f(s)ds\right) (\mathbf{e}_x\mathbf{e}_x + \mathbf{e}_y\mathbf{e}_y) + \\ & \sin\left(\frac{1}{2}\int_{t'}^t f(s)ds\right) (\mathbf{e}_x\mathbf{e}_y - \mathbf{e}_y\mathbf{e}_x) + \mathbf{e}_z\mathbf{e}_z. \end{aligned} \quad (3.15)$$

For a dual-frequency MAOS deformation, $f(t) = \dot{\gamma}_0 [\cos(\omega_1 t) + \cos(\omega_2 t)]$ and (3.15) becomes,

$$\mathbf{R}(t, t') = \cos\left(\frac{\dot{\gamma}_0}{2}P'\right) (\mathbf{e}_x\mathbf{e}_x + \mathbf{e}_y\mathbf{e}_y) + \sin\left(\frac{\dot{\gamma}_0}{2}P'\right) (\mathbf{e}_x\mathbf{e}_y - \mathbf{e}_y\mathbf{e}_x) + \mathbf{e}_z\mathbf{e}_z, \quad (3.16)$$

where

$$P' = P(t, t') = \frac{\sin(\omega_1 t) - \sin(\omega_1 t')}{\omega_1} + \frac{\sin(\omega_2 t) - \sin(\omega_2 t')}{\omega_2}. \quad (3.17)$$

Substitution of (3.12) and (3.16) into (3.2) yields the co-rotational rate-of-strain tensor for a dual-frequency MAOS deformation,

$$\check{\mathbf{E}}(t, t') = \frac{f(t')}{2} \left\{ \sin(\dot{\gamma}_0 P') (\mathbf{e}_x\mathbf{e}_x - \mathbf{e}_y\mathbf{e}_y) + \cos(\dot{\gamma}_0 P') (\mathbf{e}_x\mathbf{e}_y + \mathbf{e}_y\mathbf{e}_x) \right\}. \quad (3.18)$$

The shear stress, τ_{yx} , is determined by substituting (3.18) into (3.1) and performing a Taylor expansion about small strain amplitude ($\dot{\gamma}_0/\omega_1 \ll 1$ and $\dot{\gamma}_0/\omega_2 \ll 1$), yielding

$$\begin{aligned} \frac{\tau_{yx}}{\dot{\gamma}_0} = & \cos(\omega_1 t) \int_0^\infty G_I(s) \cos(\omega_1 s) ds + \sin(\omega_1 t) \int_0^\infty G_I(s) \sin(\omega_1 s) ds \\ & + \cos(\omega_2 t) \int_0^\infty G_I(s) \cos(\omega_2 s) ds + \sin(\omega_2 t) \int_0^\infty G_I(s) \sin(\omega_2 s) ds + O(\dot{\gamma}_0^2). \end{aligned} \quad (3.19)$$

Similarly, the second normal stress difference ($N_2 = \tau_{yy} - \tau_{zz}$) is determined from (3.1) and (3.18) as,

$$\begin{aligned}
N_2(\omega_1, \omega_2, t) = & F_0(\omega_1, \omega_2) \\
& + F_1(\omega_1, \omega_2) \cos(2\omega_1 t) + H_1(\omega_1, \omega_2) \sin(2\omega_1 t) \\
& + F_2(\omega_1, \omega_2) \cos(2\omega_2 t) + H_2(\omega_1, \omega_2) \sin(2\omega_2 t) \\
& + F_3(\omega_1, \omega_2) \cos [(\omega_1 + \omega_2)t] + H_3(\omega_1, \omega_2) \sin [(\omega_1 + \omega_2)t] \\
& + F_4(\omega_1, \omega_2) \cos [(\omega_1 - \omega_2)t] + H_4(\omega_1, \omega_2) \sin [(\omega_1 - \omega_2)t] + O(\dot{\gamma}_0^3),
\end{aligned} \tag{3.20}$$

where F_i and H_i are scalar coefficients that depend on the input frequencies, ω_1 and ω_2 , and the relaxation moduli. Full expressions for these coefficients can be found in Appendix 3.A.1. The relevant coefficient, for the purposes of this work, is the term proportional to the combination tone $\cos[(\omega_1 + \omega_2)t]$; specifically,

$$\begin{aligned}
\frac{F_3}{\dot{\gamma}_0/2} = & \left(\frac{1}{\omega_1} + \frac{1}{\omega_2} \right) \int_0^\infty G_I(s) \sin [(\omega_1 + \omega_2)s] \mathbf{d}s - \int_0^\infty G_I(s) \left(\frac{\sin(\omega_2 s)}{\omega_1} + \frac{\sin(\omega_1 s)}{\omega_2} \right) \mathbf{d}s \\
& + \int_0^\infty \int_0^\infty G_{II}(s, q) \left[\cos(\omega_1 s + \omega_2 q) + \cos(\omega_1 q + \omega_2 s) \right] \mathbf{d}s \mathbf{d}q
\end{aligned} \tag{3.21}$$

The first two terms in equation (3.21) depend on the linear relaxation modulus, which can be determined from the shear stress response in (3.19). The last term in equation (3.21) is the summation of two two-dimensional Fourier cosine transforms of G_{II} . Therefore, G_{II} can be determined from a two-dimensional inverse Fourier cosine transform of the scalar function F_3 , less the dependence on G_I , as detailed in Section 3.A.3,

$$G_{II}(s, q) = \frac{4}{\pi^2} \int_0^\infty \int_0^\infty \mathcal{F}(\omega_1, \omega_2) \left[\cos(\omega_1 s + \omega_2 q) + \cos(\omega_2 s + \omega_1 q) \right] \mathbf{d}\omega_2 \mathbf{d}\omega_1, \tag{3.22}$$

where,

$$\begin{aligned} \mathcal{F} = & \frac{F_3}{\dot{\gamma}_0/2} + \int_0^\infty G_I(s) \left(\frac{\sin(\omega_2 s)}{\omega_1} + \frac{\sin(\omega_1 s)}{\omega_2} \right) ds \\ & - \left(\frac{1}{\omega_1} + \frac{1}{\omega_2} \right) \int_0^\infty G_I(s) \sin[(\omega_1 + \omega_2)s] ds. \end{aligned} \quad (3.23)$$

The key point is that it is the second normal stress difference in simple shear that contains information about G_{II} . Therefore, one requires the ability to determine the second normal stress difference under a dual-frequency MAOS deformation in order to recover G_{II} for a given material. A complimentary analysis, where the overall strain is the difference between two independent sinusoidal strains, $\gamma = \gamma_1 \sin(\omega_1 t) - \gamma_2 \sin(\omega_2 t)$, can be utilized to recover the same MAOS relaxation modulus. In this case, the relevant coefficient is $F_4(\omega_1, \omega_2)$, but the subsequent analysis would remain unchanged. Next, we determine the stress response of a dilute suspension of Brownian spheroids subject to a dual-frequency MAOS deformation; specifically, the shear stress and second normal stress difference.

3.3.2 Micromechanics of a Dilute Suspension of Rigid Spheroids

Problem Set-up

The model system utilized is a dilute, homogeneous ensemble of force and couple-free, Brownian, rigid spheroids in a Newtonian fluid of viscosity μ_s and density ρ . The spheroidal particles are characterized by an aspect ratio, r , defined as the ratio of the major (ℓ) to minor (a) axes, $r = \ell/a$. The hydrodynamic sphericity of the particles is characterized by the Bretherton constant,

$$B = \frac{r^2 - 1}{r^2 + 1}, \quad (3.24)$$

which is positive for prolate spheroids, negative for oblate spheroids, and zero for spheres. The suspension is assumed to be dilute, $c = 4\pi n \ell a^2 / 3 \ll 1$, where c is the particle volume fraction and n is the number density of particles, such that interparticle interactions can be neglected.

The stochastic nature of the Brownian forces on the spheroidal particles requires a statistical description of the microstructure. A useful measure is the orientation distribution function, $\psi(\mathbf{p}, t)$, where the quantity $\psi(\mathbf{p}, t) \sin \theta d\theta d\phi$ represents the probability of finding a particle ensemble in a differential region about (θ, ϕ) ^{11,12,65}. Here, \mathbf{p} is the orientation unit vector parameterized in spherical polar coordinates. The orientation distribution function satisfies a conservation, or Fokker-Planck, equation,

$$\frac{\partial \psi}{\partial t} + \nabla_{\mathbf{p}} \cdot (\dot{\mathbf{p}} \psi) = 0, \quad (3.25)$$

where $\nabla_{\mathbf{p}}$ is the surface gradient operator and $\dot{\mathbf{p}}$ is the temporal evolution of the particle orientation^{12,13},

$$\dot{\mathbf{p}} = B(\mathbf{I} - \mathbf{p}\mathbf{p}) \cdot \mathbf{H} \cdot \mathbf{p} - D_r \nabla_{\mathbf{p}} \ln \psi. \quad (3.26)$$

Here, \mathbf{I} is the identity matrix, D_r is the rotary diffusion coefficient, and $\mathbf{H} = B^{-1}\boldsymbol{\Omega} + \mathbf{E}$. For a dual-frequency MAOS deformation, $\mathbf{H} = \dot{\gamma}_0 [\cos(\alpha\tau) + \cos(\beta\tau)] \mathbf{G}$, where,

$$\mathbf{G} = \frac{1}{2} \left[(1 - B^{-1}) \mathbf{e}_x \mathbf{e}_y + (1 + B^{-1}) \mathbf{e}_y \mathbf{e}_x \right] \quad (3.27)$$

and α and β are the oscillation frequencies scaled by the rotary diffusion coefficient ($\alpha = \omega_1/D_r$, $\beta = \omega_2/D_r$), and τ is dimensionless time ($\tau = t D_r$). A dimensionless conservation equation can be obtained by normalizing \mathbf{H} by the shear rate amplitude ($\tilde{\mathbf{H}} = \mathbf{H}/\dot{\gamma}_0$). Furthermore, substitution of (3.26) into (3.25) yields,

$$\frac{\partial \psi}{\partial \tau} + Wi \nabla_{\mathbf{p}} \cdot \left[(\mathbf{I} - \mathbf{p}\mathbf{p}) \cdot \tilde{\mathbf{H}} \cdot \mathbf{p} \psi \right] = \nabla_{\mathbf{p}}^2 \psi, \quad (3.28)$$

where $Wi = B\dot{\gamma}_0/D_r$ is a Weissenberg number whose magnitude describes the extent to which the system is disturbed from equilibrium by the imposed deformation. Note that Wi is signed because of its dependence on B , where $B = [-1, 1]$. At small $|Wi|$, where Brownian rotation acts on a faster time scale than the imposed flow, the particle orientation is nearly uniform. At large $|Wi|$, the imposed flow acts on a faster time scale than Brownian rotation and the particles

essentially follow Jeffery orbits in the imposed flow, leading to a highly non-uniform orientation distribution¹⁰. Finally, the orientation distribution function satisfies the normalization condition,

$$\int_0^{2\pi} \int_0^\pi \psi(\mathbf{p}, \tau) \sin \theta d\theta d\phi = 1. \quad (3.29)$$

Regular Perturbation Expansion

The conservation equation (3.28) is to be addressed in the limit of weak deformation rate, $|Wi| \ll 1$. In this regime, the system is only slightly disturbed by the imposed deformation and Brownian rotation dominates to achieve a near-equilibrium microstructure. Therefore, the orientation distribution function can be written as a regular perturbation expansion about small Wi ,

$$\psi(\mathbf{p}, t) = \frac{1}{4\pi} \left(1 + Wi \psi_1 + Wi^2 \psi_2 \right) + O(Wi^3), \quad (3.30)$$

where ψ_1 and ψ_2 represent the linear and weakly nonlinear departures from equilibrium, respectively. Substitution of (3.30) into (3.28) yields a hierarchy of equations for each term in the expansion⁹⁵,

$$\frac{\partial \psi_i}{\partial \tau} - \nabla_{\mathbf{p}} \cdot \frac{\partial \psi_i}{\partial \mathbf{p}} + 2\mathbf{p} \cdot \frac{\partial \psi_i}{\partial \mathbf{p}} = (\mathbf{p}\mathbf{p} : \mathbf{H}) \left(3\psi_{i-1} + \mathbf{p} \cdot \frac{\partial \psi_{i-1}}{\partial \mathbf{p}} \right) - (\mathbf{H} \cdot \mathbf{p}) \cdot \frac{\partial \psi_{i-1}}{\partial \mathbf{p}}, \quad (3.31)$$

subject to,

$$\int_0^{2\pi} \int_0^\pi \psi_i \sin \theta d\theta d\phi = 0, \quad (3.32)$$

for $i = 1, 2, \dots$.

The linear solution to (3.31) ($i = 1$) should oscillate at the input frequencies, α and β , such that,

$$\psi_1 = f_{1,\alpha} e^{i\alpha\tau} + \hat{f}_{1,\alpha} e^{-i\alpha\tau} + f_{1,\beta} e^{i\beta\tau} + \hat{f}_{1,\beta} e^{-i\beta\tau}, \quad (3.33)$$

where hatted quantities indicate complex conjugates. Substitution of (3.33) into (3.31) yields,

$$\psi_1 = \left(h_1(\alpha)e^{i\alpha\tau} + \hat{h}_1(\alpha)e^{-i\alpha\tau} + h_1(\beta)e^{i\beta\tau} + \hat{h}_1(\beta)e^{-i\beta\tau} \right) \mathbf{pp} : \mathbf{G}, \quad (3.34)$$

where,

$$h_1(\alpha) = \frac{3}{2} \frac{6 - i\alpha}{\alpha^2 + 36}. \quad (3.35)$$

Unsurprisingly, the first order approximation to the orientation distribution function for a dual-frequency MAOS deformation is a linear superposition of the solution obtained for a single-frequency SAOS deformation at each frequency. Here, the material is acting as a ‘linear amplifier.’

Substitution of (3.34) into (3.31) for $i = 2$ yields,

$$\frac{\partial \psi_2}{\partial \tau} + (2\mathbf{p} - \nabla_{\mathbf{p}}) \cdot \frac{\partial \psi_2}{\partial \mathbf{p}} = h(\alpha, \beta, \tau) \left[\frac{5}{2} (\mathbf{pp} : \mathbf{S})^2 - (\mathbf{p} \cdot \mathbf{S} \cdot \mathbf{S} \cdot \mathbf{p}) - (\mathbf{p} \cdot \mathbf{S} \cdot \mathbf{A} \cdot \mathbf{p}) \right], \quad (3.36)$$

where,

$$\begin{aligned} h = & h_1(\alpha) \left(1 + e^{2i\alpha\tau} + e^{i(\alpha+\beta)\tau} + e^{i(\alpha-\beta)\tau} \right) + \hat{h}_1(\alpha) \left(1 + e^{-2i\alpha\tau} + e^{-i(\alpha+\beta)\tau} + e^{-i(\alpha-\beta)\tau} \right) \\ & + h_1(\beta) \left(1 + e^{2i\beta\tau} + e^{i(\alpha+\beta)\tau} + e^{-i(\alpha-\beta)\tau} \right) + \hat{h}_1(\beta) \left(1 + e^{-2i\beta\tau} + e^{-i(\alpha+\beta)\tau} + e^{i(\alpha-\beta)\tau} \right), \end{aligned} \quad (3.37)$$

and \mathbf{S} and \mathbf{A} are the symmetric and anti-symmetric components of \mathbf{G} , respectively. From (3.36) and (3.37) we postulate that ψ_2 to be of the form,

$$\psi_2 = f_{2,0} + f_{2,\alpha} e^{2i\alpha\tau} + f_{2,\beta} e^{2i\beta\tau} + f_{2,s} e^{i(\alpha+\beta)\tau} + f_{2,d} e^{i(\alpha-\beta)\tau} + \text{c.c.}, \quad (3.38)$$

where, ‘c.c.’ denotes complex conjugate solutions. Substitution of (3.38) into (3.36) yields,

$$\begin{aligned} \psi_2 = & T(\alpha, \beta, \tau) (\mathbf{S} : \mathbf{S}) + U(\alpha, \beta, \tau) (\mathbf{p} \cdot \mathbf{S} \cdot \mathbf{S} \cdot \mathbf{p}) \\ & + V(\alpha, \beta, \tau) (\mathbf{p} \cdot \mathbf{S} \cdot \mathbf{A} \cdot \mathbf{p}) + W(\alpha, \beta, \tau) (\mathbf{pp} : \mathbf{S})^2, \end{aligned} \quad (3.39)$$

where,

$$T(\alpha, \beta, \tau) = T_0 + T_\alpha e^{2i\alpha\tau} + T_\beta e^{2i\beta\tau} + T_s e^{i(\alpha+\beta)\tau} + T_d e^{i(\alpha-\beta)\tau} + \text{c.c.}, \quad (3.40)$$

and similarly for $U(\alpha, \beta, \tau)$, $V(\alpha, \beta, \tau)$, and $W(\alpha, \beta, \tau)$. Expressions for the scalar coefficients T_k , U_k , V_k , and W_k can be found in Section 3.A.2. Next, we utilize our asymptotic solution to the orientation distribution function to determine the deviatoric stress response arising from the particles.

Stress Response

The deviatoric stress due to the addition of particles (τ^p) is determined from an ensemble average of the stresslet¹²,

$$\begin{aligned} \frac{\tau^p}{2\mu_s c} = & 2A_H \mathbf{E} : \langle \mathbf{pppp} \rangle + 2B_H \left(\mathbf{E} \cdot \langle \mathbf{pp} \rangle + \langle \mathbf{pp} \rangle \cdot \mathbf{E} + \frac{2}{3} \mathbf{E} : \langle \mathbf{pp} \rangle \mathbf{I} \right) \\ & + C_H \mathbf{E} + F_H D_r \left(\langle \mathbf{pp} \rangle - \frac{1}{3} \mathbf{I} \right), \end{aligned} \quad (3.41)$$

where the angled brackets denote orientational averages,

$$\langle \mathbf{pp} \rangle = \int_0^{2\pi} \int_0^\pi \mathbf{pp} \psi(\mathbf{p}, \tau) \sin \theta d\theta d\phi, \quad (3.42)$$

and

$$\langle \mathbf{pppp} \rangle = \int_0^{2\pi} \int_0^\pi \mathbf{pppp} \psi(\mathbf{p}, \tau) \sin \theta d\theta d\phi. \quad (3.43)$$

The coefficients A_H , B_H , C_H , and F_H are known scalar functions of the particle aspect ratio^{11,12}.

Substitution of (3.34) and (3.39) into (3.41) yields,

$$\frac{\tau^p}{2\mu_s c \dot{\gamma}_0} = S_1 \tilde{\mathbf{E}} + Wi \left[S_2 (\tilde{\mathbf{E}} \cdot \tilde{\mathbf{E}}) + S_3 \left(\tilde{\mathbf{E}} \cdot \tilde{\mathbf{\Omega}} + \tilde{\mathbf{\Omega}}^T \cdot \tilde{\mathbf{E}} \right) \right] + O(Wi^2) \quad (3.44)$$

where, $\tilde{\mathbf{E}}$ and $\tilde{\mathbf{\Omega}}$ are the spatial components of the rate of strain and vorticity tensors, respectively, defined as,

$$\mathbf{E} = \dot{\gamma}_0 [\cos(\alpha\tau) + \cos(\beta\tau)] \tilde{\mathbf{E}} \quad (3.45)$$

and

$$\mathbf{\Omega} = \dot{\gamma}_0 [\cos(\alpha\tau) + \cos(\beta\tau)] \tilde{\mathbf{\Omega}}. \quad (3.46)$$

For a shear deformation, $\tilde{\mathbf{E}} = (\mathbf{e}_y\mathbf{e}_x + \mathbf{e}_x\mathbf{e}_y)/2$ and $\tilde{\mathbf{\Omega}} = (\mathbf{e}_y\mathbf{e}_x - \mathbf{e}_x\mathbf{e}_y)/2$. The scalar coefficients in (3.44), S_1 , S_2 , and S_3 , are given by,

$$S_1 = \left(\frac{4A_H}{15} + \frac{4B_H}{3} + C_H \right) [\cos(\alpha\tau) + \cos(\beta\tau)] \quad (3.47)$$

$$+ \frac{2F_H B}{5} \left[\frac{6\cos(\alpha\tau) + \alpha\sin(\alpha\tau)}{\alpha^2 + 36} + \frac{6\cos(\beta\tau) + \beta\sin(\beta\tau)}{\beta^2 + 36} \right],$$

$$S_2 = \left(\frac{8A_H}{105} + \frac{4B_H}{15} \right) h(\alpha, \beta, \tau) + \frac{2F_H B}{105} (7U(\alpha, \beta, \tau) + 4W(\alpha, \beta, \tau)), \quad (3.48)$$

and

$$S_3 = \frac{F_H}{15} V(\alpha, \beta, \tau). \quad (3.49)$$

From (3.44) and (3.47)–(3.49) the shear stress is $S_1/2$ and the second normal stress difference is,

$$N_2 = \frac{\mu_s c \dot{\gamma}_0 Wi}{15} \left\{ \left(\frac{4A_H}{7} + 2B_H \right) h + F_H \left[B \left(U + \frac{4W}{7} \right) - V \right] \right\} + O(Wi^2), \quad (3.50)$$

which can be expanded as,

$$\begin{aligned} \frac{N_2}{\mu_s c \dot{\gamma}_0 W i} = & K_0 + K_1 \cos(2\alpha\tau) + L_1 \sin(2\alpha\tau) + K_2 \cos(2\beta\tau) + L_2 \sin(2\beta\tau) \\ & + K_3 \cos[(\alpha + \beta)\tau] + L_3 \sin[(\alpha + \beta)\tau] + K_4 \cos[(\alpha - \beta)\tau] + L_4 \sin[(\alpha - \beta)\tau], \end{aligned} \quad (3.51)$$

where K_i and L_i are frequency-dependent coefficients that can be determined from the definitions of $h(\alpha, \beta, \tau)$, $U(\alpha, \beta, \tau)$, $V(\alpha, \beta, \tau)$, and $W(\alpha, \beta, \tau)$ given in (3.37) and Section 3.A.2. From the co-rotational memory integral expansion, specifically (3.20) and (3.21), the relevant contribution to N_2 is the term proportional to $\cos[(\alpha + \beta)\tau]$; namely K_3 ,

$$\begin{aligned} K_3 = & \left(\frac{24A_H}{35} + \frac{12B_H}{5} \right) \frac{\alpha^2 + \beta^2 + 72}{(\alpha^2 + 36)(\beta^2 + 36)} \\ & + \frac{F_H}{5} \left(1 + \frac{3B}{7} \right) \left[\frac{2592 - \alpha\beta[(\alpha + \beta)^2 + 72]}{(\alpha^2 + 36)(\beta^2 + 36)[(\alpha + \beta)^2 + 36]} \right]. \end{aligned} \quad (3.52)$$

Now that the shear stress and second normal stress difference for a dilute suspension of Brownian spheroids subjected to a dual-frequency MAOS deformation have been determined, the linear and MAOS relaxation moduli of this material can be resolved.

3.3.3 Determining the Relaxation Moduli

From the co-rotational memory integral expansion, the shear stress is given by (3.19), which can be rewritten in terms of dimensionless time and frequency,

$$\begin{aligned} \frac{\tau_{yx}}{\dot{\gamma}_0/D_r} = & \cos(\alpha\tau) \int_0^\infty G_I(\tilde{s}) \cos(\alpha\tilde{s}) d\tilde{s} + \sin(\alpha\tau) \int_0^\infty G_I(\tilde{s}) \sin(\alpha\tilde{s}) d\tilde{s} \\ & + \cos(\beta\tau) \int_0^\infty G_I(\tilde{s}) \cos(\beta\tilde{s}) d\tilde{s} + \sin(\beta\tau) \int_0^\infty G_I(\tilde{s}) \sin(\beta\tilde{s}) d\tilde{s} + O(\dot{\gamma}_0^3), \end{aligned} \quad (3.53)$$

where, $\tilde{s} = (t - t')D_r$. The shear stress determined for the micro-mechanical model system is $S_1/2$, given in (3.47). Comparison of the terms proportional to $\cos(\alpha\tau)$ yields,

$$\int_0^\infty G_I(\tilde{s}) \cos(\alpha\tilde{s}) d\tilde{s} = \mu_s c D_r \left[\frac{4A_H}{15} + \frac{4B_H}{3} + C_H + \frac{2F_H B}{5} \left(\frac{6}{\alpha^2 + 36} \right) \right], \quad (3.54)$$

which is a one-dimensional Fourier Cosine transform of $G_I(\tilde{s})$. Thus, $G_I(\tilde{s})$ can be found by applying the inverse Fourier Cosine transform to the right-hand-side of (3.54), which yields

$$\frac{G_I(\tilde{s})}{\mu_s c D_r} = \left(\frac{8A_H}{15} + \frac{8B_H}{3} + 2C_H \right) \delta(\tilde{s}) + \frac{2F_H B}{5} e^{-6\tilde{s}}. \quad (3.55)$$

(3.55) has the functional form of a Jeffery's model, which is the three-element mechanical equivalent of a dashpot in series with a parallel dashpot and spring⁶⁵, where rotary diffusion is acting as the (entropic) spring.

The second normal stress difference defined from the co-rotational memory integral expansion is given in (3.20) and the term proportional to $\cos[(\alpha + \beta)\tau]$ is given by (3.21). Substitution of (3.55) into (3.21) and normalizing time and frequency by the rotary diffusion coefficient yields,

$$F_3 = \frac{\mu_s c \dot{\gamma}_0 W i F_H}{5} \left[\frac{2592 - \alpha\beta[72 + (\alpha + \beta)^2]}{(\alpha^2 + 36)(\beta^2 + 36)[(\alpha + \beta)^2 + 36]} \right] + \frac{\dot{\gamma}_0^2}{2D_r^2} \int_0^\infty \int_0^\infty G_{II}(\tilde{s}, \tilde{q}) \left[\cos(\alpha\tilde{s} + \beta\tilde{q}) + \cos(\alpha\tilde{q} + \beta\tilde{s}) \right] d\tilde{s} d\tilde{q}, \quad (3.56)$$

where, $\tilde{q} = (t - t'')D_r$. Equating (3.56) to the micro-mechanical model system result (3.52) yields,

$$\begin{aligned} & \frac{\mu_s c B D_r}{5} \left\{ \left(\frac{8A_H}{7} + 4B_H \right) \left(\frac{6}{\alpha^2 + 36} + \frac{6}{\beta^2 + 36} \right) \right. \\ & \quad \left. + \frac{3F_H B}{7} \left[\frac{2592 - \alpha\beta[(\alpha + \beta)^2 + 72]}{(\alpha^2 + 36)(\beta^2 + 36)[(\alpha + \beta)^2 + 36]} \right] \right\} \\ & = \int_0^\infty \int_0^\infty G_{II}(\tilde{s}, \tilde{q}) \left[\cos(\alpha\tilde{s} + \beta\tilde{q}) + \cos(\beta\tilde{s} + \alpha\tilde{q}) \right] d\tilde{s} d\tilde{q}. \end{aligned} \quad (3.57)$$

The MAOS relaxation modulus, G_{II} , can be resolved from the left-hand-side of (3.57) by applying

a symmetric two-dimensional inverse Fourier Transform, as detailed in Section 3.A.3. We require a symmetric transform as α and β are interchangeable, which is a result of prescribing a single strain-rate amplitude ($\dot{\gamma}_0 = \gamma_1\alpha D_r = \gamma_2\beta D_r$). The left-hand-side of (3.57) can be exactly inverted to yield,

$$G_{II}(\tilde{s}, \tilde{q}) = \frac{\mu_s c D_r B}{5} \left\{ \left[\left(\frac{16A_H}{7} + 8B_H \right) \delta(\tilde{s}) + \frac{3F_H B}{7} g(\tilde{s}, \tilde{q}) \right] e^{-6\tilde{q}} \right\}, \quad (3.58)$$

where,

$$g(\tilde{s}, \tilde{q}) = \begin{cases} 1 & \tilde{s} \leq \tilde{q} < \infty \\ 0 & 0 \leq \tilde{q} < \tilde{s} \end{cases}. \quad (3.59)$$

The condition in (3.59) arises because we require each additional past time in the deformation history to be sequentially further in the past ($t'' \leq t'$). The MAOS relaxation modulus, in the frequency and time domain, is depicted in Figure 3.2.

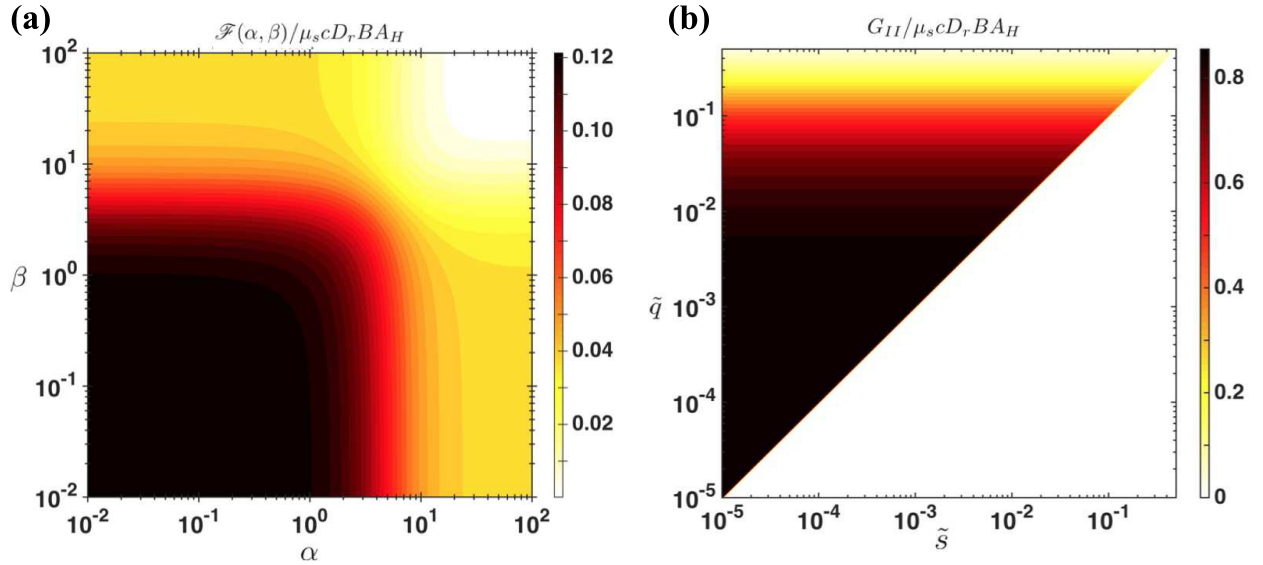


Figure 3.2: MAOS relaxation modulus of a dilute suspension of Brownian rods ($B = 1$) in (a): frequency-domain (left-hand-side of (3.57)) and (b): (dimensionless) time-domain, given in (3.58). In the frequency domain there is a symmetry about $\alpha = \beta$ since α and β are interchangeable. In the limit of large frequencies, we observe that the combination tone response decays to zero, indicating a linear material stress response. In the time domain we observe that G_{II} decays to 0 at long times and $G_{II} = 0$ for $\tilde{s} > \tilde{q}$, resulting from the constraint that all additional past times in the deformation history must be subsequently further in the past ($t'' \leq t'$).

Thus, we have shown that a dual-frequency MAOS deformation can be used to recover the first nonlinear relaxation modulus, G_{II} , which we call the MAOS relaxation modulus. The above result for G_{II} is given by Abdel-Khalik et al.⁶⁴ for the particular case of rods ($B = 1$), albeit using a different method than ours. They determined G_{II} , along with higher order moduli, by considering only irrotational flows for which the rate of strain tensor in a fixed and co-rotational reference frame are equivalent ($\mathbf{E} = \check{\mathbf{E}}$). However, if one were to use a co-deformational memory integral expansion, as mentioned previously, this simplification would not be valid as the co-deformational and fixed reference frame rate of strain tensors are not equivalent for an irrotational flow. Moreover, from an experimental perspective, their approach would require a nonlinear, transient extensional deformation, which is more difficult to obtain and maintain than an oscillatory shear deformation. In contrast, our methodology is not subject to such restrictions and thus can be utilized to determine the MAOS relaxation modulus – either theoretically or experimentally – for a variety of “simple fluids” via either memory integral expansion. Thus, we have not only generalized the results of Abdel-Khalik et al.⁶⁴ to spheroids of arbitrary aspect ratio, but we have also utilized this micro-mechanical model as a proof-of-concept for a general procedure of determining the MAOS relaxation modulus of a “simple fluid.” This allows MAOS data to be used for the prediction of the material stress response under arbitrary transient, weakly nonlinear deformations, which is exemplified in the following section.

3.4 Prediction of Nonlinear Stress Response from MAOS Relaxation Modulus

Now that we have determined the linear and MAOS relaxation moduli (G_I and G_{II}), we are able to predict the stress response of the model system to an arbitrary deformation via (3.1). However, it is not clear *a priori* as to what value of the strain-rate amplitude, Wi , this prediction gives accurate results, since, in principle, one requires many relaxation moduli⁹³. As a basis of comparison, a numerical solution to (3.28) for a transient linear flow is obtained by applying a Galerkin method^{79,96} and computing the stress tensor via (3.41).

3.4.1 Start-up and Cessation of Simple Shear Flow

The co-rotational rate of strain tensor for the start-up of simple shear ($\mathbf{v} = \dot{\gamma}_0 y \mathbf{e}_x$) at time $\tau = 0$ is,

$$\check{\mathbf{E}}^+(\tau, \tau') = \frac{\dot{\gamma}_0}{2} \left\{ \sin \left[\frac{\dot{\gamma}_0}{D_r} (\tau - \tau') \right] (\mathbf{e}_x \mathbf{e}_x - \mathbf{e}_y \mathbf{e}_y) + \cos \left[\frac{\dot{\gamma}_0}{D_r} (\tau - \tau') \right] (\mathbf{e}_x \mathbf{e}_y + \mathbf{e}_y \mathbf{e}_x) \right\}, \quad (3.60)$$

which is valid for $0 < \tau' < \tau$. The superscript '+' denotes the start-up condition. Substitution of (3.55), (3.58), and (3.60) into (3.1) yields,

$$\begin{aligned} \frac{\tau_{yx}^+}{2\mu_s c \dot{\gamma}_0} &= \frac{2A_H}{15} + \frac{2B_H}{3} + \frac{C_H}{2} \\ &+ \frac{F_H B}{30} \left\{ 1 - e^{-6\tau} \left[\cos \left(\frac{Wi}{B} \tau \right) - \frac{Wi}{6B} \sin \left(\frac{Wi}{B} \tau \right) \right] \right\} + O(Wi^2), \end{aligned} \quad (3.61)$$

$$\frac{N_1^+}{\mu_s c \dot{\gamma}_0} = \frac{F_H B}{45} \left\{ \frac{Wi}{B} - e^{-6\tau} \left[\frac{Wi}{B} \cos \left(\frac{Wi}{B} \tau \right) + 6 \sin \left(\frac{Wi}{B} \tau \right) \right] \right\} + O(Wi^3), \quad (3.62)$$

and

$$\begin{aligned} \frac{N_2^+}{\mu_s c \dot{\gamma}_0} &= \frac{-N_1^+}{2\mu_s c \dot{\gamma}_0} + Wi \left\{ \left(\frac{4A_H}{105} + \frac{B_H}{30} \right) \left(1 - e^{-6\tau} \left[\cos \left(\frac{Wi}{B} \tau \right) + \frac{Wi}{6B} \sin \left(\frac{Wi}{B} \tau \right) \right] \right) \right. \\ &\left. + \frac{F_H B}{420} \left(1 - e^{-6\tau} \left[\cos \left(\frac{Wi}{B} \tau \right) + \frac{6B}{Wi} \sin \left(\frac{Wi}{B} \tau \right) \right] \right) \right\} + O(Wi^3), \end{aligned} \quad (3.63)$$

where the normal stress differences are defined as $N_1 = \tau_{xx} - \tau_{yy}$ and $N_2 = \tau_{yy} - \tau_{zz}$. The leading order result for the second normal stress difference ($N_2 = -N_1/2$) is the classical result for the co-rotational Jeffrey's model, which is valid in the linear viscoelastic limit⁶⁵. Extending the co-rotational memory integral to the MAOS regime allows for a correction to this classical result, which depends on G_{II} .

For the cessation of steady shear flow at time $\tau = \tau^*$, the co-rotational rate of strain tensor is,

$$\check{\mathbf{E}}^-(\tau, \tau') = \frac{\dot{\gamma}_0}{2} \left\{ \sin \left[\frac{\dot{\gamma}_0}{D_r} (\tau^* - \tau') \right] (\mathbf{e}_x \mathbf{e}_x - \mathbf{e}_y \mathbf{e}_y) + \cos \left[\frac{\dot{\gamma}_0}{D_r} (\tau^* - \tau') \right] (\mathbf{e}_x \mathbf{e}_y + \mathbf{e}_y \mathbf{e}_x) \right\}, \quad (3.64)$$

which is valid for $-\infty < \tau' < \tau^*$. The superscript ‘-’ denotes the cessation condition. Substitution of (3.55), (3.58), and (3.64) into (3.1) yields,

$$\frac{\tau_{yx}^-}{2\mu_s c \dot{\gamma}_0} = \frac{2A_H}{15} + \frac{2B_H}{3} + \frac{C_H}{2} + \frac{F_H B}{30} e^{-6(\tau - \tau^*)} + O(Wi^2), \quad (3.65)$$

$$\frac{N_1^-}{\mu_s c \dot{\gamma}_0} = \frac{F_H Wi}{45} e^{-6(\tau - \tau^*)} + O(Wi^3), \quad (3.66)$$

and

$$\frac{N_2^-}{\mu_s c \dot{\gamma}_0} = \frac{-N_1^-}{2\mu_s c \dot{\gamma}_0} + Wi \left(\frac{4A_H}{105} + \frac{B_H}{30} + \frac{F_H B}{420} \right) e^{-6(\tau - \tau^*)} + O(Wi^3). \quad (3.67)$$

The MAOS reconstruction results for the second normal stress difference, given in (3.63) and (3.67), are depicted in Figure 3.3 for $Wi/B = 0.5$ and 3 for a dilute suspension of rods ($B = 1$) and disks ($B = -1$). These results are also compared to a numerical solution of (3.28) and the leading order contribution, neglecting G_{II} ($N_2 = -N_1/2$). Here, we see that G_{II} is required for an accurate prediction of N_2 beyond small $|Wi|$. For both rods and disk, qualitative agreement between the MAOS reconstruction and numerical results is observed. Surprisingly, for rods, we observe near quantitative agreement at $Wi/B = 3$, which is not small compared to unity and thus arguably beyond the ‘weakly nonlinear’ regime.

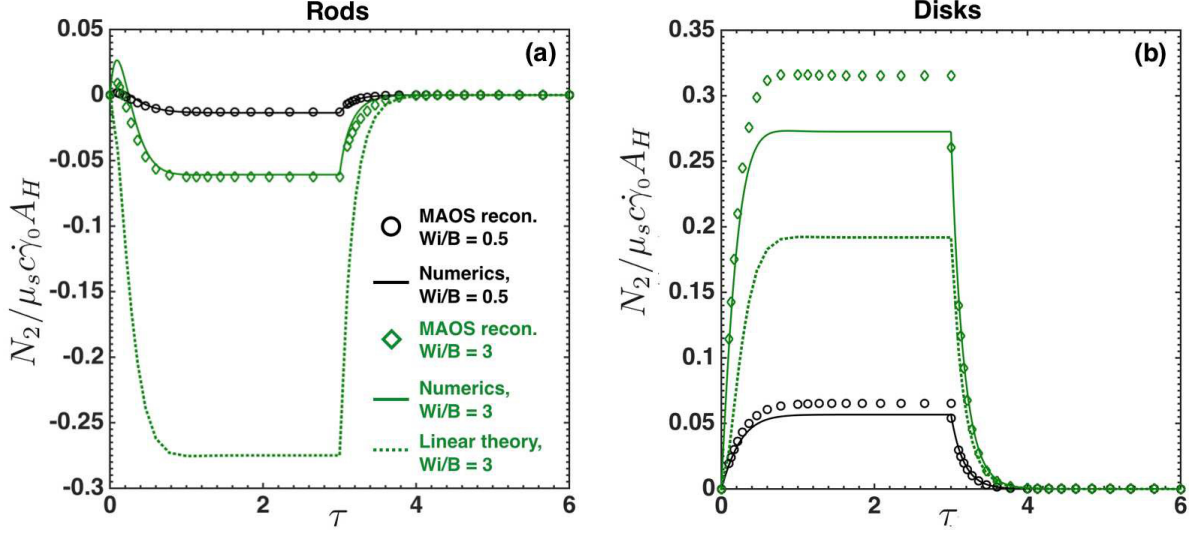


Figure 3.3: Second normal stress difference ($N_2 = \tau_{yy} - \tau_{zz}$) for a dilute suspension of **a):** rigid rods ($B = 1$) and **(b):** rigid disks ($B = -1$) for the start-up and cessation of simple shear flow for $Wi/B = 0.5$ and $Wi/B = 3$. The flow is started at $\tau = 0$ and the stress is allowed to reach a steady value. At $\tau = 3$, the flow is stopped and the stress relaxes back to equilibrium. The solid lines are the numerical solution to the conservation equation and particle stress response, given in (3.28) and (3.41). The symbols are generated from the reconstruction results that utilize the linear and MAOS relaxation moduli, given in (3.61) and (3.65). The dashed line represent the leading order contribution to the second normal stress difference in (3.61) and (3.65) for $Wi/B = 3$, which one would obtain by neglecting the contribution of G_{II} ($N_2(t) = -N_1(t)/2$).

3.4.2 Start-up and Cessation of Uniaxial Extensional Flow

The co-rotational rate-of-strain tensor for the start-up of steady uniaxial extensional flow at time $\tau = 0$ is,

$$\check{\mathbf{E}}(\tau, \tau') = \frac{\dot{\epsilon}}{2\sqrt{3}} (2\mathbf{e}_z\mathbf{e}_z - \mathbf{e}_x\mathbf{e}_x - \mathbf{e}_y\mathbf{e}_y), \quad (3.68)$$

which is valid for $0 < \tau' < \tau$. Note that (3.68) is equivalent to the rate-of-strain tensor in a fixed frame of reference because uniaxial extension is an irrotational flow ($\mathbf{\Omega} = 0$). Substitution of (3.55), (3.58), and (3.68) into (3.1) yields,

$$\begin{aligned} \frac{\mu_e^+}{2\mu_s c} &= \frac{2A_H}{15} + \frac{2B_H}{3} + \frac{C_H}{2} + \frac{F_H B}{30} (1 - e^{-6\tau}) \\ &+ \frac{Wi}{60\sqrt{3}} \left[\left(\frac{8A_H}{7} + 4B_H \right) (1 - e^{-6\tau}) + \frac{F_H B}{14} (1 - e^{-6\tau} - 6\tau e^{-6\tau}) \right] + O(Wi^2), \end{aligned} \quad (3.69)$$

where the extensional viscosity is defined as, $\mu_e = (\tau_{zz} - \tau_{xx})/2\sqrt{3}\dot{\epsilon}$. For the cessation of uniaxial extensional flow at time $\tau = \tau^*$, the co-rotational rate-of-strain tensor is again given by (3.68), which is valid for $-\infty < \tau' < \tau^*$. Substitution of (3.55), (3.58), and (3.68) into (3.1) yields,

$$\frac{\mu_e^-}{2\mu_s c} = \frac{2A_H}{15} + \frac{2B_H}{3} + \frac{C_H}{2} + \left[\frac{F_H B}{30} + \frac{Wi}{60\sqrt{3}} \left(\frac{8A_H}{7} + 4B_H + \frac{F_H B}{14} \right) \right] e^{-6(\tau-\tau^*)} \quad (3.70)$$

$$+ O(Wi^2).$$

The MAOS reconstruction results of (3.69) and (3.70) are depicted in Figure 3.4 for $Wi/B = 0.75$ and 3 for a dilute suspension of rods ($B = 1$) and disks ($B = -1$). These results are also compared to a numerical solution to (3.28) and the leading order contribution, neglecting G_{II} . Here, the leading order contribution to the extensional viscosity is independent of Wi , making the contribution of G_{II} increasingly important as the strength of the flow is increased. A qualitative agreement between the MAOS reconstruction and numerical results is obtained for both rods and disks. Here, we observe near quantitative agreement at $Wi/B = 3$ for both rods and disks, which is, again, beyond the ‘weakly nonlinear’ regime.

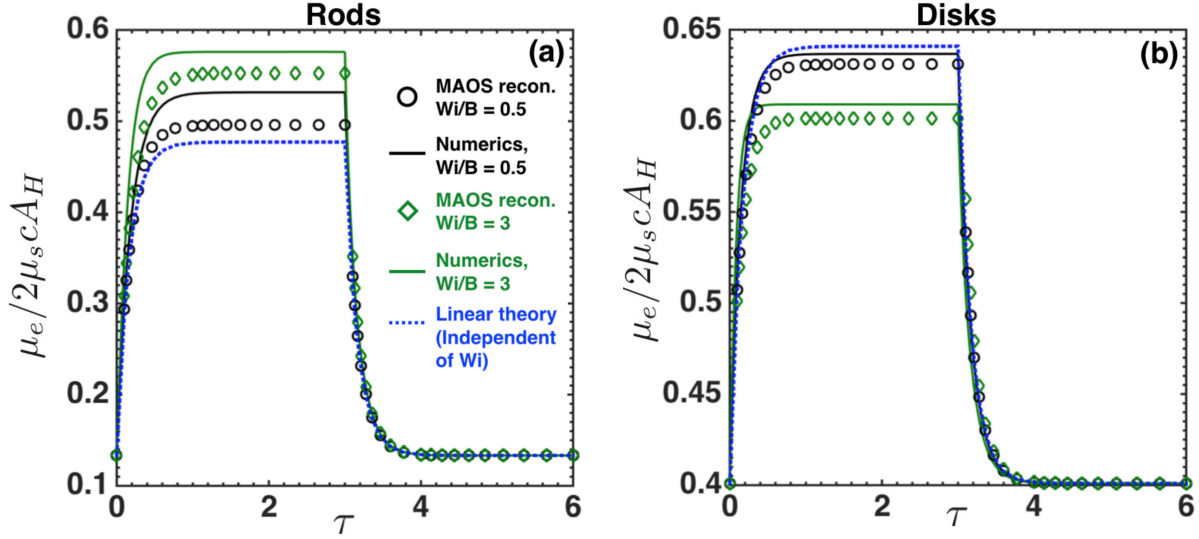


Figure 3.4: Extensional viscosity of a dilute suspension of (a): rigid rods ($B = 1$) and (b): rigid disks ($B = -1$) for the start-up and cessation of uniaxial extension for $Wi/B = 0.75$ and 3 . The flow is started at $\tau = 0$ and the stress is allowed to reach a steady value. At time $\tau = 3$, the flow is stopped and the stress is allowed to relax back to equilibrium. Here, the extensional viscosity at $\tau = 0$ and $\tau = 6$ is not equal to zero, due to an equilibrium contribution to the bulk stress solely arising from the addition of particles. The solid lines are the numerical solution to the conservation equation and particle stress response, given in (3.28) and (3.41). The symbols are generated from the reconstruction results that utilize the linear and MAOS relaxation moduli, given in (3.69) and (3.70). The dashed line represents the leading order contribution to the extensional viscosity in (3.69) and (3.70), which one would obtain by neglecting the contribution of G_{II} .

3.5 Discussion

We have determined the MAOS relaxation modulus for a dilute suspension of Brownian spheroids. This is accomplished by subjecting the material to a dual-frequency MAOS deformation. From the resulting shear stress and second normal stress difference, the linear (G_I) and MAOS relaxation moduli (G_{II}), respectively, can be determined. This allows one to predict the stress response of the system under a transient deformation of arbitrary flow type by use of the co-rotational memory integral expansion. In principal, one could determine higher order moduli in the co-rotational memory integral expansion by use of a multi-frequency oscillatory shear deformation (e.g. tri-frequency for G_{III} and G_{IV} ⁹⁷). However, we have limited our analysis to the weakly nonlinear, dual-frequency, MAOS regime. Following Swan et al.⁹⁷, it is evident that the MAOS regime encodes information on the ‘weakly nonlinear’ memory of a viscoelastic fluid.

The co-rotational memory integral expansion is useful because of its general applicability to simple fluids^{64,81,93}. We have demonstrated this for a dilute suspension of Brownian spheroids, whose microstructure is governed by the Fokker-Planck equation. The eigenfunctions of the Fokker-Planck equation in space and time are decoupled, which allows for one to determine analytical expressions for G_I and G_{II} . A similar procedure can be employed for a dilute colloidal dispersion of mono-disperse hard-spheres, whose microstructure is governed by a two-body Smoluchowski equation^{98,99},

$$\frac{\partial g}{\partial t} + \nabla_r \cdot [\mathbf{u}_r g - (\mathbf{D}_r \cdot \nabla_r)g] = 0, \quad (3.71)$$

where \mathbf{r} is the separation distance between two particles, ∇_r is the relative gradient operator, $\mathbf{u}_r = \mathbf{u}_2 - \mathbf{u}_1$ is the relative velocity of the two particles, and \mathbf{D}_r is the relative diffusivity tensor¹⁰⁰. Here, $g = g(\mathbf{r}, t)$ is the pair distribution function that describes the likelihood of finding a particle at position \mathbf{r} , relative to a second particle. One can solve (3.71) for a single-frequency oscillatory shear flow in the SAOS regime, analogously to what is done here in Section 3.3.2. The leading order contribution to the pair distribution function, $g = 1 + Wi f_1 + O(Wi^2)$, is of the same structural form as (3.34); namely⁹⁸,

$$f_1(r, t) = -\frac{1}{2}f(r)e^{-i\tilde{\omega}t} \mathbf{d} \cdot \mathbf{E} \cdot \mathbf{d}, \quad (3.72)$$

where, $f_1(r, t)$ is analogous to $\psi_1(\mathbf{p}, t)$ herein, $\tilde{\omega}$ is a dimensionless frequency, $r = |\mathbf{r}|$ is the magnitude of particle separation distance, $\mathbf{d} = \mathbf{r}/r$ is a unit vector connecting the particle centers, and \mathbf{E} is the rate of strain tensor. In the limit of no hydrodynamic interactions, $f(r)$ is governed by the ordinary differential equation,

$$\frac{1}{r^2} \frac{d}{dr} \left(r^2 \frac{df}{dr} \right) - 6 \frac{f}{r^2} - i\tilde{\omega} f = 0, \quad (3.73)$$

where (3.73) is a Bessel's equation and can be solved exactly for non-zero $\tilde{\omega}$ (see equation (56) in

Brady⁹⁸). To determine the MAOS relaxation modulus for a dilute colloidal dispersion, one would need to determine the linear and weakly nonlinear contributions to the pair distribution function for a dual-frequency MAOS deformation, which is analogous to determining ψ_1 and ψ_2 in this work; compute the resultant stress response; and compare the stress response to the result of the co-rotational memory integral expansion in Section 3.2. We leave this as an interesting problem for future work.

The framework presented here can also be applied to constitutive equations, such as the Giesekus model for concentrated polymer solutions^{30,37,73}, for the which the polymer stress, $\boldsymbol{\tau}_p$ evolves as,

$$\overset{\nabla}{\boldsymbol{\tau}}_p = 2G \mathbf{E} - \frac{1}{\lambda} \boldsymbol{\tau}_p - \frac{\xi}{\lambda G} \boldsymbol{\tau}_p \cdot \boldsymbol{\tau}_p, \quad (3.74)$$

where,

$$\overset{\nabla}{\boldsymbol{\tau}}_p = \frac{\partial \boldsymbol{\tau}_p}{\partial t} + \mathbf{v} \cdot \nabla \boldsymbol{\tau}_p - (\nabla \mathbf{v})^T \cdot \boldsymbol{\tau}_p - \boldsymbol{\tau}_p \cdot \nabla \mathbf{v}, \quad (3.75)$$

is the upper convective (Maxwell) derivative, λ is the characteristic relaxation time, and G is the elastic modulus. The final term in (3.74) accounts for anisotropic drag arising from the hydrodynamic interaction between polymer chains and is tuned by a “nonlinearity parameter,” ξ , where $\xi = [0, 1]$. One can determine the linear and MAOS relaxation moduli by substituting the definition for the dual-frequency, oscillatory rate-of-strain tensor, given in (3.12), into (3.74), and expanding $\boldsymbol{\tau}_p$ accordingly. In the MAOS regime, the shear stress response will oscillate at the input frequencies (ω_1, ω_2) , to leading order in Wi . The linear relaxation modulus can be determined by a comparison of the shear stress response of the Giesekus model to that of the memory integral expansion given in (3.19). Furthermore, the leading order second normal stress difference from $\boldsymbol{\tau}_p$ will oscillate a frequencies $2\omega_1, 2\omega_2, \omega_1 - \omega_2$, and $\omega_1 + \omega_2$. A comparison of the second normal stress difference to the memory integral expansion in (3.20) and (3.21) will yield the MAOS relaxation modulus for the Giesekus model.

The MAOS relaxation modulus could be determined experimentally, in principle. First, one would need to perform a strain rate sweep to precisely define the weakly nonlinear regime, where

the shear stress and normal stress differences vary linearly and quadratically with the strain rate amplitude, respectively (e.g. $\tau_{yx} \propto Wi$ and $N_1, N_2 \propto Wi^2$). One experimental apparatus that can be used is a cone-and-plate rheometer with a monolithic plate fitted with miniature capacitive pressure sensors¹⁰¹ and a computer program capable of applying a parallel superposition strain to the material, specially a dual-frequency oscillatory deformation. Here, the shear stress is calculated in the standard manner from the measured torque, which can be decomposed to determine the components of the complex viscosity, as given in (3.7). The linear relaxation modulus can then be determined from the discrete complex viscosity by one of three methods: 1) fitting the data to a generalized Maxwell model and performing the 1-D inverse Fourier Cosine Transform (FCT) on the fit¹⁰²; 2) numerically evaluate the inverse FCT equation given in (3.10)¹⁰³; 3) perform a discrete inverse Fourier Transform (DFT)¹⁰⁴. The third method requires that the complex viscosity is known at evenly spaced frequency values. Generally, the frequency values are logarithmically spaced and a suitable interpolation technique must be applied in order to use DFT. In this set-up, the second normal stress difference is determined from the pressure measurement, P , where

$$P = -(N_1 + 2N_2) \ln(r/R) - N_2, \quad (3.76)$$

R is the rheometer plate radius, and r is the radial position of the measurement¹⁰¹. A linear regression analysis can be applied to the discrete pressure measurements as a function of the logarithm of the radial position scaled by the plate radius. From this, $-N_2$ is the intercept, i.e. the pressure measurement extrapolated to the plate edge. Also, N_1 can be determined from the normal force on the plate, which, when combined with the slope of the linear regression analysis, provides an additional measurement of N_2 . N_2 can then be decomposed into its harmonic contributions, as given in (3.20). Again, it is the harmonic contribution at $\cos[(\omega_1 + \omega_2)t]$ that is important for our purposes, which is given in (3.21). The first three terms on the right-hand-side of (3.21) can be determined, from the linear relaxation modulus, and subtracted from F_3 , as given in (3.23). Then, by applying a 2-D inverse FCT to this quantity, one can determine the MAOS relaxation modulus, as shown

in (3.22). Similar to the linear relaxation modulus, G_{II} can be determined by either 1) fitting data and performing a 2-D inverse FCT; 2) numerically evaluating the 2-D symmetric, inverse FCT; or 3) performing a discrete 2-D FCT at evenly spaced frequency values. The second normal stress difference can also be measured using other techniques¹⁰⁵, such as a partitioned cone-and-plate rheometer¹⁰⁶ and pressure distribution parallel-plate rheometer¹⁰⁷. We acknowledge that practical difficulties will undoubtedly arise in an experimental setting, particularly with regard to noise. At low frequencies, the long time dynamics of the material are probed; since the linear and MAOS relaxation moduli decay in time, we do not foresee noise being an issue in this regime. However, at large frequencies, where the short time dynamics of the material are probed, noise could pose a potential issue. However, we hope that our work will prompt experimental consideration.

In summary, if one is able to determine the shear stress and second normal stress difference of a complex fluid subject to a dual-frequency oscillatory shear flow, whether that material is considered experimentally, via a micro-mechanical model, or a constitutive equation, we suggest that the first nonlinear ‘MAOS’ relaxation modulus can be determined by use of the co-rotational memory integral expansion. From the MAOS relaxation modulus, the weakly nonlinear, transient stress response of a material under an arbitrary deformation can be predicted.

3.A Appendix

3.A.1 Coefficients of N_2 from the co-rotational memory integral expansion

Below are the coefficients of N_2 given in (3.20) for a dual-frequency MAOS deformation.

$$\begin{aligned}
 F_0(\omega_1, \omega_2) = & \frac{1}{\omega_2} \int_0^\infty G_I(s) \sin(\omega_1 s) ds + \frac{1}{\omega_1} \int_0^\infty G_I(s) \sin(\omega_2 s) ds \\
 & - \int_0^\infty \int_0^\infty G_{II}(s, q) \cos[\omega_1(s - q)] ds dq + \int_0^\infty \int_0^\infty G_{II}(s, q) \cos[\omega_2(s - q)] ds dq
 \end{aligned} \tag{3.77}$$

$$\begin{aligned}
H_1(\omega_1, \omega_2) &= \frac{1}{\omega_1} \int_0^\infty G_I(s) \cos(\omega_1 s) \mathbf{d}s + \frac{1}{\omega_2} \int_0^\infty G_I(s) \cos(\omega_2 s) \mathbf{d}s \\
&\quad - \int_0^\infty \int_0^\infty G_{II}(s, q) \sin[\omega_1(s+q)] \mathbf{d}s \mathbf{d}q
\end{aligned} \tag{3.78}$$

$$\begin{aligned}
F_1(\omega_1, \omega_2) &= \frac{-1}{\omega_1} \int_0^\infty G_I(s) \sin(\omega_1 s) \mathbf{d}s - \frac{1}{\omega_2} \int_0^\infty G_I(s) \sin(\omega_2 s) \mathbf{d}s \\
&\quad - \int_0^\infty \int_0^\infty G_{II}(s, q) \cos[\omega_1(s+q)] \mathbf{d}s \mathbf{d}q
\end{aligned} \tag{3.79}$$

$$\begin{aligned}
H_2(\omega_1, \omega_2) &= \frac{1}{\omega_1} \int_0^\infty G_I(s) \cos(\omega_1 s) \mathbf{d}s + \frac{1}{\omega_2} \int_0^\infty G_I(s) \cos(\omega_2 s) \mathbf{d}s \\
&\quad - \int_0^\infty \int_0^\infty G_{II}(s, q) \sin[\omega_2(s+q)] \mathbf{d}s \mathbf{d}q
\end{aligned} \tag{3.80}$$

$$\begin{aligned}
F_2(\omega_1, \omega_2) &= \frac{1}{\omega_1} \int_0^\infty G_I(s) \sin(\omega_1 s) \mathbf{d}s + \frac{1}{\omega_2} \int_0^\infty G_I(s) \sin(\omega_2 s) \mathbf{d}s \\
&\quad - \int_0^\infty \int_0^\infty G_{II}(s, q) \cos[\omega_2(s+q)] \mathbf{d}s \mathbf{d}q
\end{aligned} \tag{3.81}$$

$$\begin{aligned}
H_3(\omega_1, \omega_2) &= \frac{1}{\omega_1} \int_0^\infty G_I(s) \cos(\omega_2 s) \mathbf{d}s + \frac{1}{\omega_2} \int_0^\infty G_I(s) \cos(\omega_1 s) \mathbf{d}s + \\
&\quad \left(\frac{1}{\omega_1} + \frac{1}{\omega_2} \right) \int_0^\infty G_I(s) \cos[(\omega_1 + \omega_2)s] \mathbf{d}s - \\
&\quad \int_0^\infty \int_0^\infty G_{II}(s, q) \left[\sin(\omega_1 s + \omega_2 q) + \sin(\omega_1 q + \omega_2 s) \right] \mathbf{d}s \mathbf{d}q
\end{aligned} \tag{3.82}$$

$$\begin{aligned}
F_3(\omega_1, \omega_2) &= \frac{-1}{\omega_1} \int_0^\infty G_I(s) \sin(\omega_2 s) \mathbf{d}s - \frac{1}{\omega_2} \int_0^\infty G_I(s) \sin(\omega_1 s) \mathbf{d}s \\
&\quad + \left(\frac{1}{\omega_1} + \frac{1}{\omega_2} \right) \int_0^\infty G_I(s) \sin[(\omega_1 + \omega_2)s] \mathbf{d}s \\
&\quad - \int_0^\infty \int_0^\infty G_{II}(s, q) \left[\cos(\omega_1 s + \omega_2 q) + \cos(\omega_1 q + \omega_2 s) \right] \mathbf{d}s \mathbf{d}q
\end{aligned} \tag{3.83}$$

$$\begin{aligned}
H_4(\omega_1, \omega_2) &= \frac{1}{\omega_1} \int_0^\infty G_I(s) \cos(\omega_2 s) \mathbf{d}s - \frac{1}{\omega_2} \int_0^\infty G_I(s) \cos(\omega_1 s) \mathbf{d}s \\
&+ \left(\frac{1}{\omega_1} - \frac{1}{\omega_2} \right) \int_0^\infty G_I(s) \cos[(\omega_1 - \omega_2)s] \mathbf{d}s - \\
&- \int_0^\infty \int_0^\infty G_{II}(s, q) \left[\sin(\omega_1 s - \omega_2 q) + \sin(\omega_2 s - \omega_1 q) \right] \mathbf{d}s \mathbf{d}q
\end{aligned} \tag{3.84}$$

$$\begin{aligned}
F_4(\omega_1, \omega_2) &= \frac{1}{\omega_1} \int_0^\infty G_I(s) \sin(\omega_2 s) \mathbf{d}s + \frac{1}{\omega_2} \int_0^\infty G_I(s) \sin(\omega_1 s) \mathbf{d}s \\
&+ \left(\frac{1}{\omega_1} - \frac{1}{\omega_2} \right) \int_0^\infty G_I(s) \sin[(\omega_1 - \omega_2)s] \mathbf{d}s \\
&- \int_0^\infty \int_0^\infty G_{II}(s, q) \left[\cos(\omega_1 s - \omega_2 q) + \cos(\omega_2 s - \omega_1 q) \right] \mathbf{d}s \mathbf{d}q
\end{aligned} \tag{3.85}$$

3.A.2 Frequency-dependent coefficients of ψ_2

Below are the frequency-dependent coefficients, $f_{2,0}$, $f_{2,\alpha}$, $f_{2,\beta}$, $f_{2,s}$, and $f_{2,d}$ of ψ_2 given in (3.38).

First,

$$f_{2,0} = T_0(\mathbf{S} : \mathbf{S}) + U_0(\mathbf{p} \cdot \mathbf{S} \cdot \mathbf{S} \cdot \mathbf{p}) + V_0(\mathbf{p} \cdot \mathbf{S} \cdot \mathbf{A} \cdot \mathbf{p}) + W_0(\mathbf{pp} : \mathbf{S})^2, \tag{3.86}$$

where,

$$T_0 = \frac{-3}{10} \left(\frac{1}{\alpha^2 + 36} + \frac{1}{\beta^2 + 36} \right), \tag{3.87a}$$

$$U_0 = 0, \tag{3.87b}$$

$$V_0 = -3 \left(\frac{1}{\alpha^2 + 36} + \frac{1}{\beta^2 + 36} \right), \tag{3.87c}$$

$$W_0 = \frac{9}{4} \left(\frac{1}{\alpha^2 + 36} + \frac{1}{\beta^2 + 36} \right). \tag{3.87d}$$

Second,

$$f_{2,\alpha} = T_\alpha(\mathbf{S} : \mathbf{S}) + U_\alpha(\mathbf{p} \cdot \mathbf{S} \cdot \mathbf{S} \cdot \mathbf{p}) + V_\alpha(\mathbf{p} \cdot \mathbf{S} \cdot \mathbf{A} \cdot \mathbf{p}) + W_\alpha(\mathbf{pp} : \mathbf{S})^2, \tag{3.88}$$

where,

$$T_\alpha = \frac{-3i}{4[\alpha^3 - 108\alpha + i(180 - 19\alpha^2)]}, \quad (3.89a)$$

$$U_\alpha = \frac{3\alpha}{4[\alpha^3 - 108\alpha + i(180 - 19\alpha^2)]}, \quad (3.89b)$$

$$V_\alpha = \frac{3}{4(\alpha^2 - 18 - 9i\alpha)}, \quad (3.89c)$$

$$W_\alpha = \frac{-15}{8(\alpha^2 - 60 - 16i\alpha)}. \quad (3.89d)$$

Third,

$$f_{2,\beta} = T_\beta(\mathbf{S} : \mathbf{S}) + U_\beta(\mathbf{p} \cdot \mathbf{S} \cdot \mathbf{S} \cdot \mathbf{p}) + V_\beta(\mathbf{p} \cdot \mathbf{S} \cdot \mathbf{A} \cdot \mathbf{p}) + W_\beta(\mathbf{pp} : \mathbf{S})^2, \quad (3.90)$$

where,

$$T_\beta = \frac{-3i}{4[\beta^3 - 108\beta + i(180 - 19\beta^2)]}, \quad (3.91a)$$

$$U_\beta = \frac{3\alpha}{4[\beta^3 - 108\beta + i(180 - 19\beta^2)]}, \quad (3.91b)$$

$$V_\beta = \frac{3}{4(\beta^2 - 18 - 9i\beta)}, \quad (3.91c)$$

$$W_\beta = \frac{-15}{8(\beta^2 - 60 - 16i\beta)}. \quad (3.91d)$$

Fourth,

$$f_{2,s} = T_s(\mathbf{S} : \mathbf{S}) + U_s(\mathbf{p} \cdot \mathbf{S} \cdot \mathbf{S} \cdot \mathbf{p}) + V_s(\mathbf{p} \cdot \mathbf{S} \cdot \mathbf{A} \cdot \mathbf{p}) + W_s(\mathbf{pp} : \mathbf{S})^2, \quad (3.92)$$

where,

$$T_s = \frac{-3i(\alpha + \beta - 12i)}{(\alpha - 6i)(\beta - 6i)(\alpha + \beta - 6i)(\alpha + \beta - 20i)}, \quad (3.93a)$$

$$U_s = \frac{3[\alpha^2 + 2\alpha(\beta - 6i) + \beta(\beta - 12i)]}{(\alpha - 6i)(\beta - 6i)(\alpha + \beta - 6i)(\alpha + \beta - 20i)}, \quad (3.93b)$$

$$V_s = \frac{3(\alpha + \beta - 12i)}{2(\alpha - 6i)(\beta - 6i)(\alpha + \beta - 6i)}, \quad (3.93c)$$

$$W_s = \frac{-15(\alpha + \beta - 12i)}{4(\alpha - 6i)(\beta - 6i)(\alpha + \beta - 20i)}. \quad (3.93d)$$

Finally,

$$f_{2,d} = T_\beta(\mathbf{S} : \mathbf{S}) + U_d(\mathbf{p} \cdot \mathbf{S} \cdot \mathbf{S} \cdot \mathbf{p}) + V_d(\mathbf{p} \cdot \mathbf{S} \cdot \mathbf{A} \cdot \mathbf{p}) + W_d(\mathbf{pp} : \mathbf{S})^2, \quad (3.94)$$

where,

$$T_d = \frac{3i(\alpha - \beta - 12i)}{(\alpha - 6i)(\beta + 6i)(\alpha - \beta - 6i)(\alpha - \beta - 20i)}, \quad (3.95a)$$

$$U_d = \frac{-3[\alpha^2 - 2\alpha(\beta + 6i) + \beta(\beta + 12i)]}{2(\alpha - 6i)(\beta + 6i)(\alpha - \beta - 6i)(\alpha - \beta - 20i)}, \quad (3.95b)$$

$$V_d = \frac{-3(\alpha - \beta - 12i)}{2(\alpha - 6i)(\beta + 6i)(\alpha - \beta - 6i)}, \quad (3.95c)$$

$$W_d = \frac{15(\alpha - \beta - 12i)}{4(\alpha - 6i)(\beta + 6i)(\alpha - \beta - 20i)}. \quad (3.95d)$$

3.A.3 Two-dimensional inverse Fourier cosine transform to determine G_{II}

The two-dimensional Fourier Cosine Transform (FCT) of an even function $Z(\omega_1, \omega_2) = Z(-\omega_1, -\omega_2)$ and $Z(-\omega_1, \omega_2) = Z(\omega_1, -\omega_2)$, is defined as¹⁰⁸,

$$Z(\omega_1, \omega_2) = \int_0^\infty \int_0^\infty z(t_1, t_2) \cos(\omega_1 t_1 + \omega_2 t_2) dt_1 dt_2, \quad (3.96)$$

with inverse,

$$z(t_1, t_2) = \frac{4}{\pi^2} \int_0^\infty \int_0^\infty Z(\omega_1, \omega_2) \cos(\omega_1 t_1 + \omega_2 t_2) d\omega_1 d\omega_2. \quad (3.97)$$

Here, (3.97) is transforming a frequency-dependent function, Z , to a time-dependent function, z , by mapping all information from ω_1 to only t_1 and ω_2 to only t_2 .

We can rewrite (3.57) as,

$$\kappa(\alpha, \beta) = \int_0^\infty \int_0^\infty G_{II}(\tilde{s}, \tilde{q}) \left[\cos(\alpha\tilde{s} + \beta\tilde{q}) + \cos(\beta\tilde{s} + \alpha\tilde{q}) \right] d\tilde{s}d\tilde{q}, \quad (3.98)$$

where,

$$\kappa = \frac{3\mu_s c B D_r}{5} \left\{ \left(\frac{16A_H}{7} + 8B_H \right) \frac{\alpha^2 + \beta^2 + 72}{(\alpha^2 + 36)(\beta^2 + 36)} + \frac{F_H B}{7} \left[\frac{2592 - \alpha\beta [(\alpha + \beta)^2 + 72]}{(\alpha^2 + 36)(\beta^2 + 36) [(\alpha + \beta)^2 + 36]} \right] \right\} \quad (3.99)$$

Recall that the oscillation frequencies, α and β , are interchangeable because we have required that the imposed deformation be described by a single strain-rate amplitude, $\dot{\gamma}_0 = \gamma_1 \alpha D_r = \gamma_2 \beta D_r$. Therefore, $\kappa(\alpha, \beta) = \kappa(\beta, \alpha)$. The form of the right-hand-side of (3.57) and (3.98) also arises due to fact that α and β are interchangeable and cannot solely map to each time-domain variable (i.e. \tilde{s} and \tilde{q} are mapped by both α and β). G_{II} can be resolved from (3.98) by applying the inverse Fourier Cosine Transform, given in (3.97), for interchangeable frequency values,

$$G_{II}(\tilde{s}, \tilde{q}) = \int_0^\infty \int_0^\infty \kappa(\alpha, \beta) \left[\cos(\alpha\tilde{s} + \beta\tilde{q}) + \cos(\beta\tilde{s} + \alpha\tilde{q}) \right] d\alpha d\beta, \quad (3.100)$$

Evaluating the integrals in (3.100) for the first term of (3.99) yields,

$$\frac{4}{\pi^2} \int_0^\infty \int_0^\infty \frac{\alpha^2 + \beta^2 + 72}{(\alpha^2 + 36)(\beta^2 + 36)} \left[\cos(\alpha\tilde{s} + \beta\tilde{q}) + \cos(\beta\tilde{s} + \alpha\tilde{q}) \right] d\alpha d\beta = \frac{1}{3} \delta(\tilde{s}) e^{-6\tilde{q}}. \quad (3.101)$$

The quantity in square brackets in (3.99) can be expanded as,

$$\begin{aligned} \frac{2592 - \alpha\beta [(\alpha + \beta)^2 + 72]}{(\alpha^2 + 36)(\beta^2 + 36)[(\alpha + \beta)^2 + 36]} = & \quad (3.102) \\ \frac{36 - \alpha(\alpha + \beta)}{(\alpha^2 + 36)[(\alpha + \beta)^2 + 36]} + \frac{36 - \beta(\alpha + \beta)}{(\beta^2 + 36)[(\alpha + \beta)^2 + 36]}, \end{aligned}$$

where,

$$\begin{aligned} & \frac{36 - \beta(\alpha + \beta)}{(\beta^2 + 36)[(\alpha + \beta)^2 + 36]} \left[\cos(\alpha\tilde{s} + \beta\tilde{q}) + \cos(\beta\tilde{s} + \alpha\tilde{q}) \right] \quad (3.103) \\ = & \frac{36 - \alpha(\alpha + \beta)}{(\alpha^2 + 36)[(\alpha + \beta)^2 + 36]} \left[\cos(\beta\tilde{s} + \alpha\tilde{q}) + \cos(\alpha\tilde{s} + \beta\tilde{q}) \right], \end{aligned}$$

for $\alpha = \beta$. Therefore, applying the symmetric two-dimensional inverse FCT to (3.102) yields,

$$\begin{aligned} \frac{4}{\pi^2} \int_0^\infty \int_0^\infty \frac{2592 - \alpha\beta [(\alpha + \beta)^2 + 72]}{(\alpha^2 + 36)(\beta^2 + 36)[(\alpha + \beta)^2 + 36]} \left[\cos(\beta\tilde{s} + \alpha\tilde{q}) + \cos(\alpha\tilde{s} + \beta\tilde{q}) \right] d\alpha d\beta \\ = \frac{8}{\pi^2} \int_0^\infty \int_0^\infty \frac{36 - \beta(\alpha + \beta)}{(\beta^2 + 36)[(\alpha + \beta)^2 + 36]} \left[\cos(\alpha\tilde{s} + \beta\tilde{q}) + \cos(\beta\tilde{s} + \alpha\tilde{q}) \right] d\alpha d\beta. \quad (3.104) \end{aligned}$$

Evaluating the right-hand-side of (3.104) yields,

$$\frac{8}{\pi^2} \int_0^\infty \int_0^\infty \frac{36 - \beta(\alpha + \beta)}{(\beta^2 + 36)[(\alpha + \beta)^2 + 36]} \left[\cos(\alpha\tilde{s} + \beta\tilde{q}) + \cos(\beta\tilde{s} + \alpha\tilde{q}) \right] d\alpha d\beta = e^{-6\tilde{q}}, \quad (3.105)$$

for $q - s > 0$ and $s > 0$. Substitution of (3.101) and (3.105) into (3.100) yields (3.58).

4. Nonlinear Viscoelasticity of a Dilute Suspension of Brownian Spheroids in Oscillatory Shear

4.1 Introduction

Complex fluids are viscoelastic materials that simultaneously exhibit viscous (liquid-like) and elastic (solid-like) characteristics under mechanical strain. For instance, Silly-Putty™ will behave viscously and spread, or flow, when allowed to rest. Silly-Putty™ will also behave elastically and bounce when dropped onto a solid surface, much like a rubber ball would. These different responses of the material are due to its microstructure, which in this case refers to the arrangement of the polymer chains in space and time. When the material is probed over sufficiently small time scales, seconds in this case, the polymer chains are not given sufficient time to relax and effectively become rigid, allowing for the material to bounce like a solid. Conversely, when the material is probed over much longer time scales, say tens of minutes, the polymer chains are given sufficient time to relax and reorient to minimize the stress in the material. This results in a viscous-like material which will spread outward on a solid surface. The viscoelasticity of a material is commonly characterized using a small amplitude oscillatory shear (SAOS) deformation¹⁷. Here the material is subjected to a sinusoidal strain, $\gamma = \gamma_0 \sin(\omega^* t^*)$, where γ_0 is the strain amplitude, ω^* is the oscillation frequency, and t^* is time; the asterisk superscript indicates a dimensional quantity. An experimental advantage of oscillatory rheometry is that one can average the response over numerous periods and avoid step changes that would occur in the start-up and cessation of a flow. There are two relevant time-scales for this deformation: the oscillation time scale, $2\pi/\omega^*$, and flow time-scale, $1/\dot{\gamma}_0^*$, where $\dot{\gamma}_0^* = \gamma_0 \omega^*$ is the strain-rate amplitude. Two dimensionless groups can be obtained from these time scales: a Weissenberg number, $Wi = \dot{\gamma}_0^* \lambda^*$, or dimensionless

strain-rate amplitude, and a Deborah number, $De = \omega^* \lambda^*$, or dimensionless oscillation frequency; here, λ^* is a characteristic relaxation time of the material. Under a small-amplitude deformation, the rate of deformation is small relative to the relaxation rate, $Wi \ll 1$, the material remains in a near-equilibrium state, and the linear viscoelasticity of the material is determined in terms of the frequency-dependent elastic (storage) and viscous (loss) moduli, G' and G'' , respectively. In this regime, the material is probed over a range of De and the resultant shear stress response is linearly proportional to the strain amplitude with a component in-phase and out-of-phase with the oscillatory deformation. The linear relaxation modulus of the material can be determined from an inverse Fourier transform of the elastic or viscous modulus^{17,30}. Knowledge of the linear relaxation modulus enables ones to determine the linear viscoelastic response of the material under an arbitrary small-amplitude deformation history (e.g. start-up or cessation of simple shear)³⁰.

Complex fluids are, however, commonly processed or utilized at conditions far from equilibrium, such as in plastics or polymer melt processing¹⁶, chewing food²⁹, and impact-resistant suits and armor^{27,28}. In these examples, Wi is typically not small and the resultant stress response is no longer a linear function of the strain amplitude. The results of a SAOS deformation cannot be utilized to predict the nonlinear stress response of a material, and thus additional techniques are required. In general, the nonlinear response of a material is probed when both the rate of deformation is not small, $Wi \gtrsim O(1)$, and the extent of deformation is not small, $\gamma_0 = Wi/De \gtrsim O(1)$. Equivalently, when $Wi \sim O(1)$ or larger and $De \sim O(1)$, the relaxation time of the material is comparable to the time-scale of the flow ($\lambda \sim 1/\omega$), and thus the nonlinear and unsteady viscoelasticity of the material is probed. Again, this regime is of practical importance, but relatively little, in comparison to linear viscoelasticity, is known on how to systematically interpret and predict the stress response of a material¹⁰⁹.

Large amplitude oscillatory shear (LAOS) has become a popular rheological technique for probing the nonlinear viscoelasticity of a material. LAOS has been applied to a variety of different systems such as colloidal dispersions^{34–36}, polymer solutions or melts^{16,32,33}, and worm-like micelles^{37–40}, among many others. An advantage of LAOS is that it is sensitive to the molecular

architecture of a material, which other techniques may be unable to discern. For instance, LAOS is capable of distinguishing between a suspension of linear polystyrene and star-branched polystyrene due to differences in the extent of branching and reptation; these differences in the microstructure of the two materials are unpronounced in the SAOS and nonlinear steady shear response⁴¹. LAOS has also been combined with other techniques to provide a comprehensive picture of how the microstructure of a material evolves under a strong, transient deformation. Some examples include the combination of LAOS with: small-angle X-ray scattering (SAXS) to study the orientation and reorientation of lamellar block-copolymers^{76,77}; particle image velocimetry (PIV) for observing spatially heterogeneous microstructures that occur in shear banding³⁸ and the gelation of waxy crude oils¹¹⁰; small-angle neutron scattering (SANS) for studying the impact of nanoparticles on micellar packing¹¹¹, concentration dependent particle alignment¹¹², or shear banding of worm-like micelles^{40,113}; flow-induced birefringence (or rheo-optics) of the dynamic drop deformation of polydimethylsiloxane (PDMS) in a polyisobutylene (PIB) matrix¹¹⁴; and Raman spectroscopy for studying the conformational changes during polymer crystallization or gelation¹¹⁵.

Under a LAOS deformation, the material is still subjected to an oscillating shear flow at a single frequency, ω^* , but the strength of the deformation is large, $Wi > 1$, and the extent of deformation is not small, $Wi/De \gtrsim 1$. The resulting periodic stress response will oscillate at multiple frequencies, a hallmark of a nonlinear response to an oscillatory forcing; typically the shear stress will oscillate at odd overtones (ω^* , $3\omega^*$, $5\omega^*$, etc.) and the normal stress will oscillate at even overtones ($0\omega^*$, $2\omega^*$, $4\omega^*$, etc.). However, it is not guaranteed that the response will be periodic in time or spatially homogeneous. For example, the existence of even harmonics in the shear stress has been predicted in polymer blends¹¹⁶ and observed in colloidal dispersions³⁵ and worm-like micelles³⁸. Quasi-periodic and chaotic stress dynamics have been observed in polymer melts^{117,118} and predicted in the Geisikus model and Johnson-Segalman model¹¹⁶. Graham¹¹⁹ showed that quasi-periodic stress dynamics can also arise due to the coupling of the viscoelasticity of a material and dynamic wall-slip at zero Reynolds number. Various methods have been proposed to decompose a LAOS stress waveform, such as Fourier-Transform Rheology¹²⁰, expansion

with Chebyshev polynomials as a basis set¹²¹, a geometric decomposition into elastic and viscous contributions¹²², and as a sequence of physical processes¹²³.

Theoretical work has included utilizing LAOS to determine nonlinear model parameters in constitutive equations such as the Giesekus model³⁷, the Doi-Edwards model⁷⁴, the Phan-Thien/Tanner (PTT) model⁷⁵, the co-rotational Maxwell model^{124,125}, and co-rotational ANSR model¹²⁶. In these works, the LAOS dynamics are computed via a regular perturbation expansion about either small Wi or small $\gamma_0 = Wi/De$. This approach leads to predictions of the stress response that are asymptotic as either $Wi \rightarrow 0$ or $Wi/De \rightarrow 0$, and neither condition can describe the material dynamics in the truly nonlinear, viscoelastic regime of $Wi \gg 1$ and $Wi/De > 1$. Recent work by Khair⁷³ utilized singular perturbation theory to determine an asymptotic solution to the Giesekus constitutive model at $Wi \gg 1$ and $Wi/De \gg 1$. An alternative approach is to employ a micro-mechanical model to connect the micro-scale dynamics of a material to its macroscopic stress response under LAOS. This approach has been utilized, for example, in cases of semi-dilute, hard-sphere colloidal dispersions⁸⁴, dilute dispersions of Brownian rods^{7,8}, and a dilute dispersion of surfactant-laden drops¹²⁷. In the aforementioned works, the LAOS dynamics were determined either by numerical integration or a regular perturbation expansion about small Wi . Again, the later approach cannot describe a material that is strongly shifted out of equilibrium. Recent work by Leahy et al.^{128,129} on a dilute suspension of rod-like, Brownian particles and by Khair¹³⁰ on a dilute suspension of nearly-spherical, Brownian particles employed a singular perturbation theory to analyze the LAOS dynamics at $Wi \rightarrow \infty$ and $Wi/De \gg 1$.

In this work, we quantify the nonlinear viscoelasticity of a dilute suspension of Brownian spheroids subject to a LAOS deformation. For this model micro-mechanical system, we numerically calculate the entire stress tensor – shear stress and normal stress differences, N_1 and N_2 – along with birefringence parameters - linear dichroism and average orientation angle. This allows us to directly connect changes in the mechanical and optical response of the suspension to rearrangements in the microstructure. Here, the microstructure refers to the orientation dynamics of the particles in the oscillatory shear flow. Previous work has investigated the LAOS response of

dilute rigid-dumbbell suspensions, which consist of particles of infinite aspect ratio, that are either active (self-propelled)⁵⁷ or passive^{7,8}. These works investigated the weakly nonlinear stress response of the material by employing a regular perturbation scheme about either small γ_0 or Wi . Again, this approach limits the applicability of the results to the asymptotic limit of either $\gamma_0 \rightarrow 0$ or $Wi \rightarrow 0$, which cannot be utilized to infer the strongly nonlinear and unsteady response. Swan et al.⁷² theoretically investigated the microrheology of a dilute colloidal suspension deformed by an oscillating probe at arbitrary force amplitude (or Péclet number, Pe) and frequency (De). They were able to probe essentially the entire $Pe-De$ space, akin to the $Wi-De$ space considered here, including the nonlinear, unsteady mechanical response of the material. However, their approach is unable to predict the full stress tensor of the material, due to the axisymmetric microstructure deformation produced by the motion of the spherical probe. Interestingly, Swan et al.⁷² determined a “hypo-viscous” regime where the rate of viscous dissipation is less than that of the undeformed state; this regime occurs when $Pe \gg 1$, $De \gg 1$, and $Pe/De \gg 1$. In this nonlinear, viscoelastic regime, the probe particle moves so strongly and quickly that the wake behind it, voided of bath particles, does not have time to relax and refill with bath particles before the probe particle passes through the region again.

Here we will probe essentially the entire $Wi-De$ parameter space while also determining the full stress tensor along with other experimentally measurable properties of the material, such as birefringence parameters. The stress response of a typical viscoelastic material in the $Wi-De$ parameter space is schematically depicted in Figure 4.1; a yield stress fluid, for example, is not accurately depicted by Figure 4.1 as it requires a finite stress in order to flow. There are four regimes addressed in this work: 1) the linear viscoelastic regime ($Wi \ll 1$); 2) the quasi-linear viscoelastic regime ($Wi > 1$ and $De \gg 1$); 3) the quasi-steady viscoelastic regime ($Wi > 1$ and $De \ll 1$); and 4) the nonlinear viscoelastic regime ($Wi > 1$ and $Wi/De > 1$). In the quasi-linear viscoelastic regime, the oscillation time scale ($1/\omega^*$) is much less than both the relaxation time-scale of the material and the flow time-scale. Here, the material is not given ample time to deform, even if the flow is strong, resulting in a nearly linear material response. We characterize

this regime as quasi-linear because the shear stress response does contain higher order harmonics, which cannot occur in the linear viscoelastic regime. In the quasi-steady viscoelastic regime the oscillation time scale is much greater than the relaxation time scale. Here, the microstructure is given ample time to relax and each oscillation cycle resembles a step-strain deformation. Finally, in the nonlinear viscoelastic regime, the transient, nonlinear response of the material is probed. When $Wi > 1$ and $De \sim O(1)$, the material is unable to fully relax over an oscillation cycle and overshoots are observed in the shear stress and normal stress differences, which result from significant microstructural changes.

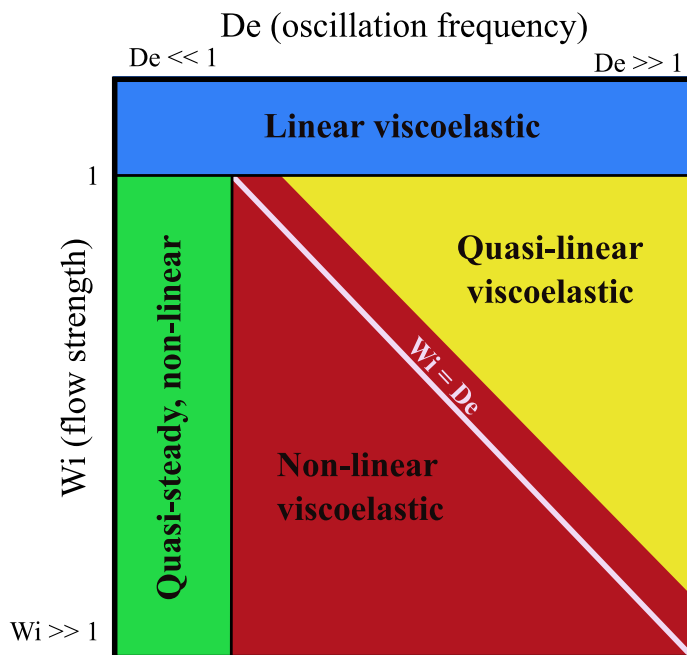


Figure 4.1: Schematic of the stress response of a material in the $Wi - De$ parameter space. When $Wi \ll 1$, the linear viscoelastic response of the material is probed. Under strong deformation ($Wi \gg 1$), but small oscillation frequency ($De \ll 1$) the quasi-steady nonlinear response is interrogated, similar to a step-strain deformation. In the limit of large oscillation frequency ($De \gg 1$) the material is not given sufficient time to deform and a quasi-linear material response can be obtained, even if the strength of the deformation is large ($Wi \gg 1$). In general, when $Wi \gg 1$ and $Wi/De \gtrsim 1$, the nonlinear viscoelasticity of the material is probed.

This article is organized as follows. In Section 4.2 the micro-mechanical model of a dilute suspension of Brownian spheroids is presented. In Section 4.3 we employ a Fourier series in time and a finite difference discretization in space to numerically calculate the microstructure, parameterized by the non-equilibrium orientation distribution function. In Section 4.4 the results

of our numerical approach, namely the non-equilibrium orientation distribution function, stress, and birefringence parameters, are given for prolate rods of aspect ratio $r = 20$ over a range of Wi and De . Finally, in Section 4.5 we discuss the microstructural origins of multiple stress overshoots in the nonlinear viscoelastic regime, provide additional results for oblate particles, and discuss the overall conclusions of this work.

4.2 Micro-mechanical Model

4.2.1 Problem setup

The micro-mechanical model utilized is a homogeneous, monodisperse, dilute suspension of force and couple-free, Brownian spheroids. The suspending medium is a Newtonian fluid with viscosity μ_s and density ρ_s . This well studied model has the advantage that the macroscopic suspension rheology can be directly calculated from the micro-dynamics of the particles. The spheroidal particles are characterized by a major (rotation) axis, ℓ , and two equivalent minor axes, a . The ratio of the major axis, to minor axes is the aspect ratio, $r = \ell/a$. The particles are sufficiently small such that inertia can be neglected. The Bretherton constant, a measure of the hydrodynamic sphericity of the particles, is defined as

$$B = \frac{r^2 - 1}{r^2 + 1}, \quad (4.1)$$

which is zero for spheres, between zero and unity for prolate spheroids, and between zero and negative unity for oblate spheroids¹². The suspension is assumed dilute, such that all interparticle interactions are negligible. For nearly spherical particles ($\ell \approx a$), this simply requires that the volume fraction of particles is much less than unity, $nV_p \ll 1$, where n is the number density of particles and $V_p = 4\pi\ell a^2/3$ is the volume of a single particle. However, an elongated particle ($\ell \gg a$) generates a disturbance to the ambient flow over a length scale ℓ^3 ; hence, the neglect of hydrodynamic interactions requires a more stringent condition, $nV_p r^2 \ll 1$. Similarly, a thin, oblate particle ($\ell \ll a$) generates a disturbance to the ambient flow over a length scale a^3 , requiring

that $nV_p/r^2 \ll 1$ for hydrodynamic interactions to be neglected.

Initially, the microstructure is assumed to be isotropic with no preferential particle orientation. The suspension is then subjected to a spatially homogenous, transient, and linear flow with velocity $\mathbf{v}^*(t^*)$ and velocity gradient $\mathbf{\Gamma}^*(t^*)$, where t^* is time. The orientation unit vector, \mathbf{p} , is defined along the axis of rotation of a particle. In the absence of Brownian motion, \mathbf{p} will rotate deterministically based on Jeffery's equation⁹,

$$\dot{\mathbf{p}}_J = \mathbf{p} \cdot \mathbf{\Omega}^* + B (\mathbf{E}^* \cdot \mathbf{p} - \mathbf{E}^* : \mathbf{p}\mathbf{p}\mathbf{p}), \quad (4.2)$$

where $\mathbf{\Omega}^* = (\mathbf{\Gamma}^* - \mathbf{\Gamma}^{*T})/2$ and $\mathbf{E}^* = (\mathbf{\Gamma}^* + \mathbf{\Gamma}^{*T})/2$ are the vorticity and rate-of-strain tensors, respectively; the superscript T represents the matrix transpose. Equation (4.2) can be solved exactly for steady, simple shear^{9,12} and the orientation will evolve periodically in time for $|B| < 1$. The resultant trajectory, with period $T_{JO} = 2\pi(r + r^{-1})/\dot{\gamma}_0$, is known as a Jeffery orbit and is given by⁹,

$$\tan \theta = \frac{C r}{\sqrt{r^2 \cos^2 \phi + \sin^2 \phi}}, \quad (4.3)$$

and

$$\tan \phi = -r \tan \left(\frac{\dot{\gamma}_0 t}{r + r^{-1}} + \kappa \right), \quad (4.4)$$

where θ is the polar angle from the vorticity direction, ϕ is the azimuthal angle from the flow axis (see Figure 4.2), $C = [0, \infty)$ is the orbit constant, which sets the specific orbit a particle will follow, and κ is the phase along an orbit; since all orbits have the same period, a single phase angle is sufficient. If $|B| \geq 1$, a particle adopts a terminal orientation in steady shear flow^{131,132}. For nearly-spherical particles, the velocity along an orbit will be roughly constant, a particle will essentially rotate at half of the ambient vorticity and the orbits trace lines of latitude along a unit sphere. For elongated particles ($B \nearrow 1$), the particle trajectory traces greater circles and the velocity is highly non-uniform along an orbit, with particles spending most of their time nearly aligned with the flow. Notably, this configuration causes the least disturbance to the ambient flow and thus suspension stress. The Jeffery orbits for a nearly-spherical particle ($r = 1.1$) and an

elongated particle ($r = 20$) are shown in Figure 4.3.

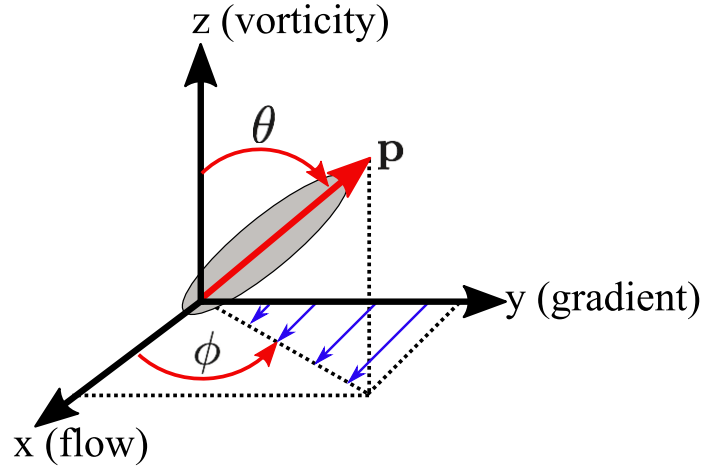


Figure 4.2: Definition of spherical coordinates. The polar angle, θ , denotes the projection of the orientation unit vector, \mathbf{p} , into the x-y plane (flow-gradient plane). The azimuthal angle, ϕ , denotes the orientation in the x-y plane with respect to the positive flow axis.

Equation (4.2), for $|B| < 1$, describes the periodic orientational motion of a particle, and thus periodic suspension stress, with no mechanism of relaxation; thus, a particle will remain along its initial Jeffery orbit indefinitely. However, most colloidal systems are Brownian and the orientation of a particle is affected by random collisions with solvent molecules. This ultimately allows for a steady distribution of particle orientation. Rotational Brownian motion is not the only mechanism by which a steady orientation distribution can be achieved. Rahnama et al.¹³³ show that the hydrodynamic interactions in a suspension of non-Brownian fibers also allows for a steady orientation distribution. With the inclusion of rotational Brownian motion, which is the mechanism for relaxation of the micro-mechanical model used herein, the system is no longer deterministic and a statistical description of the microstructure is required. A convenient measure is the orientation distribution function, $\psi(\mathbf{p}, t^*)$, where $\psi(\mathbf{p}, t^*) \sin \theta d\theta d\phi$ represents the likelihood of a particle oriented in a differential solid angle about (θ, ϕ) , and θ and ϕ are the polar and azimuthal angles, respectively, of a spherical coordinate system (see Figure 4.2). The orientation unit vector is restricted to the surface of a unit sphere, requiring that the orientation distribution

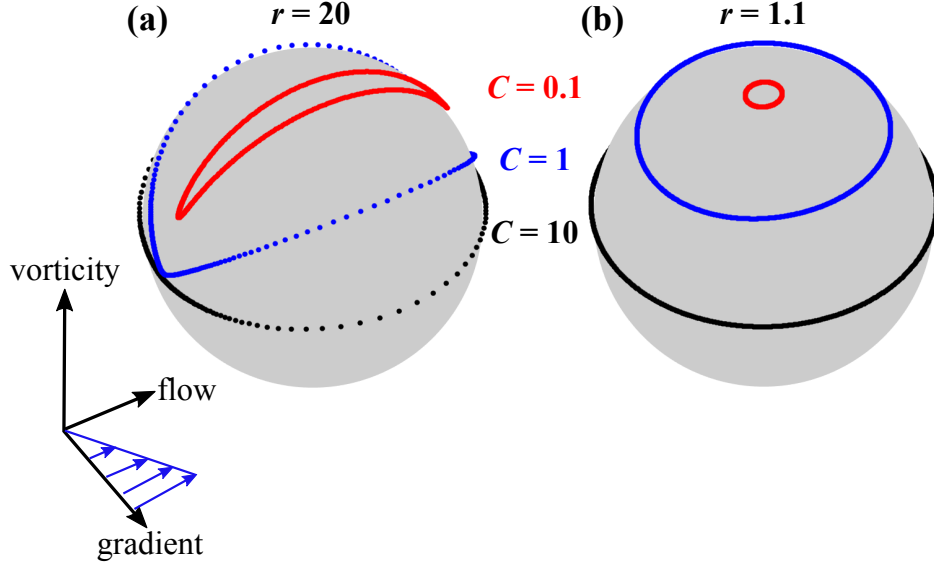


Figure 4.3: Jeffery orbits for a (a) prolate spheroid ($r = 20$) and (b) nearly-spherical particle ($r = 1.1$) for orbit constants $C = 0.1, 1$, and 10 , phase $\kappa = 0$, and shear rate $\dot{\gamma}_0 = 10 \text{ s}^{-1}$. The discrete points in time are evenly spaced over a period of a Jeffery orbit, $T_{JO} = 2\pi(r + r^{-1})/\dot{\gamma}_0$. In (a), a particle trajectory traces large circles with a non-uniform velocity along an orbit. Here, the discrete points are clustered near the flow axis for $C = 1, 10$, indicating that a particle spends most of the period of a Jeffery orbit aligned with the flow. Conversely, in (b) the distribution of orientations over a period of a Jeffery orbit is nearly uniform as a particle simply rotates with half the ambient vorticity of the flow.

function satisfy a normalization condition at all instances in time,

$$\int \psi(\mathbf{p}, t^*) dS = 1, \quad (4.5)$$

where $dS = \sin \theta d\theta d\phi$ is the differential solid angle over a unit sphere.

The orientation distribution function satisfies the conservation, or Fokker-Planck, equation ^{12,13,65}

$$\frac{\partial \psi}{\partial t^*} + \nabla_{\mathbf{p}} \cdot (\dot{\mathbf{p}} \psi) = 0. \quad (4.6)$$

where $\nabla_{\mathbf{p}} = (\mathbf{I} - \mathbf{p}\mathbf{p}) \cdot \nabla$ is the surface gradient operator, \mathbf{I} is the identity tensor, and $\dot{\mathbf{p}}$ is the temporal evolution of the orientation unit vector,

$$\dot{\mathbf{p}} = \dot{\mathbf{p}}_J - D_r \nabla_{\mathbf{p}} \ln \psi. \quad (4.7)$$

Here, D_r is a rotational diffusion coefficient. Equation (4.7) results from a torque balance with

contributions from the vorticity and straining components of the flow and rotational Brownian motion. Equations (4.5)-(4.7) have previously been solved for the case of steady simple shear. For $Wi \ll 1$, Brownian motion is dominant and the orientation remains essentially isotropic; the first effect of the imposed flow is to align particles along the extensional axes of the flow. Here, a solution to (4.5)-(4.7) can be achieved through a regular perturbation expansion^{134,135} or a Galerkin (spherical harmonics) expansion^{96,135}. For $Wi \gg 1$, the effect of Brownian motion is dampened and the orientation distribution function follows a Jeffery orbit. As shown by Leal and Hinch¹⁰, here the first effect of Brownian motion is to select a distribution of orbit constants, C , and phase, κ . For elongated particles ($r \gg 1$), the likely orbits are those in which the particles spend the majority of the time aligned along the flow axis. A simple transformation, $r \rightarrow 1/r$ and $\phi \rightarrow \phi + \pi/2$, shows that oblate particles tend to spend most of the the time over an orbit aligned along the velocity gradient direction (normal to the flow axis)¹¹. Furthermore, Hinch and Leal¹¹ identify an intermediate regime, $Wi \gg 1$ and $Wi \ll (r + 1/r)^3$, for which particles essentially follow Jeffery orbits, but the velocity in the slow portion of the orbit is so small that the rate of Brownian motion is comparable to the rate of advection along the orbit in that region, even though $Wi \gg 1$. This leads to an orientational boundary layer of thickness $O(Wi^{-1/3})$ in which the orientation distribution is strongly peaked about $\theta \sim \pi/2$ and $\phi \sim 0$, with a small, $O(Wi^{-1/3})$, fraction of orientations outside the boundary layer.

For $B \equiv 1$, the micro-mechanical model described herein reduces to the rigid-dumbbell model used in the kinetic theory of polymers. Here, a particle is equally affected by the vorticity and straining component of the flow, and the trajectories in (4.3)-(4.4) predict a terminal orientation along the flow axis as the period of a Jeffery orbit is infinite⁹⁶. Bird et al.⁵ provide a thorough discussion of the stress dynamics of a rigid-dumbbell suspension under steady shear, small amplitude oscillatory shear, and steady elongation. The rigid dumbbell model has, more recently, been investigated under a large amplitude oscillatory shear flow via a regular perturbation expansion about small Wi ^{7,8}.

The particle contribution to the stress tensor, τ^P , can be determined from an ensemble average

of the stresslet ^{11,12}

$$\begin{aligned} \frac{\boldsymbol{\tau}^P}{\mu_s c} = & 4A_H \mathbf{E}^* : \langle \mathbf{p}\mathbf{p}\mathbf{p}\mathbf{p} \rangle + 4B_H \left(\mathbf{E}^* \cdot \langle \mathbf{p}\mathbf{p} \rangle + \langle \mathbf{p}\mathbf{p} \rangle \cdot \mathbf{E}^* - \frac{2\mathbf{I}}{3} \mathbf{E}^* : \langle \mathbf{p}\mathbf{p} \rangle \right) \\ & + 2C_H \mathbf{E}^* + 2F_H D_r \left(\langle \mathbf{p}\mathbf{p} \rangle - \frac{\mathbf{I}}{3} \right), \end{aligned} \quad (4.8)$$

where the angled brackets are averages of the moments of the orientation unit vector,

$$\langle \mathbf{p}\mathbf{p} \rangle = \int \mathbf{p}\mathbf{p} \psi(\mathbf{p}, t^*) dS, \quad (4.9)$$

and

$$\langle \mathbf{p}\mathbf{p}\mathbf{p}\mathbf{p} \rangle = \int \mathbf{p}\mathbf{p}\mathbf{p}\mathbf{p} \psi(\mathbf{p}, t^*) dS. \quad (4.10)$$

which require a solution of (4.6) to compute. $A_H, B_H, C_H,$ and F_H are scalar coefficients that solely depend on the particle aspect ratio ^{11,12}. The terms in (4.8) proportional to \mathbf{E}^* originate from the hydrodynamic stresslet generated by the inability of a rigid particle to deform with the straining component of the flow. ^{11,14} In a transient flow, such as an oscillatory flow, the hydrodynamic contribution to the stress is zero when the flow vanishes.

The last term in (4.8) is a direct Brownian contribution arising from the entropic torque generated by rotational Brownian motion and is solely dependent upon the second moment of the orientation distribution function. The evolution of this second moment, and thus the direct Brownian stress, can be obtained by multiplying (4.6) by $(\mathbf{p}\mathbf{p} - \mathbf{I}/3)$ and integrating over \mathbf{p} -space ^{15,136},

$$\begin{aligned} \frac{\partial}{\partial t} \langle \mathbf{p}\mathbf{p} \rangle - \boldsymbol{\Omega}^{*T} \cdot \langle \mathbf{p}\mathbf{p} \rangle - \langle \mathbf{p}\mathbf{p} \rangle \cdot \boldsymbol{\Omega}^* - B \left[\mathbf{E}^* \cdot \langle \mathbf{p}\mathbf{p} \rangle + \langle \mathbf{p}\mathbf{p} \rangle \cdot \mathbf{E}^* \right] \\ = 6D_r \left[\frac{\mathbf{I}}{3} - \langle \mathbf{p}\mathbf{p} \rangle \right] - 2B \langle \mathbf{p}\mathbf{p}\mathbf{p}\mathbf{p} \rangle : \mathbf{E}^*. \end{aligned} \quad (4.11)$$

Unfortunately, (4.11) depends on the unknown higher-order moment $\langle \mathbf{p}\mathbf{p}\mathbf{p}\mathbf{p} \rangle$ and thus cannot be solved exactly; the same is true for the evolution equation of any finite moment of \mathbf{p} . However, a qualitative understanding of the evolution of the Brownian stress can be obtained for limiting values

of B . In the rigid dumbbell limit ($B = 1$), the left-hand-side of (4.11) is the co-deformational, or upper-convected, material derivative of $\langle \mathbf{pp} \rangle$ and describes its rate of change while translating and deforming (i.e. rotating and straining) with a fluid element. Here, the microstructure aligns with the flow axis under steady shear, and thus the Brownian stress should be relatively constant. This feature is shared by constitutive equations that involve the upper convected derivative of the stress tensor, such as the Giesekus model. Hence, we would expect similar dynamics between the total stress from the Giesekus model and the Brownian stress of the rigid dumbbell micro-mechanical model. For $B \simeq 0$, the microstructure rotates with half of the ambient vorticity. In the limit of nearly-spherical particles, $B \simeq 0$, the left-hand-side of (4.11) reduces to the co-rotational, or Jaumann, derivative of $\langle \mathbf{pp} \rangle$, and describes its evolution while translating and rotating with a fluid element. Here, the microstructure rotates at half the ambient vorticity and rapid oscillations in the stress are observed¹³⁰. This feature is likely shared with constitutive models that involve a co-rotational derivative of the stress, such as the co-rotational Maxwell model.

4.2.2 Oscillatory Shear Flow

The specific deformation employed in this work is an oscillatory shear flow with velocity field $\mathbf{v}^*(t^*) = \dot{\gamma}_0 \cos(\omega t^*) y \mathbf{e}_x$ and velocity gradient $\mathbf{\Gamma}^*(t^*) = \dot{\gamma}_0 \cos(\omega t^*) \mathbf{e}_y \mathbf{e}_x$, where $\Gamma_{i,j}^* = \partial v_j^* / \partial x_i$. Here, x, y , and z are Cartesian coordinates and \mathbf{e}_x and \mathbf{e}_y are unit vectors along the x (flow) and y (flow-gradient) directions, respectively. Thus, substitution of the above oscillatory velocity field into (4.6) and (4.7), and defining the relaxation time as $\lambda = 1/6D_r$, yields a dimensionless Fokker-Planck equation,

$$\frac{\partial \psi}{\partial t} + Wi \cos(De t) \nabla_{\mathbf{p}} \cdot (\dot{\mathbf{p}}_J \psi) = \frac{1}{6} \nabla_{\mathbf{p}}^2 \psi, \quad (4.12)$$

where $Wi = \dot{\gamma}_0/6D_r$ is a Weissenberg number, $De = \omega/6D_r$ is a Deborah number, and $t = 6D_r t^*$ is a dimensionless time. The relaxation time of $\lambda = 1/(6D_r)$ is chosen as this is the time-scale over which the stress relaxes upon flow cessation and the relaxation time-scale obtained from linear viscoelasticity^{65,137}. Other relaxation times do occur for elongated particles in strong flows when $Wi \gg 1$ ^{11,128,137}. However, our choice is convenient to allow consistent comparison across the

entire $Wi - De$ space.

For $Wi \ll 1$, the material is only slightly shifted out of equilibrium, and the resulting response is linear in the imposed flow; this is typically referred to as a small-amplitude oscillatory shear (SAOS). Two conditions must be met to ensure one is operating in the LAOS regime to obtain a non-linear material response : 1) the rate of relaxation is less than the rate of deformation, $Wi > 1$, and 2) the strain cannot be small, $\gamma_0 = \dot{\gamma}_0/\omega = Wi/De \geq 1$. If the oscillation frequency is much greater than the strain-rate amplitude, the deformation over an oscillation cycle cannot fully propagate through the material and the response will be quasi-linear in the imposed flow. Alternatively, when $Wi > 1$ and $De \sim O(1)$, the nonlinear and unsteady viscoelasticity of the material becomes apparent.

We define a non-equilibrium orientation distribution, $\psi(\mathbf{p}, t) = (1 + f(\mathbf{p}, t))/4\pi$, where $\psi = 1/4\pi$ is the equilibrium solution for an isotropic material and f characterizes departures from equilibrium. The non-equilibrium orientation distribution function satisfies the normalization condition,

$$\int f(\mathbf{p}, t) dS = 0, \quad (4.13)$$

and initial condition $f(\mathbf{p}, t = 0) = 0$. The dimensionless Fokker-Planck equation in (4.12) parameterized in spherical coordinates is (Figure 4.2),

$$\begin{aligned} \frac{\partial f}{\partial t} + \frac{Wi \cos(De t)}{2} \left[\frac{B \sin 2\theta \sin 2\phi}{2} \frac{\partial f}{\partial \theta} + (B \cos 2\phi - 1) \frac{\partial f}{\partial \phi} - 3B \sin^2 \theta \sin 2\phi f \right] \\ - \frac{1}{6} \left(\frac{\partial^2 f}{\partial \theta^2} + \cot \theta \frac{\partial f}{\partial \theta} + \frac{1}{\sin^2 \theta} \frac{\partial^2 f}{\partial \phi^2} \right) = \frac{3B Wi}{2} \cos(De t) \sin^2 \theta \sin 2\phi. \end{aligned} \quad (4.14)$$

The first bracketed quantity, proportional to $Wi \cos(De t)$, of (4.14) represents the advective contribution from the imposed flow, which acts to concentrate the orientation density along Jeffery orbits. The second bracketed quantity is simply the angular portion of the Laplacian operator and represents relaxation via rotational Brownian diffusion, which acts to randomize the orientation (i.e. phase and orbital constant). The right-hand-side of (4.14) is the contribution of the equilib-

rium microstructure, which acts as a forcing term.

The stress tensor in (4.8) can be specified for the oscillatory shear flow given above by substitution of the orientation unit vector in spherical coordinates,

$$\mathbf{p} = \sin \theta \cos \phi \mathbf{e}_x + \sin \theta \sin \phi \mathbf{e}_y + \cos \theta \mathbf{e}_z, \quad (4.15)$$

and the appropriate rate of strain tensor. From there, the shear stress, τ_{yx} , and normal stress differences, N_1 and N_2 , can be decomposed into a hydrodynamic, or flow-induced, and Brownian, or indirect, contributions¹¹. The components of the shear stress are,

$$\frac{\tau_{yx}^H}{\mu_s c \dot{\gamma}_0} = \eta^{eq} + \left[A_H \langle \sin^4 \theta \sin^2 2\phi \rangle + B_H \langle \sin^2 \theta \rangle \right] \cos(De t), \quad (4.16)$$

and

$$\frac{\tau_{yx}^B}{\mu_s c \dot{\gamma}_0} = \frac{F_H}{6Wi} \langle \sin^2 \theta \sin 2\phi \rangle, \quad (4.17)$$

where the superscripts ‘ H ’ and ‘ B ’ indicate the hydrodynamic or Brownian contribution, respectively, and η^{eq} is the hydrodynamic viscosity that arises from the equilibrium microstructure¹¹,

$$\eta^{eq} = \left(\frac{4A_H}{15} + \frac{4B_H}{3} + C_H \right) \cos(De t). \quad (4.18)$$

This contribution is always in-phase with the strain-rate and is thus purely viscous. Likewise, the normal stress differences, $N_1 = \tau_{yy} - \tau_{xx}$ and $N_2 = \tau_{zz} - \tau_{yy}$, can be decomposed as,

$$\frac{N_1^H}{\mu_s c \dot{\gamma}_0} = -A_H \langle \sin^4 \theta \sin 4\phi \rangle \cos(De t), \quad (4.19)$$

$$\frac{N_1^B}{\mu_s c \dot{\gamma}_0} = -\frac{F_H}{3Wi} \langle \sin^2 \theta \cos 2\phi \rangle, \quad (4.20)$$

and

$$\frac{N_2^H}{\mu_s c \dot{\gamma}_0} = \left[2A_H \langle \sin^2 \theta \sin 2\phi (\cos^2 \theta - \sin^2 \theta \sin^2 \phi) \rangle - 2B_H \langle \sin^2 \theta \sin 2\phi \rangle \right] \cos(Det), \quad (4.21)$$

$$\frac{N_2^B}{\mu_s c \dot{\gamma}_0} = \frac{F_H}{3W_i} \langle \cos^2 \theta - \sin^2 \theta \sin^2 \phi \rangle, \quad (4.22)$$

respectively.

Another useful metric in quantifying the dynamics of the microstructure is through rheo-optical, or birefringence, techniques, which measure the flow-induced anisotropy of the suspension. Specifically, one can calculate (or measure) the average orientation angle, χ , in the shear plane (flow-gradient plane) and the extent of alignment about that angle, $\Delta n''$. These quantities are determined from the eigenvalues of the imaginary component of the effective refractive index tensor of the suspension. In the Rayleigh limit of light-scattering, where the length scale of the particles is much smaller than the wavelength of incident light, these are^{138–141},

$$\tan 2\chi = \frac{\langle \sin^2 \theta \sin 2\phi \rangle}{\langle \sin^2 \theta \cos 2\phi \rangle}, \quad (4.23)$$

and

$$\frac{\Delta n''}{\Delta n''_{\max}} = \left[\langle \sin^2 \theta \sin 2\phi \rangle^2 + \langle \sin^2 \theta \cos 2\phi \rangle^2 \right]^{1/2}. \quad (4.24)$$

The orientation angle and linear dichroism can also be expressed in terms of the Brownian contribution to the shear stress (4.17) and first normal stress difference (4.20) as,

$$\tan 2\chi = \frac{\tau_{yx}^B}{-N_1^B/2}, \quad (4.25)$$

and

$$\frac{\Delta n''}{\Delta n''_{\max}} = \frac{6Wi}{F_H} \left[(\tau_{yx}^B)^2 + \left(\frac{N_1^B}{2} \right)^2 \right]^{1/2}. \quad (4.26)$$

Thus, the birefringence measurements of a dilute suspension of rigid, anisotropic particles provides a measure of the entropic, or Brownian, evolution of the stress in the suspension. This is in contrast to birefringence measurements of polymer solutions or semi-dilute rigid rod suspensions, where the stress-optic law applies and the *total* shear stress and first normal stress difference can be inferred from the average orientation angle and linear dichroism¹⁴⁰.

4.3 Numerical Solution Method

We limit our analysis to the long-time oscillatory response of the material, neglecting any initial transience resulting from the start-up of the flow. Thus, we pose a solution to (4.14) as a series of Fourier harmonics of base frequency De ,

$$f(\mathbf{p}, t) = \sum_{\ell=-\infty}^{\infty} f^{\ell}(\mathbf{p}) e^{i\ell De t}, \quad (4.27)$$

where $i = \sqrt{-1}$ and the coefficients $f^{\ell}(\mathbf{p})$ are solely dependent upon \mathbf{p} . Substitution of (4.27) into (4.14) yields,

$$\begin{aligned} & \left[i\ell De - \frac{1}{6} \left(\frac{\partial^2}{\partial \theta^2} + \cot \theta \frac{\partial}{\partial \theta} + \frac{1}{\sin^2 \theta} \frac{\partial^2}{\partial \phi^2} \right) \right] f^{\ell} \\ & + Wi \left[\frac{B \sin 2\theta \sin 2\phi}{8} \frac{\partial}{\partial \theta} + \left(\frac{B \cos 2\phi - 1}{4} \right) \frac{\partial}{\partial \phi} - \frac{3B}{4} \sin^2 \theta \sin 2\phi \right] (f^{\ell+1} + f^{\ell-1}) \\ & = \frac{3BWi}{4} \sin^2 \theta \sin 2\phi (\delta_{\ell,1} + \delta_{\ell,-1}) \end{aligned} \quad (4.28)$$

where δ_{ij} is the Kronecker delta function. From (4.28), it is evident that each temporal mode, f^{ℓ} , is coupled to $f^{\ell+1}$ and $f^{\ell-1}$ through oscillatory advection, the strength of which is dictated by the magnitude of Wi . This is analogous to the problem of large amplitude oscillatory microrheology,

investigated by Swan et al.⁷², where the structural modes of the pair distribution function, governed by the Smoluchowski equation, are also coupled through oscillatory advection. The orientation distribution function is a real-valued function, thus requiring that $f^{-\ell}$ and f^ℓ be related by their complex conjugates, $f^{-\ell} = \hat{f}^\ell$; the hatted symbol indicates the complex conjugate. Substituting (4.27) into (4.8), for example, yields for the shear stress,

$$\begin{aligned} \frac{\tau_{yx}^P}{\mu_s c \dot{\gamma}_0} = & \eta^{eq} + \frac{1}{4\pi} \sum_{\ell=-\infty}^{\infty} \left[\left(e^{i(\ell+1)Det} + e^{i(\ell-1)Det} \right) \left(\frac{A_H}{2} \int \sin^4 \theta \sin^2 2\phi f^\ell dS + B_H \int \sin^2 \theta f^\ell dS \right) \right. \\ & \left. + e^{i\ell Det} \left(\frac{F_H}{Wi} \int \sin^2 \theta \sin 2\phi f^\ell dS \right) \right]. \end{aligned} \quad (4.29)$$

The normal stress differences and birefringence parameters can be calculated in an analogous manner (see Section 4.A.1).

A finite-difference approach is utilized to solve for the temporal modes in (4.28). A uniform grid is applied in ϕ and a scaled polar angle, $\beta = \exp(-Wi^{1/3} \cos \theta)$, is introduced. The cosine transformation acts to cluster points near $\theta = \pi/2$. In the intermediate regime of weak Brownian rotation ($Wi \gg 1$) and elongated particles ($Wi^{1/3} \ll r + r^{-1}$), the steady shear orientation distribution function is peaked at $\theta \sim \pi/2$, indicating that the particles spend a majority of the time in the flow-gradient plane^{11,129}. A scaling factor of $Wi^{1/3}$ is chosen as this is the width of the orientational boundary layer formed under a strong, steady shear flow^{11,142}. Equation (4.28) is axisymmetric and can be solved on the quarter-plane $\beta \in [e^{-Wi^{1/3}}, 1]$ ($\theta \in [0, \pi/2]$) and $\phi \in [0, \pi]$ as opposed to over the full half-plane. The harmonics, $f^\ell(\theta, \phi)$, must satisfy the following boundary conditions. First, a mirror boundary condition about $\theta = \pi/2$,

$$f^\ell \left(\frac{\pi}{2} - \delta, \phi \right) = f^\ell \left(\frac{\pi}{2} + \delta, \phi \right), \quad (4.30)$$

where $\delta \in [0, \pi/2]$. Secondly, a periodic boundary condition about $\phi = \pi$,

$$f^\ell(\theta, \epsilon) = f^\ell(\theta, \pi + \epsilon), \quad (4.31)$$

where $\epsilon = [0, \pi]$. Two additional boundary conditions can be determined by analyzing the orientation distribution function as expanded in spherical harmonics⁹⁶,

$$f^\ell(\theta, \phi) = \sum_{n=2}^N \sum_{m=0}^n \begin{cases} s_{\ell,n}^m P_n^m(\cos \theta) \sin(m\phi) & \ell \text{ odd} \\ c_{\ell,n}^m P_n^m(\cos \theta) \cos(m\phi) & \ell \text{ even} \end{cases}, \quad (4.32)$$

where $c_{\ell,n}^m$ and $s_{\ell,n}^m$ are scalar coefficients and P_n^m is an associated Legendre polynomial. At $\theta = 0$, $P_n^m(1)$ is only non-zero for $m = 0$; thus, for odd ℓ the modes are zero,

$$f^\ell(0, \phi) = 0 \quad (\text{for odd } \ell), \quad (4.33)$$

and even ℓ modes are only a function of ϕ ,

$$\left. \frac{\partial f^\ell}{\partial \theta} \right|_{\theta=0} = 0 \quad (\text{for even } \ell). \quad (4.34)$$

Finally, at $\phi = 0$, the odd ℓ modes are zero,

$$f^\ell(\theta, 0) = 0 \quad (\text{for odd } \ell), \quad (4.35)$$

and even ℓ the modes are only a function of θ ,

$$\left. \frac{\partial f^\ell}{\partial \phi} \right|_{\phi=0} = 0 \quad (\text{for even } \ell). \quad (4.36)$$

We have chosen not to utilize a spherical harmonics expansion in the solution of the non-equilibrium orientation distribution function because this approach results in an ill-conditioned matrix system for $Wi \gtrsim O(1)$ ⁹⁶, whereas the approach described herein is well-conditioned (see Section 4.A.2).

A second-order central difference scheme is applied to (4.28) in both β and ϕ resulting in the

discretized equation,

$$\begin{aligned}
& A_{i,j} f_{i,j+1}^\ell + B_{i,j} f_{i,j-1}^\ell + C_{i,j} (f_{i+1,j}^\ell + f_{i-1,j}^\ell) + D_{i,j}^\ell f_{i,j}^\ell + E_{i,j} (f_{i,j+1}^{\ell+1} - f_{i,j-1}^{\ell+1} + f_{i,j+1}^{\ell-1} - f_{i,j-1}^{\ell-1}) \\
& + F_{i,j} (f_{i+1,j}^{\ell+1} - f_{i-1,j}^{\ell+1} + f_{i+1,j}^{\ell-1} - f_{i-1,j}^{\ell-1}) + G_{i,j} (f_{i,j}^{\ell+1} + f_{i,j}^{\ell-1}) = R_{i,j} \delta_{\ell,\pm 1}
\end{aligned} \tag{4.37}$$

where,

$$\begin{aligned}
A_{i,j} &= \left((\ln \beta_i)^2 - Wi^{2/3} \right) \frac{\beta_i^2}{6\Delta\beta^2}, \\
B_{i,j} &= \left((\ln \beta_i)^2 - Wi^{2/3} \right) \frac{\beta_i}{6\Delta\beta} + \frac{\beta_i \ln \beta_i}{6\Delta\beta}, \\
C_{i,j} &= \frac{1}{6\Delta\phi^2} \frac{Wi^{2/3}}{(\ln \beta_i)^2 - Wi^{2/3}}, \\
D_{i,j}^\ell &= i\ell De - 2(A_{i,j} + C_{i,j}), \\
E_{i,j} &= Wi \left(\frac{B \cos 2\phi_j - 1}{8\Delta\phi} \right), \\
F_{i,j} &= \frac{Wi B}{8\Delta\beta} \beta_i \ln \beta_i \left(Wi^{-2/3} (\ln \beta_i)^2 - 1 \right) \sin 2\phi_j, \\
G_{i,j} &= \frac{3Wi B}{4} \left(Wi^{-2/3} (\ln \beta_i)^2 - 1 \right) \sin 2\phi_j, \\
R_{i,j} &= \frac{3Wi B}{4} \left(1 - Wi^{-2/3} (\ln \beta_i)^2 \right) \sin 2\phi_j.
\end{aligned} \tag{4.38}$$

A point in the discretized spatial domain is labeled (β_i, ϕ_j) for $i \in [0, N + 1]$ and $j \in [0, M + 1]$ with grid spacing $(\Delta\beta, \Delta\phi) = (1/N, \pi/M)$. The resulting coupled set of ODEs can be compactly written as $\mathbf{M} \cdot \mathbf{f} = \mathbf{R}$, where \mathbf{M} is a sparse matrix containing 15 bands comprised of the coefficients in (4.38), \mathbf{f} is the solution vector for the non-equilibrium orientation distribution function, and \mathbf{R} is a forcing vector from the equilibrium microstructure at each point in space and time. The linear system is solved using sparse direct solvers in MATLAB[®]. The solution is deemed converged for a given Wi , De , and r when both the addition of spatial (N , M) and temporal nodes (L) results in less than a 1% relative change in the shear stress (see Section 4.A.2 for more details).

4.4 Results

A numerical solution to the Fokker-Planck equation for a dilute suspension of Brownian spheroids subject to an oscillatory shear flow over a range of flow strengths (Wi) and oscillation frequencies (De) is obtained. For simplicity, we have limited the majority of our analysis to prolate spheroids of aspect ratio $r = 20$; however, our numerical method is general and can be applied to other aspect ratios, including oblate spheroids, as we discussed in Section 4.2. For near-spheres, $r \approx 1$, the nonlinear viscoelastic regime is discussed by Khair¹³⁰.

Figure 4.4 is a Pipkin diagram comprised of a collection of Lissajous plots of the hydrodynamic and Brownian shear stress contributions over $Wi \in (0, 20]$ and $De \in (0, 100]$ as a function of the normalized strain-rate, $\cos(De t)$. In the weak deformation limit, $Wi \ll 1$, the hydrodynamic shear stress is the equilibrium contribution in (4.18) to leading order in Wi , resulting in a straight line at all De . The Brownian shear stress is elliptical over most values of De , as this is the source of the material's viscoelasticity in this regime. In the limit of large oscillation frequency, $De \gg 1$, or small extent of deformation, $Wi/De \ll 1$, the hydrodynamic shear stress is dominant over the Brownian shear stress over a majority of an oscillation cycle. Furthermore, the hydrodynamic shear stress is linear in the strain-rate at all Wi , analogous to the linear viscoelastic regime. In the limit of slow oscillations, $De \ll 1$, both shear stress contributions have a negligible amount of projected area, indicating a quasi-steady, viscous response. For larger flow strengths, $Wi \gtrsim 2$, the non-Newtonian, shear-thinning response of the material is observed. Finally, when the deformation is strong, $Wi \gg 1$, and the extent of deformation is not small, $Wi/De \geq 1$, both the hydrodynamic and Brownian shear stress exhibit a non-linear viscoelastic response, where secondary and sometimes tertiary loops are observed in the shear stress response. The secondary and tertiary loops observed in this regime correspond to over-shoots that one would observe during the start-up, or under-shoots upon the cessation, of a steady shear flow. This is unsurprising as an oscillatory deformation is a continual start-up and cessation flow, since the flow must pass through zero twice during an oscillation cycle. Beyond $Wi \simeq 10$, over all De , the stress response does not

significantly change when increasing Wi . Thus, our results have reached the large Wi regime. In what follows, we will address each of these regimes in more detail (see also Figure 4.1).

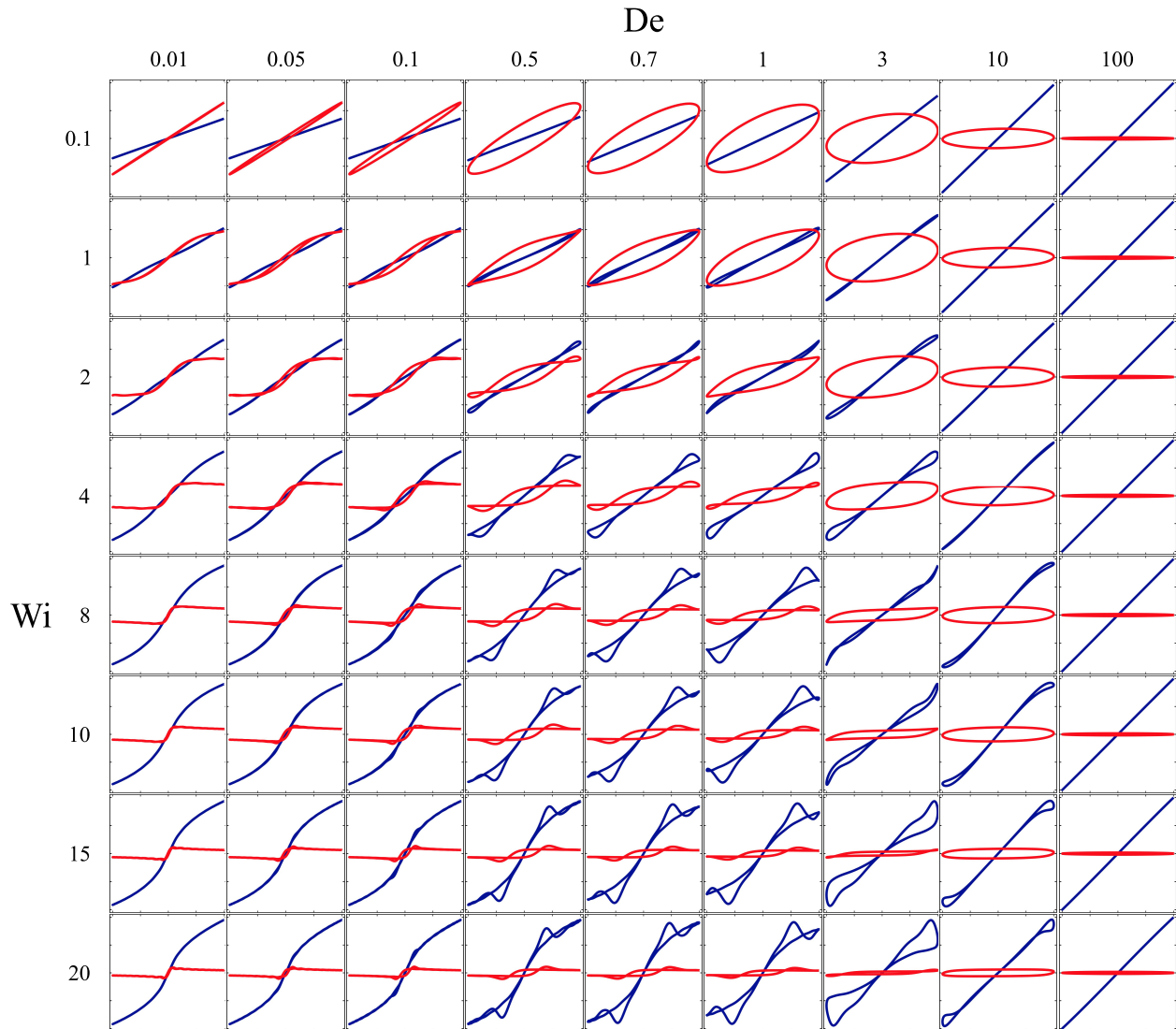


Figure 4.4: Pipkin diagram of Lissajous curves over a range of flow strengths (Wi) and oscillation frequencies (De). Each Lissajous plot shows the hydrodynamic (black (blue online)) and Brownian (gray (red online)) shear stress contribution versus the normalized strain-rate, $\cos(De t)$. The shear stress is normalized by the total shear stress at that (Wi, De) , so that the shear stress across the $Wi - De$ parameter space can be compared consistently.

4.4.1 Linear viscoelastic response: $Wi \ll 1$

In the linear viscoelastic regime, the rate of the imposed deformation, $\dot{\gamma}_0$, is much less than the rate of relaxation, $1/6D_r$ ($Wi \ll 1$). Here, the leading order non-equilibrium orientation distribution function is asymptotically small in Wi and the microstructure oscillates at the input frequency, De .

Formally we have¹¹,

$$f_{\text{LVE}} = \frac{3BWi}{2} \left[\frac{\cos(De t) + De \sin(De t)}{De^2 + 1} \right] \sin^2 \theta \sin(2\phi) + O(Wi^2). \quad (4.39)$$

Substitution of (4.39) into (4.8), (4.23), and (4.24) yields for the linear viscoelastic shear stress^{11,65,134},

$$\frac{\tau_{yx}^{\text{LVE}}}{\mu_s c \dot{\gamma}_0} = \eta^{eq} + \frac{F_H B}{15} \left(\frac{\cos(De t) + De \sin(De t)}{De^2 + 1} \right) + O(Wi^2), \quad (4.40)$$

orientation angle,

$$\chi^{\text{LVE}} = \text{sgn}(I_1) \frac{\pi}{4} + O(Wi^2), \quad (4.41)$$

and linear dichroism,

$$\frac{\Delta n''}{\Delta n''_{\text{max}}} = |I_1| + O(Wi^2), \quad (4.42)$$

where,

$$I_1 = \frac{2WiB}{5} \left(\frac{\cos(De t) + De \sin(De t)}{De^2 + 1} \right) \quad (4.43)$$

and sgn is the sign function. Normal stress differences are beyond the linear viscoelastic regime as they arise from the $O(Wi^2)$ microstructure deformation.

Figure 4.5 shows the non-equilibrium orientation distribution function given in (4.39) for $Wi = 0.1$ and $De = 0.1$ and 1 as a function of the strain rate, $\dot{\gamma}_0 \cos(De t)$. The microstructure will orient along the principle axes of strain in the flow-gradient plane, $\phi = \pm \pi/4$, and transition between the two axes based on the value of De . For instance, when $De \ll 1$, $f_{\text{LVE}} \sim \cos(De t)$ and the transition in orientation about the principle axes of strain will occur in-phase with the imposed flow, characteristic of a viscous liquid. Conversely, when $De \gg 1$, $f_{\text{LVE}} \sim \sin(De t)/De$ and the transition in orientation will occur 90° out-of-phase with the imposed flow, i.e. in phase with the strain, characteristic of an elastic solid. At intermediate De , the microstructure will behavior viscoelastically and the duration of the transition between the principle axes of strain will be out-of-phase with the imposed strain and strain-rate.

Figure 4.6(a) shows Lissajous plots of the hydrodynamic and Brownian components of the

shear stress as a function of the normalized strain-rate from (4.40). The hydrodynamic contribution solely arises from the equilibrium (isotropic) microstructure and is purely in-phase with the applied flow. The viscoelasticity of the material solely arises from the Brownian contribution, which has the greatest overall contribution to the shear stress at $De \sim O(1)$. Figure 4.6(b) shows Lissajous plots of the orientation angle (purple) and linear dichroism (green) given in (4.41)-(4.42) as a function of the normalized strain-rate. As discussed previously, the orientation of the microstructure oscillates between the principle axes of strain and the transition is dictated by the magnitude of De . Unsurprisingly, the magnitude of the linear dichroism remains close to zero regardless of the magnitude of De . This is because the microstructure is only slightly perturbed out of equilibrium.

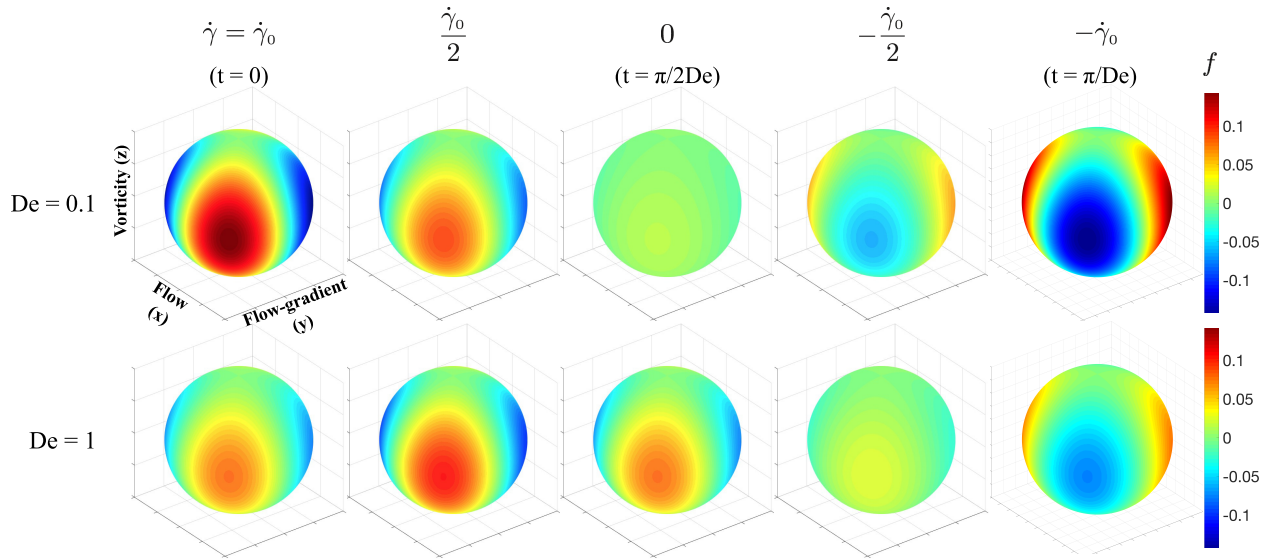


Figure 4.5: Non-equilibrium orientation distribution function in the linear viscoelastic regime, $Wi = 0.1$, given in (4.39) for $De = 0.1, 1$ at different instances in the strain-rate, $\dot{\gamma} = \dot{\gamma}_0 \cos(De t)$, over a half cycle, $t \in [0, \pi/De]$. Regions of red indicate likely orientations whereas regions of blue indicate unlikely orientations. The particles tend to align along the principle axes of strain in the flow-gradient plane ($\pm \pi/4$), which is supported by the value of the orientation angle given in (4.41).

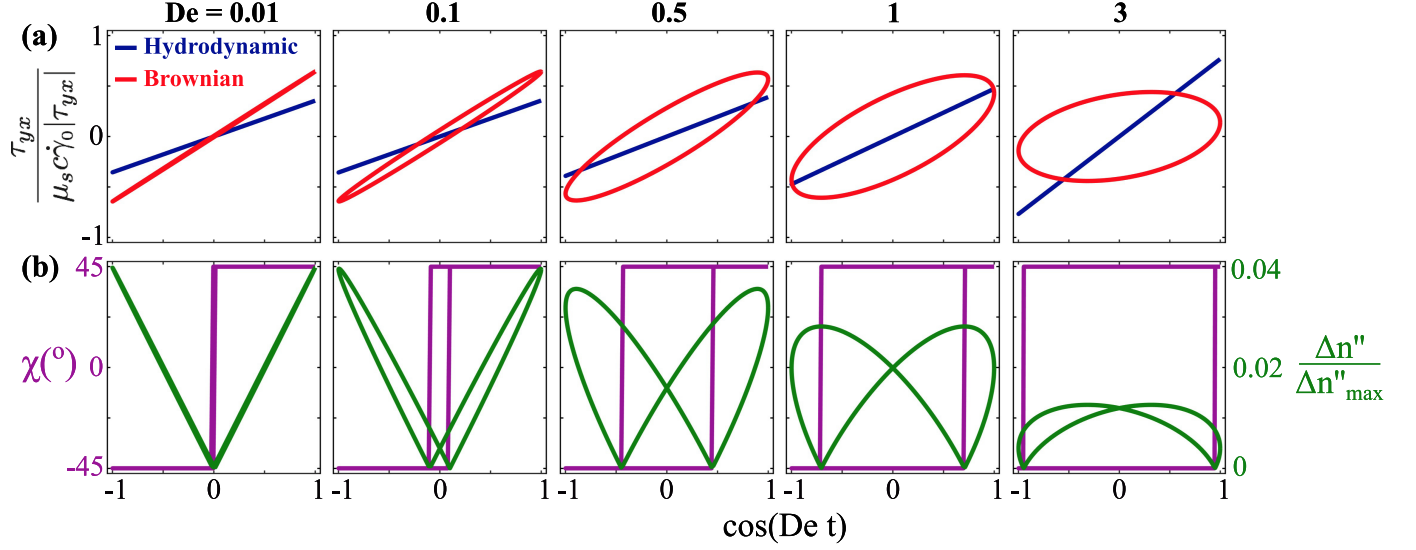


Figure 4.6: (a): Hydrodynamic (black, (blue online)) and Brownian (gray (red online)) shear stress contributions and (b): orientation angle (purple) linear dichroism (green) for $Wi = 0.1$ and $De = [0.01, 3]$.

4.4.2 Quasi-linear Response: $Wi > 1, Wi/De \ll 1$

In the large frequency limit, $De \gg 1$, the oscillation time scale is much less than time scale of relaxation. When the oscillation time scale is also much less than the time scale of the flow, $Wi/De = \gamma_0 \ll 1$, the material is not given sufficient time to deform, even under a strong deformation rate, resulting in a quasi-linear response. Figure 4.7 shows the non-equilibrium orientation distribution function at various instances in the shear cycle at $De = 100$ and $Wi \in [1, 20]$. We qualitatively observe that the material response is akin to the large frequency, *small* amplitude deformation regime, where the microstructure is aligned about the principle axes of strain and the transition between the two axes is 90° out-of-phase with the strain-rate, $f \sim De \sin(De t)$. As shown in Figure 4.8(a), the hydrodynamic shear stress contribution is dominant and is nearly entirely in-phase with the strain-rate. Thus, the hydrodynamic contribution is dominated by the equilibrium microstructure and not the distorted orientation distribution function that is 90° out-of-phase with the strain rate. Figure 4.8(b) shows that for a large-amplitude deformation, but small strain, the particles will align along the principle axes of strain, with an increased degree of alignment as Wi increases, and the transition between the axes will be nearly 90° out-of-phase with the strain-rate, as one would observe for an elastic solid; this is analogous to what is observed under a

small-amplitude deformation.

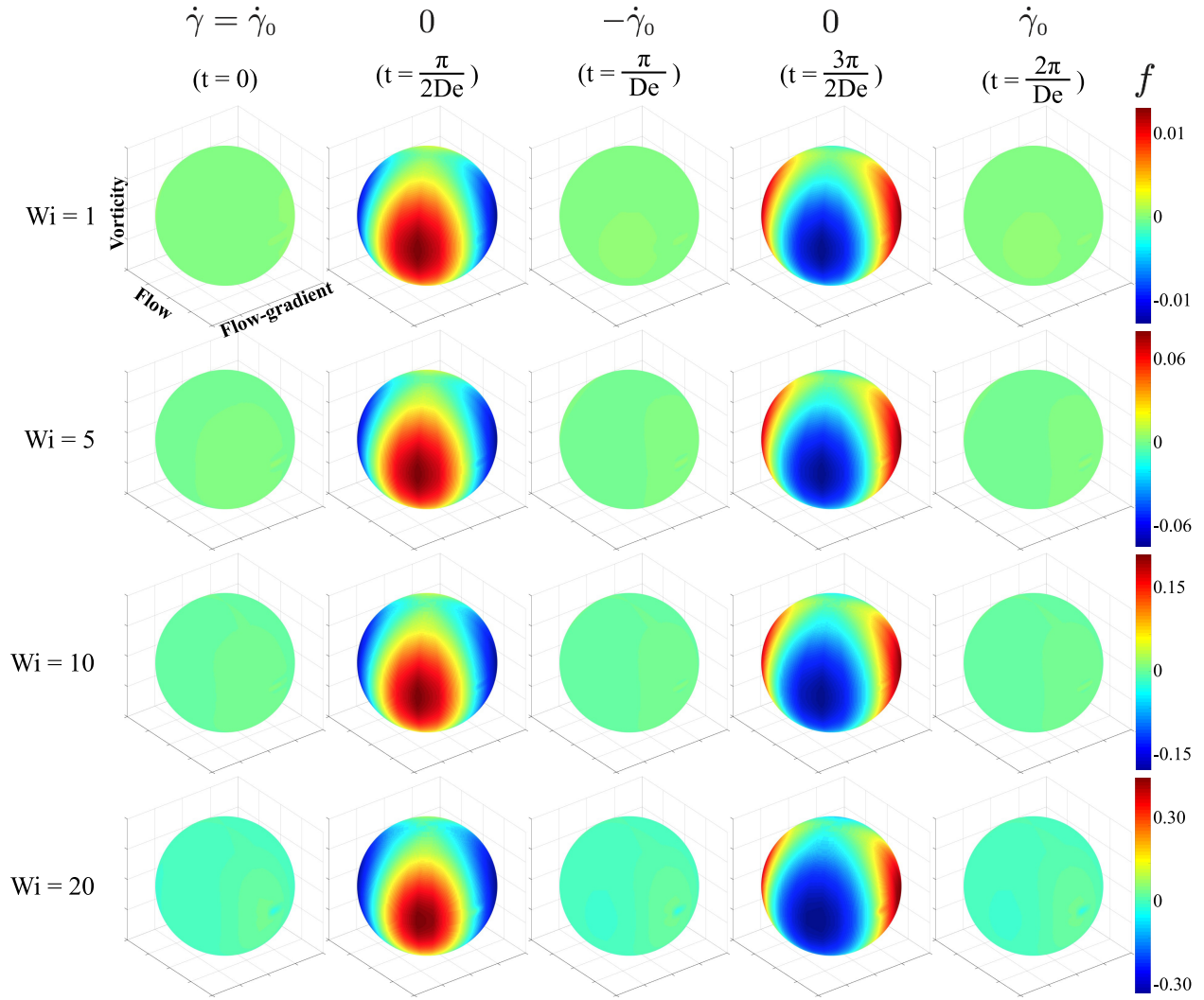


Figure 4.7: Non-equilibrium orientation distribution function in the quasi-linear viscoelastic regime at different instances in the strain-rate over a full-cycle, $t = [0, 2\pi/De]$, for $De = 100$ and $Wi = [1, 20]$. Regions of red indicate likely orientations whereas regions of blue indicate unlikely orientations. We qualitatively observe that $f \sim \sin(De t)$ as changes in the microstructure are 90° out-of-phase with the imposed strain-rate over all Wi investigated, similar to the large frequency limit of the linear response in Section 4.4.4.4.1

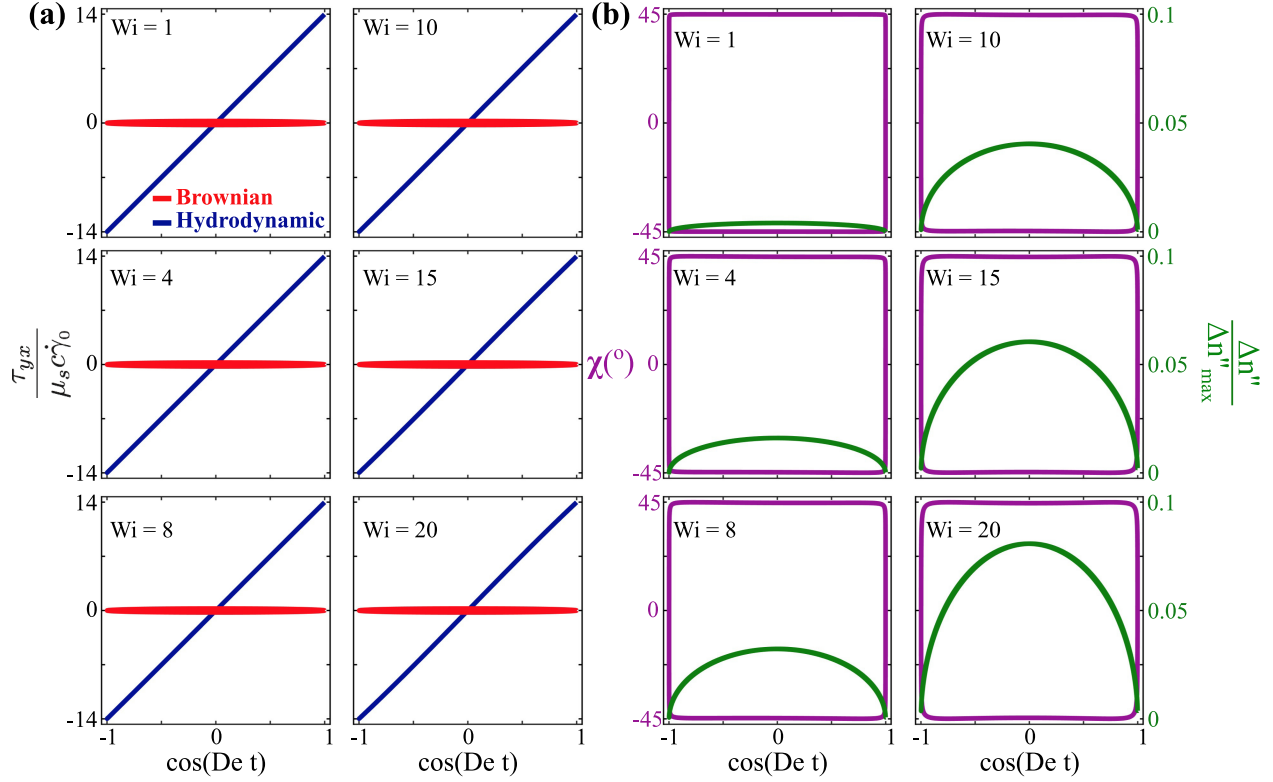


Figure 4.8: (a) Shear stress and (b) birefringence parameters in quasi-linear viscoelastic regime for $De = 100$ and $Wi = [1, 20]$. The shear stress is dominated by the equilibrium hydrodynamic component (black (blue online)), which is fully in-phase with the strain-rate. The Brownian shear stress (gray (red online)) is 90° out-of-phase with the strain rate and remains near zero at all points in an oscillation cycle. Over all flow strengths (Wi) investigated, the particles mainly align along the principle axes of strain, as is observed in SAOS. The linear dichroism remains small over all Wi , but does increase as the flow strength increases, characteristic of a nonlinear elastic deformation of the microstructure.

4.4.3 Quasi-steady response: $De \rightarrow 0$

In the small oscillation frequency limit, $De \ll 1$, the oscillation time scale is much greater than the time scale of relaxation resulting in a quasi-steady deformation. For $Wi \gtrsim O(1)$, the microstructure is strongly aligned with the flow axis during most of an oscillation cycle; the shear rate is strong enough to bias the particle orientation toward slower parts of the Jeffery orbit. In Figure 4.9 we qualitatively observe that as Wi increases, the degree of alignment along the flow axis is enhanced and the magnitude of the orientation distribution function increases. Also, the alignment of the microstructure about the flow axis oscillates in time and appears to be nearly in-phase with the oscillatory strain-rate. The orientation angle in Figure 4.10(b), over all Wi investigated, re-

mains near its minimum magnitude over the majority of an oscillation cycle; as the flow changes in direction, the sign of orientation of the particles also changes, but the magnitude remains the same (since the particles are fore-aft symmetric). Similarly, the linear dichroism is at a maximum when the strain-rate is at a maximum and decays to a minimum value when the flow vanishes.

Figure 4.10(a) shows the hydrodynamic and Brownian contributions to the shear stress. For $Wi > 1$, the increase of the hydrodynamic shear stress with strain-rate is sub-linear, indicating that the suspension is shear-thinning. Interestingly, the magnitude of the slope of the Brownian shear stress is also sub-linear and negative, $\Delta\tau_{yx}^B/\Delta\dot{\gamma} \sim -0.45$, for $Wi > 1$. Furthermore, there is nearly no projection of area in the Lissajous plots of either the hydrodynamic or Brownian shear stress contribution, indicating that the response is essentially viscous in nature, i.e. the stress evolves quasi-steadily with the imposed flow.

The steady shear response of a dilute suspension of spheroids subject to weak rotational Brownian motion was investigated by Hinch and Leal¹¹, who obtained an approximation to the steady-state orientation distribution function via a singular perturbation analysis. For weak Brownian rotation, $Wi \gg 1$, diffusion is negligible nearly everywhere in the domain with the exception of a boundary layer near the flow axis where advection and diffusion are of comparable strength; the width of this orientational boundary layer scales as $O(Wi^{-1/3})$. Hinch and Leal¹¹ ultimately found that for $1/(6Wi) \ll 1$ and $Wi^{1/3} \ll 6^{-1/3}(r + r^{-1})$, the hydrodynamic contribution to the shear stress scales as $\tau_{yx}^H \sim Wi^{2/3}$ (see their equation (48a)); a particle aspect ratio of $r = 20$ and the range of Wi used herein falls within this regime. Hinch and Leal¹¹ neglected the Brownian contribution to the shear stress as it is of lower order in Wi than the hydrodynamic contribution for $Wi \gg 1$. However, we observe that when the strain-rate is close to zero, the hydrodynamic and Brownian shear stress contributions are comparable. Thus, the Brownian contribution to the shear stress should not be naively neglected during the entirety of an oscillatory shear deformation, even if Wi at the maximum strain-rate is large. In Figure 4.10(a) we fit the scaling approximation of Hinch and Leal¹¹ to pass through zero when the flow vanishes and through the value of the hydrodynamic shear stress when the magnitude of the strain rate is at a maximum. A qualitative

agreement is observed between this scaling and our numerical results for the hydrodynamic shear stress at $De = 0.01$ and $Wi > 1$, indicating that at sufficiently low oscillation frequencies, the material response approaches a quasi-steady state limit. This also validates our numerical results.

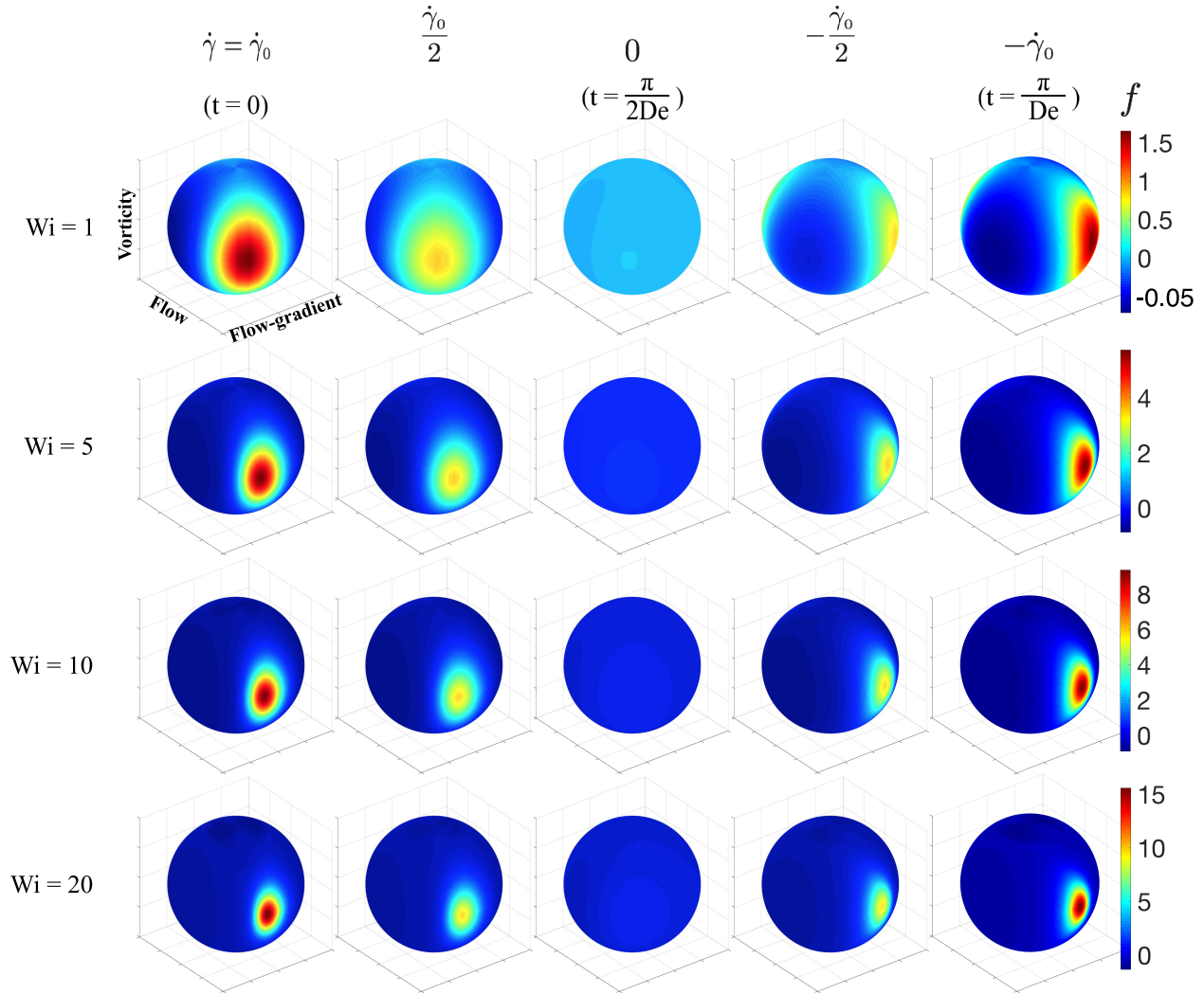


Figure 4.9: Non-equilibrium orientation distribution function in the quasi-steady viscoelastic regime at different instances in the strain-rate over a half-cycle, $t = [0, \pi/De]$ for $De = 0.01$ and $Wi = [1, 20]$. Regions of red indicate likely orientations whereas regions of blue indicate unlikely orientations. The alignment of the microstructure along the flow axis oscillates in time and appears to be in-phase with the strain-rate. Also, as Wi increases, the degree of alignment about the flow axis increases.

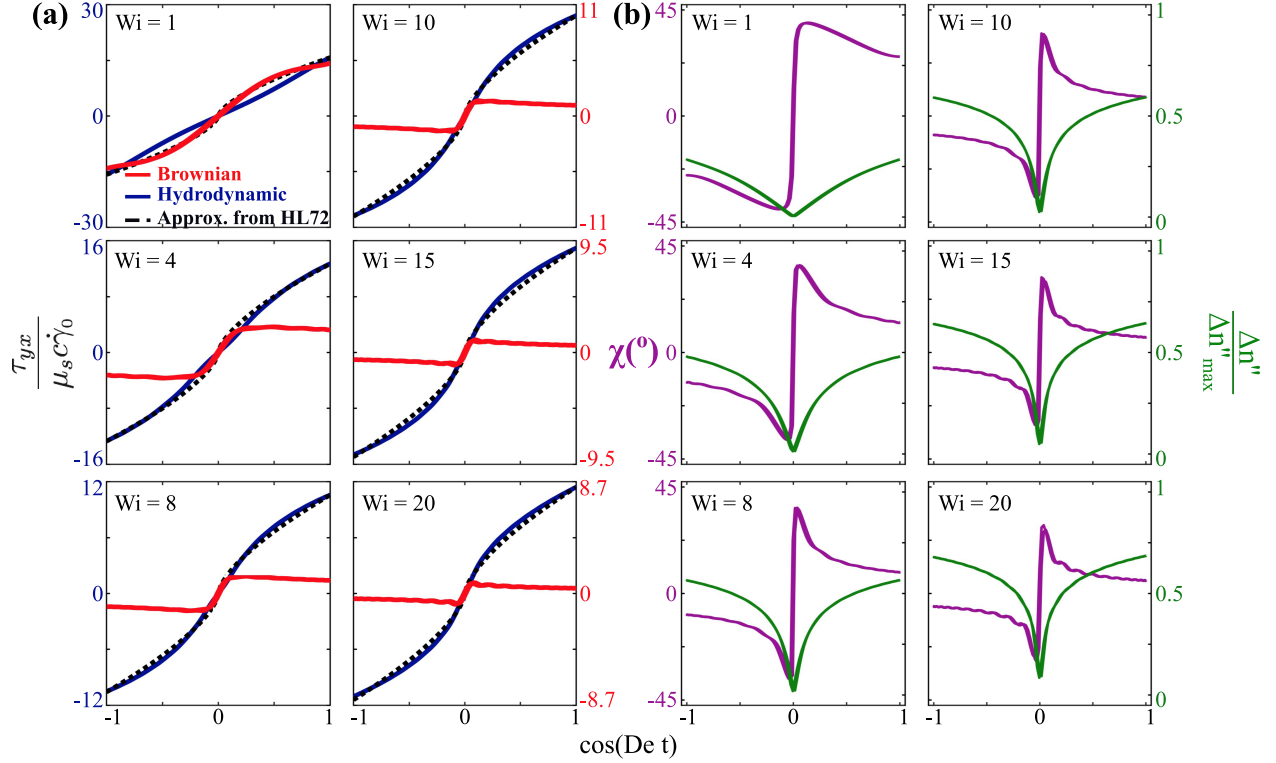


Figure 4.10: Shear Stress in the quasi-steady viscoelastic regime for $De = 0.01$ and $Wi = [1, 20]$. The hydrodynamic (black (blue online)) contribution to the shear stress dominates over the Brownian (gray (red online)) contribution at nearly all instances in an oscillation cycle. The exception occurs when the flow is near zero, $t \sim \pi/De$, when the two contributions are comparable. The blue dashed line is the scaling approximation for the steady hydrodynamic shear stress from Hinch and Leal¹¹ (denoted as HL72), which is fit to pass through zero when the flow vanishes and through the value of the hydrodynamic shear stress when the flow is at its maximum value, $\tau_{yx}^{HL} = \tau_{yx}^H|_{\dot{\gamma}=1} \cos^2/3(De t)$. This approximation qualitatively agrees with our numerical results for $Wi > 1$ and $De = 0.01$. The qualitative agreement between the steady shear scaling and the Brownian shear stress for $Wi = 1$ is coincidental. The average orientation angle (purple) remains at a minimum over most of an oscillation cycle and changes sign when the flow reverses direction. Similarly, the linear dichroism (green) is at a maximum when $|\dot{\gamma}| \sim 1$ and a minimum when $|\dot{\gamma}| \sim 0$.

4.4.4 Nonlinear Viscoelastic Response, $Wi \gtrsim 1$ and $Wi/De \gtrsim 1$

In the nonlinear viscoelastic regime, the deformation is strong, $Wi \sim O(1)$ and larger, and the rate of relaxation of the material is comparable to the oscillation frequency, $De \sim O(1)$, such that the transient, non-linear rheology of the material is interrogated. Figure 4.11 shows the non-equilibrium orientation distribution function for $De = 1$ and $Wi = [1, 20]$. Here, as Wi increases, the degree of alignment along the flow axis is enhanced, which is observed over a range of De (not shown). Also, as Wi increases, the particles tend to spend most their time aligned along the

flow direction with little distribution along the vorticity direction. At all Wi , when $De = O(1)$, the orientation distribution function is not in-phase with the rate of strain – there is a significant out-of-phase contribution resulting from the viscoelasticity of the material. Furthermore, when the flow vanishes, $\dot{\gamma} = 0$, a significant degree of alignment still exists as the microstructure is not given sufficient time to relax. The inability of the material to completely relax occurs because the time-scale over which the flow transitions is comparable to the relaxation time of the material. It is this inability to relax from a strongly aligned state that gives rise to the nonlinear viscoelastic response. As one transitions to $De < 1$, the time-scale of relaxation is less than the time-scale over which the flow transitions; and thus, the material is given sufficient time to relax over an oscillation cycle, as was shown in Section 4.4.4.3

Under a sufficiently strong deformation, $Wi \gtrsim 2$, and $De \sim O(1)$, the Lissajous curves in Figure 4.4 show secondary loops (or points of overlap) in both the hydrodynamic and Brownian shear stress; when $Wi \geq 10$ tertiary loops are also observed. The existence of secondary (and higher order) loops, or over/under-shoots, in the material response indicate significant microstructural variations are occurring over an oscillation cycle¹⁴³. Figure 4.12 shows the shear stress response at $De = 1$ at various Wi in both the time and strain-rate domain. At each Wi selected, an under-shoot is observed between $Det = [\pi/2, \pi]$, corresponding to a cross-over point on $\cos(De t) = [0, -1]$.

In this nonlinear viscoelastic regime, the hydrodynamic contribution to the shear stress (Figure 4.13a) is dominant over the Brownian shear stress contribution, with the exception of when the strain-rate is near zero, as the hydrodynamic shear stress must be zero when the flow vanishes. Here, the only viscoelasticity observed in the hydrodynamic shear stress is when the strain-rate is near its maximum. Otherwise, it is purely viscous and in-phase with the strain-rate; this can also be observed in the left column of Figure 4.12. As mentioned previously, tertiary loops, or secondary cross-over points, are observed in the hydrodynamic shear stress for $Wi \geq 10$. The Brownian shear stress, at all Wi investigated in this regime, is viscoelastic over an entire oscillation cycle and maintains a “bow-tie” shape with a single cross-over point in each oscillation half-cycle. Analogous to what is observed in the shear stress response, the hydrodynamic first

normal stress difference is dominant over the Brownian contribution through the majority of an oscillation cycle (Figure 4.13b). The exception being when the flow vanishes and the hydrodynamic first normal stress difference is zero and the Brownian contribution is non-zero. The hydrodynamic and Brownian first normal stress difference are viscoelastic over an entire oscillation cycle with a cross-over point when the flow vanishes. This cross-over point corresponds to the symmetry of the first normal stress difference over the half-cycle of an oscillation, i.e. $N_1(0 \leq Det \leq \pi/2) = N_1(\pi/2 \leq Det \leq \pi)$; again, the symmetry occurs because the particles are fore-aft symmetric. A secondary cross-over point occurs in both contributions to the first normal stress difference for $Wi \gtrsim 8$, but at different points in an oscillation cycle. The secondary cross-over point in the hydrodynamic first normal stress difference occurs when $|\dot{\gamma}| \sim \dot{\gamma}_0/2$, whereas this occurs for the Brownian contribution when $|\dot{\gamma}| \sim \dot{\gamma}_0$. As Wi increases, the orientation angle and linear dichroism (Figure 4.13c), indicate a higher degree of alignment along the flow axis. The magnitude of the orientation angle at the maximum strain rate decreases from roughly 13° at $Wi = 4$ to 6° at $Wi = 20$. The linear dichroism increases from approximately 0.5 to 0.7 over the same change in Wi , indicating that the non-equilibrium orientation distribution function is increasingly peaked along the flow axis. Furthermore, we can qualitatively observe that the orientation angle is dominated by the Brownian shear stress whereas the linear dichroism is dominated by the Brownian first normal stress difference (see equations (4.25) and (4.26)).

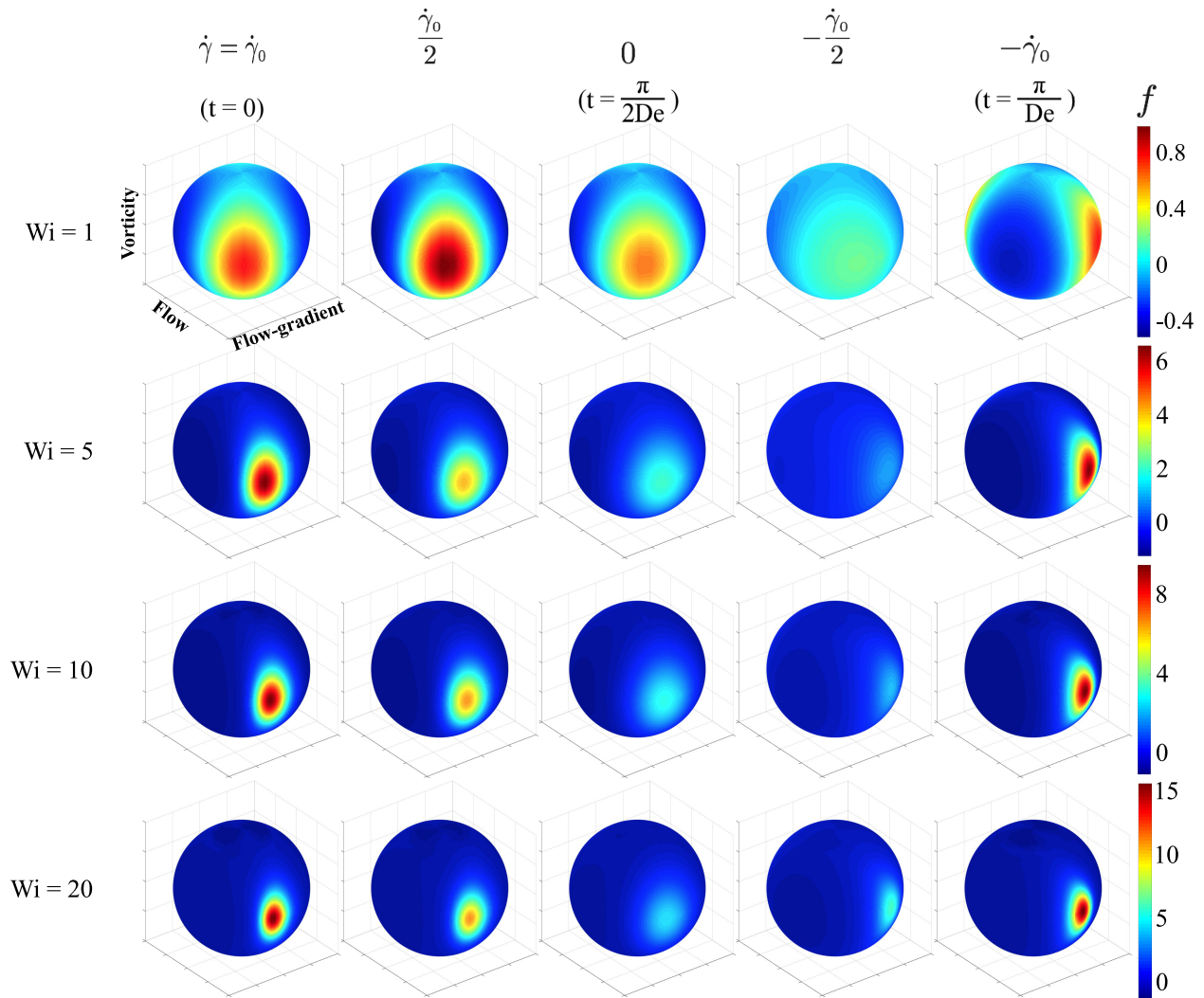


Figure 4.11: Non-equilibrium orientation distribution function in the non-linear viscoelastic regime at different instances in the strain-rate over a half-cycle, $t = [0, \pi/De]$ for $De = 1$ and $Wi = [1, 20]$. Regions of red indicate likely orientations whereas regions of blue indicate unlikely orientations. As Wi increases, the degree of alignment along the flow-axis is enhanced and the particles are almost entirely aligned along the flow axis, as would be expected from their Jeffery orbit trajectories.

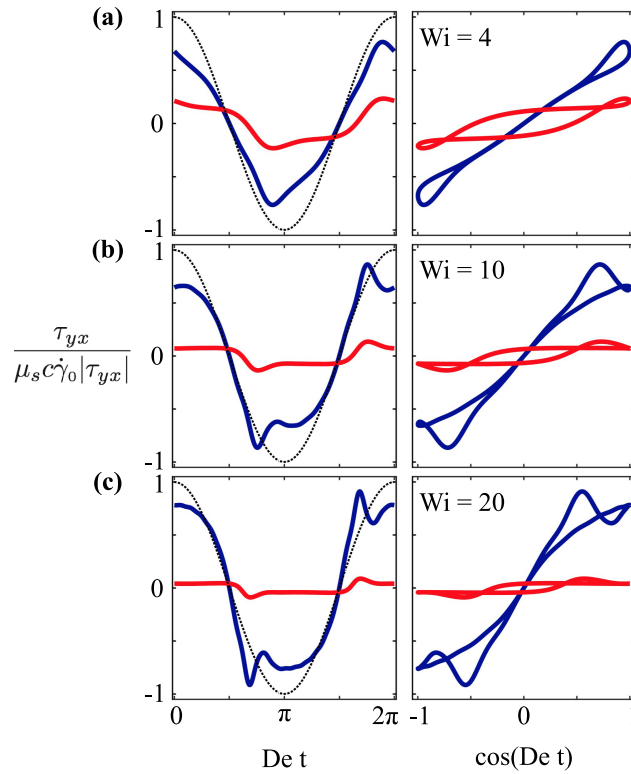


Figure 4.12: Normalized shear stress at $De = 1$ and **(a)**: $Wi = 4$, **(b)**: $Wi = 10$, and **(c)**: $Wi = 20$ as a function of time (left column) and normalized strain-rate (right column). The shear stress is decomposed into the hydrodynamic (black (blue online)) and Brownian (gray (red online)) contributions. The dotted black line in the left column represents strain-rate for reference. The points of cross-over in the Lissajous plots (right column) correspond to the over-shoots and under-shoots in the shear stress response in the time-domain (left column). Regions in the Lissajous plots where the shear stress contributions have a finite projection area correspond to the response in the time-domain being out-of-phase with the imposed strain-rate.

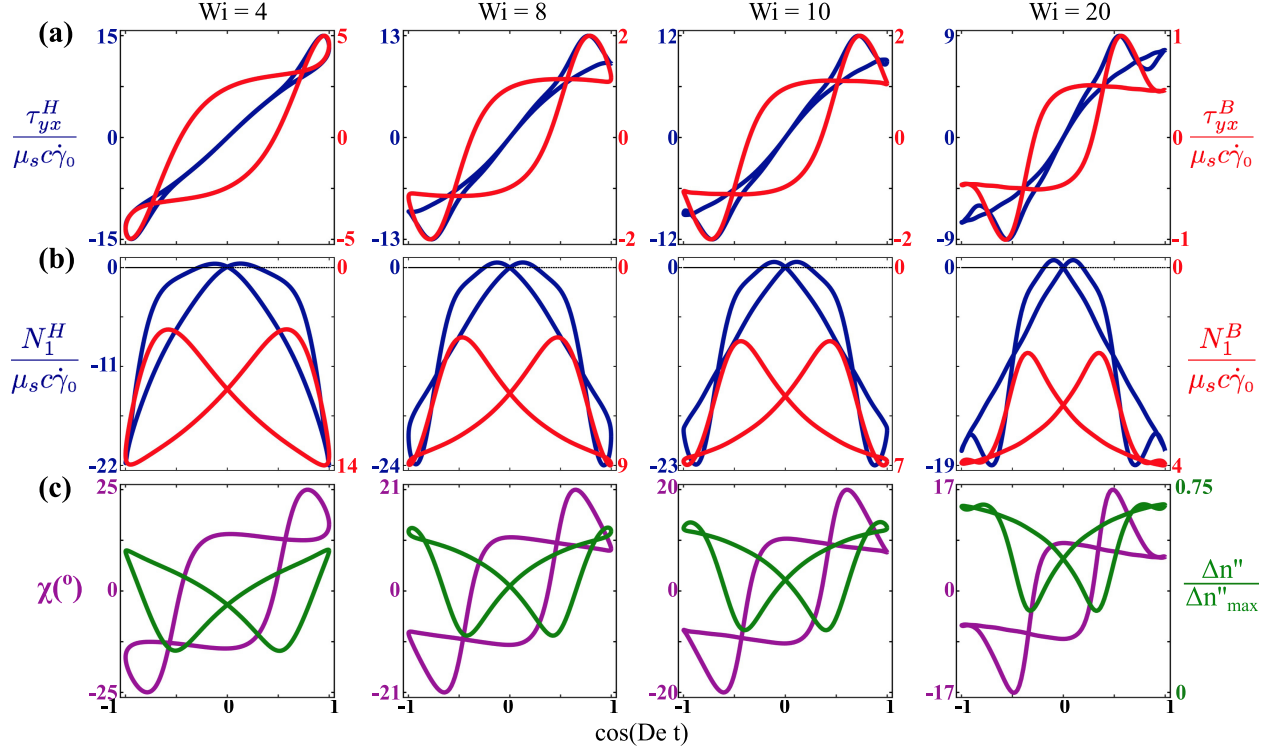


Figure 4.13: Lissajous plots of (a): the shear stress, decomposed into the hydrodynamic (black (blue on-line)) and Brownian (gray (red online)) contributions; (b): first normal stress difference, decomposed into the hydrodynamic (black (blue online)) and Brownian (gray (red online)) contributions; and (c): orientation angle (purple) and linear dichroism (green) for $Wi = [1, 20]$ and $De = 1$. Secondary loops in the shear stress and first normal stress are observed for $Wi \geq 4$; tertiary loops are only observed in the hydrodynamic contributions to the shear stress and first normal stress difference for $Wi \geq 10$. The magnitude of the average orientation angle decreases as Wi increases, whereas the linear dichroism increases, supporting the notion that the particles are increasingly aligned with the flow. Qualitatively, the orientation angle closely resembles the Brownian shear stress whereas the linear dichroism resembles the Brownian first normal stress difference.

4.5 Discussion

We have numerically solved the Fokker-Planck equation for a dilute suspension of Brownian spheroids in a Newtonian fluid subject to an oscillatory shear flow of varying flow strength (Wi) and oscillation frequency (De). The resultant non-equilibrium orientation distribution function was then utilized to calculate the hydrodynamic and Brownian contributions to the shear stress and normal stress differences and the average orientation angle and linear dichroism, as would be measured from a birefringence experiment. Our numerical approach has allowed us to probe a significant portion of the $Wi - De$ parameter space for the case of prolate spheroids of aspect ratio

$r = 20$; our approach can be applied generally to spheroids of any aspect ratio, however. Next, we will discuss the nonlinear viscoelastic regime and explain the microstructural origins of multiple crossover points in the Lissajous-Bowditch plots of the shear stress response. We will then compare our results for prolate spheroids of aspect ratio $r = 20$ to that of oblate spheroids of aspect ratio $r = 1/20 = 0.05$. Finally, we will discuss the overall impact of this work.

Cross-over points in the Lissajous plots of the shear stress versus strain-rate have been observed in a variety of soft materials such as xanthum gum solutions and inverted-micelle drilling fluids¹⁴³, a thermoreversible nanoparticle gel¹⁴⁴, and micelle solutions^{37,145} along with constitutive equations such as the single-mode Geisekus model^{73,146,147}, a non-affine network model¹⁴⁸, and a tube-based model for entangled polymers¹⁴⁹. The origin of cross-over points has been physically interpreted as significant changes in the microstructure¹⁴³. Figure 4.14 gives a complete picture of the microstructure, stress response, and rheo-optical response for a dilute suspension of Brownian rods ($r = 20$) under a large-amplitude oscillatory shear deformation for $Wi = 20$ and $De = 1$. Figure 4.14(a) shows snapshots of the microstructure, parameterized by the non-equilibrium orientation distribution function, at four points in an oscillation half-cycle, where two stress over-shoots are observed in the hydrodynamic stress response. The four quadrants of Figure 4.14(a) correspond to the four discrete points numbered in Figure 4.14(b-e), which will be referred to as “time points 1–4”.

At time point 1, the flow vanishes ($\dot{\gamma} = 0$), the microstructure begins to relax via rotational Brownian motion, and the hydrodynamic stress is zero. However, the Brownian stress is non-zero, but qualitatively appears to be decaying analogous to what one would observe in a cessation experiment. The relaxation of the microstructure results in a decrease in the magnitude of the linear dichroism corresponding to an decrease in the degree of alignment of particles. A slight increase in the orientation angle is also observed as the particles are no longer being driven to align along the flow axis. At the very next instance in time, the flow restarts, but in the opposite direction from the previous half-cycle.

At time point 2, the flow is roughly at 50% of its maximum amplitude ($|\dot{\gamma}| \sim 0.5$, $Det \sim$

$7\pi/10$). With the inception of the flow and reversal in its directionality, the particles have transitioned from an average orientation angle of $\approx 8^\circ$ to an average orientation angle of $\approx -17^\circ$ (Figure 4.14f), as they are driven to align along the flow axis, which is now $\phi = \pi$ (-x axis). Now the particles are more mis-aligned, i.e. further from 0° , than they were at time point 1, which contributes to the stress over-shoot observed between time points 1 and 2. The linear dichroism increases beyond time point 2 as the strain-rate increases, indicating increased degree of alignment (Figure 4.14g). This dramatic change in the microstructure causes the first over-shoot in the hydrodynamic stress (Figure 4.14b,c). The increase in the magnitude of the strain-rate and dramatic change in the average orientation angle is also the origin of the over-shoot in the Brownian stress response.

At time point 3, the flow is roughly at 75% of its maximum amplitude ($|\dot{\gamma}| \sim 0.75$, $Det \sim 4\pi/5$). Here, the average orientation angle (Figure 4.14f) has nearly decreased to its minimum magnitude of $\sim 7^\circ$ and the linear dichroism (Figure 4.14g) is roughly at its maximum value, indicating the strongest alignment about the average orientation angle. A decrease in the hydrodynamic shear stress is observed, resulting from the fact that more of the particles are aligned near the flow axis thus generating less of a disturbance to the flow. The Brownian shear stress has also decreased because the contribution of rotational Brownian motion is dampened by the strength of the flow. Between time points 2 and 3 a maximum in the magnitude of both the hydrodynamic and Brownian first normal stress difference occurs due to the over-alignment of the particles, as is observed in the shear stress overshoot.

At time point 4, the flow is approximately at its maximum amplitude, and a secondary maximum in the magnitude of the hydrodynamic shear stress, hydrodynamic first normal stress difference, and Brownian first normal stress difference occur. Interestingly, a slight decrease and then recovery is observed in the linear dichroism (Figure 4.14g) indicating that some particles briefly become less aligned with the flow; an analogous change is observed in the Brownian first normal stress difference (Figure 4.14e) between time points 3 and 4. At time point 2 the non-equilibrium orientation distribution function is approximately 0 at $\phi \approx 0$ (+x axis). Then, further along at time

point 3 the orientation distribution function has a small, but finite contribution near $\phi = 0$, which increases slightly when moving to time point 4. This corresponds to a small, but non-negligible probability of an ensemble of particles transitioning from the average orientation angle, χ , to a different angle that is of opposite sign and close to zero. This second transition creates a disturbance to the flow, resulting in a secondary overshoot in the hydrodynamic shear stress and first normal stress difference. No discernible change is observed in the Brownian shear stress or average orientation angle between time points 3 and 4.

This secondary transition is similar to spheroidal particles undergoing a Jeffery orbit under steady shear flow in the absence of Brownian motion. Jeffery orbits occur in steady shear because the imposed flow generates a torque on the surface of a particle, but the particle is rigid and cannot deform so it must rotate in order to remain torque-free; the period of rotation is $T_{JO} = 2\pi(r + r^{-1})/\dot{\gamma}_0$. Here, the period of a Jeffery orbit is comparable to the period of an oscillation cycle, $T_{JO}/T_{osc} = (r + r^{-1})De/Wi = 1.0025$. Under these conditions we are allowing for sufficient time for these Jeffery orbit-like events to occur; specifically, one orbit can occur before the flow reverses. Furthermore, it is worth mentioning the striking similarities between the Brownian first normal stress difference in 4.14(e) and the total first normal stress difference calculated by Khair⁷³ from a singular perturbation solution to the single-mode Giesekus model under LAOS. As mentioned in Section 4.2.4.2.1, for $B \approx 1$, the evolution of the Brownian stress via $\langle \mathbf{pp} \rangle$, is dependent upon the upper convected derivative of $\langle \mathbf{pp} \rangle$, analogous to the evolution of the total stress in the Giesekus model, as a particle is equally affected by the vorticity and straining component of the flow. Thus, this leads to the single overshoots in the Brownian first normal stress difference herein and the total first normal stress difference from the Giesekus model (see Figure 4 of Khair⁷³).

An analogous phenomena has been described for a dilute suspension of nearly spherical particles ($|r - 1| \ll 1$) under a large-amplitude oscillatory shear flow¹³⁰, where the total shear stress response undergoes rapid oscillations and multiple cross-over points near $|\dot{\gamma}| \simeq 1$. Here, $T_{JO}/T_{osc} \approx 2De/Wi \ll 1$, allowing for multiple orbits to occur over an oscillation cycle, and thus multiple crossover points in the shear stress, which is dampened by Brownian rotation. Further-

more, the evolution of the Brownian stress, which is dominant over the hydrodynamic contribution ($F_H \gg A_H, B_H, C_H$ for $r \sim 1$ ¹²), depends on the co-rotational derivative of $\langle \mathbf{pp} \rangle$ for $B \approx 0$. The existence of multiple cross-over points in the stress response is thus expected for any co-rotational microstructure that is not oriented by the straining component of the flow

The numerical approach provided herein for solving the Fokker-Planck equation subject to an oscillatory shear deformation can be applied to spheroids of any aspect ratio. To illustrate this, Figure 4.15 shows the non-equilibrium orientation distribution function over a half-cycle for $Wi = 10$ and $De = 1$ for prolate spheroids ($r = 20$) and oblate spheroids ($r = 0.05$). The results for prolate spheroids are the same as in Figure 4.11. Both types of particles align in such a way to minimize the disturbance to the imposed flow and thus minimize the stress of the suspension. This results in prolate spheroids aligned along the flow axis and oblate spheroids aligned along the flow-gradient axis. For both cases, the particles are mainly aligned in the flow-gradient plane with little distribution along the vorticity direction.

The shear stress, decomposed into hydrodynamic and Brownian contributions, for $Wi = 10$ and $De = [0.5, 100]$ is given for both types of particles in Figure 4.16. For both prolate and oblate particles, the hydrodynamic contribution to the shear stress is dominant over the Brownian contribution, with the exception of when the strain-rate is small, $\dot{\gamma} \sim 0$, where the hydrodynamic contribution vanishes but the Brownian contribution does not. Qualitatively, the Brownian contribution to the shear stress for an oblate spheroid suspension is similar to that of a prolate spheroid suspension. Quantitatively the two differ by roughly a factor of 5, which can be attributed to the difference in the relevant scalar hydrodynamic coefficient, $F_H(r)$, ($F_H(r = 20)/F_H(r = 0.05) \approx 4.9$)¹². When $De \sim O(1)$, differences are observed in the hydrodynamic shear stress contribution for oblate and prolate particles. The prolate suspension tends to have an increased degree of hydrodynamic viscoelasticity, meaning that the area projection is larger compared to that of the oblate suspension.

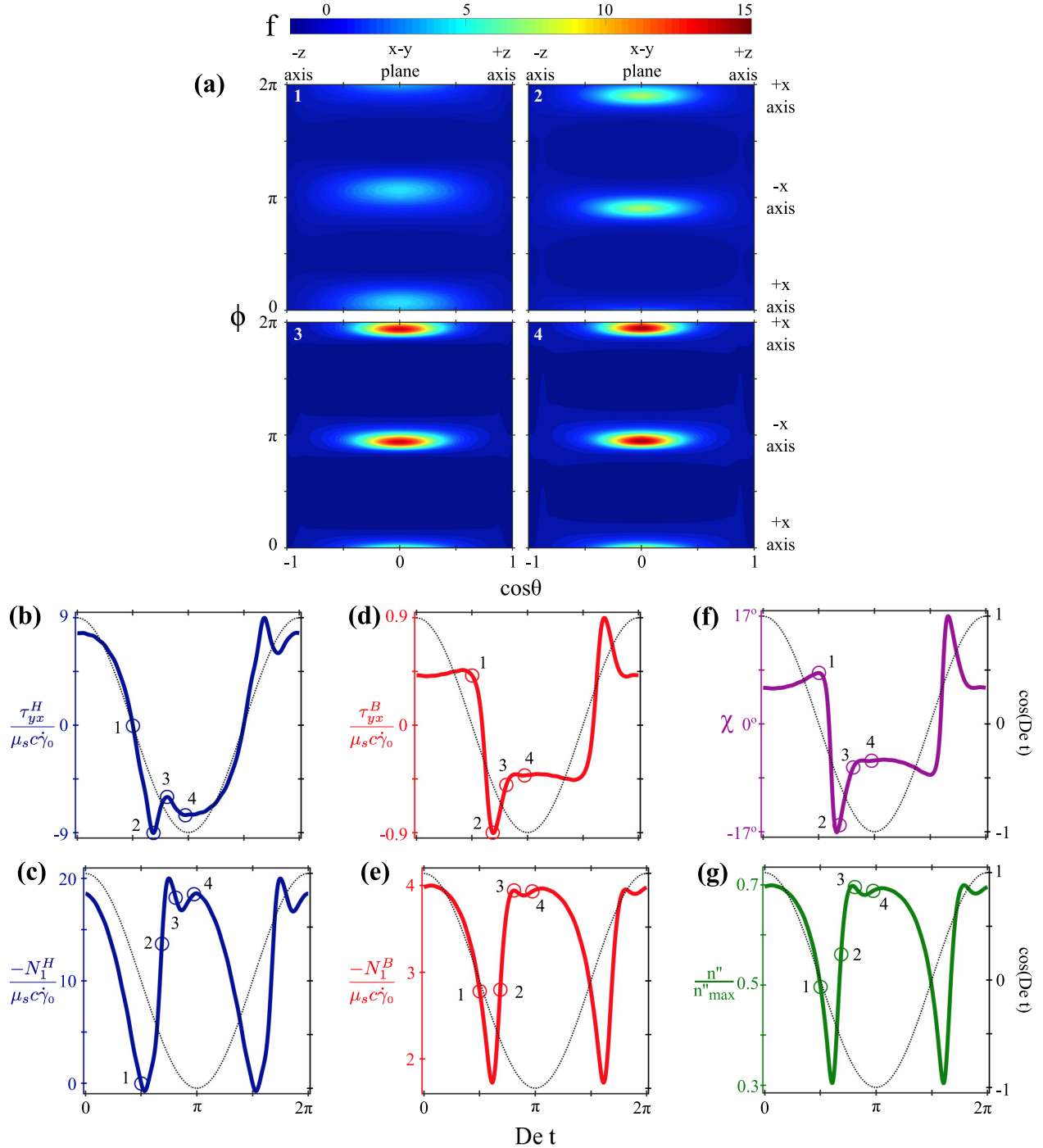


Figure 4.14: Microstructural origins of stress over-shoot: (a): Non-equilibrium orientation distribution function in spherical coordinates, (b): hydrodynamic shear stress, (c): hydrodynamic first normal stress difference, (d): Brownian shear stress, (e): Brownian first normal stress difference, (f): average orientation angle, and (g): linear dichroism for $Wi = 20$ and $De = 1$. The orientation distribution function in each quadrant of (a) corresponds to the numerically labeled point on (b-g).

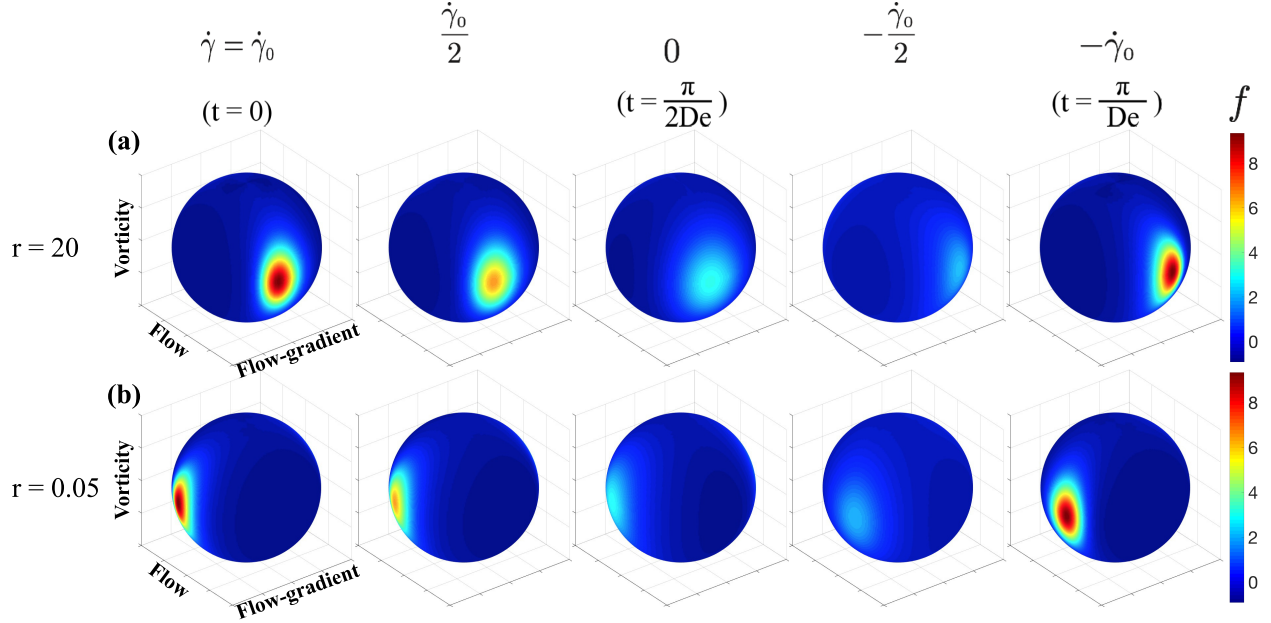


Figure 4.15: Microstructure at $Wi = 10$ and $De = 1$ for **(a)**: prolate spheroid suspension, $r = 20$ and **(b)**: $r = 0.05$. The prolate particles will orient themselves about the flow axis under a sufficiently strong deformation. Conversely, oblate objects will orient themselves along the flow-gradient axis.

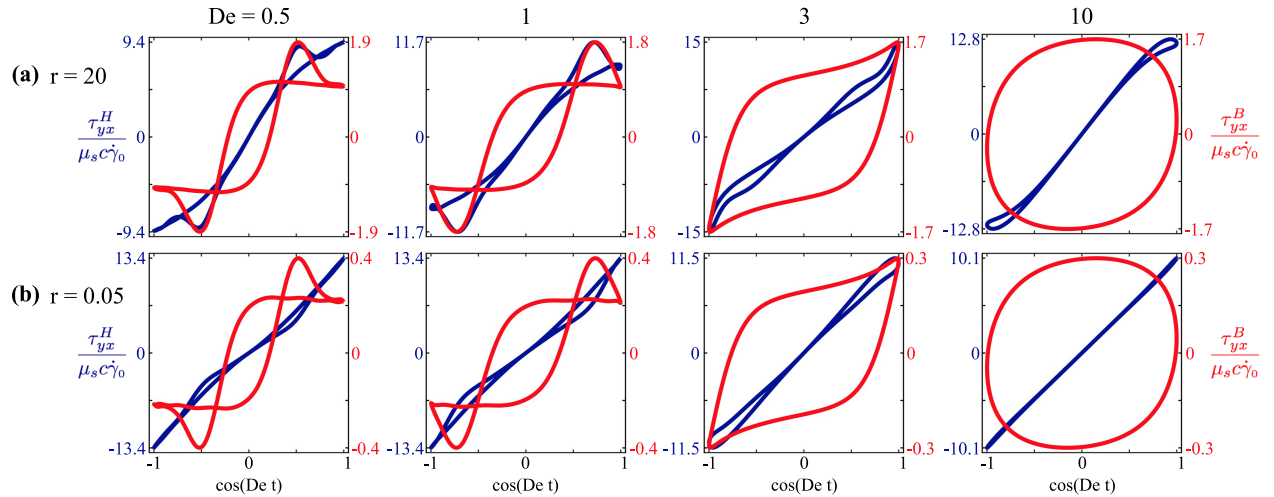


Figure 4.16: Hydrodynamic (black, blue online) and Brownian (gray, red online) shear stress for **(a)** a prolate spheroid suspension, $r = 20$, and **(b)** an oblate spheroid suspension, $r = 0.05$, for $Wi = 10$ over a range of De .

In conclusion, we have demonstrated a general numerical approach to solving the Fokker-Planck equation for a dilute suspension of Brownian spheroids subject to an oscillatory shear flow over a wide range Wi and De . Specifically for the case of prolate spheroids of aspect ratio $r = 20$, we have calculated the full stress tensor along with the birefringence quantities, the linear dichro-

ism and average orientation angle. This work provides a novel microstructural insight into the nonlinear viscoelasticity of suspensions of rigid anisotropic particles. This type of insight is generally valuable because many complex fluids are utilized under strong, transient deformations. LAOS can be viewed as a series of shear start-up and cessation shear flows. However, the microstructure at each start-up in the oscillation cycle does not start from equilibrium, but contains some memory of the previous oscillation cycle. Thus, LAOS is a tool complimentary to a steady shear start-up or cessation flow where the microstructure is beginning at equilibrium or allowed to full relax to equilibrium, respectively, where one can probe the affects of memory on the stress response of a material. The full potential of LAOS can be achieved by combining the technique with other microstructural probes, such as birefringence measurements, SANS, or Raman spectroscopy, to name a few. Specifically, we have shown that the birefringence results provide valuable insight into the Brownian, or entropic nature, of the material. Here, the linear dichroism is qualitatively providing a measure of the Brownian first normal stress differences whereas the average orientation angle is providing a measure of the Brownian shear stress contribution. The combination of the birefringence and LAOS results allow for one to experimentally decouple the hydrodynamic and Brownian stress contributions, which cannot be done by either technique alone. Furthermore, this can analogously be applied to simultaneous SANS measurements. In this case, the alignment factor (typically denoted as A_f ⁴⁰) would now give a qualitative measure of the Brownian first normal stress difference.

4.A Appendix

4.A.1 Expressions for normal stress differences and birefringence parameters

Below are expressions for the normal stress differences and birefringence parameters, average orientation angle and linear dichroism, when the non-equilibrium orientation distribution function

is expanded as a Fourier series in time (see equation (4.27)). The first normal stress difference is,

$$N_1 = -\frac{1}{4\pi} \sum_{\ell=-\infty}^{\infty} \left[\left(e^{i(\ell+1)Det} + e^{i(\ell-1)Det} \right) A_H \int \sin^4 \theta \sin 4\phi f^\ell dS \right. \\ \left. + e^{i\ell Det} \left(\frac{F_H}{3Wi} \int \sin^2 \theta \sin 2\phi f^\ell dS \right) \right]. \quad (4.44)$$

The second normal stress difference is,

$$N_2 = \frac{1}{2\pi} \sum_{\ell=-\infty}^{\infty} \left[\left(e^{i(\ell+1)Det} + e^{i(\ell-1)Det} \right) \left(A_H \int \sin^2 \theta \sin 2\phi (\cos^2 \theta - \sin^2 \theta \sin^2 \phi) f^\ell dS \right. \right. \\ \left. \left. + B_H \int \sin^2 \theta \sin 2\phi f^\ell dS \right) + e^{i\ell Det} \left(\frac{F_H}{6Wi} \int (\cos^2 \theta - \sin^2 \theta \sin^2 \phi) f^\ell dS \right) \right]. \quad (4.45)$$

The linear dichroism is,

$$\frac{\Delta n''}{\Delta n''_{max}} = \sqrt{L_1^2 + L_2^2}. \quad (4.46)$$

The average orientation angle is,

$$\tan 2\chi = \frac{L_1}{L_2}, \quad (4.47)$$

where,

$$L_1 = \frac{1}{4\pi} \sum_{\ell=-\infty}^{\infty} \left[e^{i\ell Det} \int \sin^2 \theta \sin 2\phi f^\ell dS \right], \quad (4.48)$$

and

$$L_2 = \frac{1}{4\pi} \sum_{\ell=-\infty}^{\infty} \left[e^{i\ell Det} \int \sin^2 \theta \cos 2\phi f^\ell dS \right]. \quad (4.49)$$

4.A.2 Convergence and Condition of Numerical Solution Method

The numerical method detailed in Section 4.3 is an iterative approach in that the number of spatial nodes in β and ϕ (N and M , respectively) and the number of temporal nodes (L) necessary to accurately prescribe the non-equilibrium orientation distribution function in (4.28), for a given Wi , De , and r , are not known *a priori*. We deem a numerical solution to (4.28) converged when the addition of spatial and temporal nodes results in a less than 1% relative change in the total shear stress. This is achieved as follows for a fixed r , Wi , and De . An initial guess for the number of spatial nodes, N_0 and M_0 , and temporal nodes, L_0 are chosen either from a previously converged solution at the same Wi and larger De or a previously converged solution at the same De and smaller Wi . Using the initial discretization scheme, the orientation distribution function, f_0 , is calculated and then employed to calculate the total shear stress, τ_{yx}^0 . Next, the number of spatial nodes is increased, $N = N_0 + \zeta$ and $M = M_0 + \zeta$, and the orientation distribution function, f , and shear stress, τ_{yx} , are calculated. This is repeated until the relative error in the total shear stress is below a given tolerance limit: $\text{error} = \|\tau_{yx}^0 - \tau_{yx}\| / \|\tau_{yx}^0\| \leq \text{tol}$, where $\|x\|$ represents the 2-norm. We refer to this intermediate solution as the “spatially converged solution.” Then, while holding the number of spatial nodes fixed at N and M , an additional temporal node is added, $L = L_0 + 1$, and the orientation distribution function, f , and total shear stress, τ_{yx} , are calculated. If the relative error between the new total shear stress and spatially converged total shear stress is less than the prescribed tolerance limit, the solution is deemed converged. However, if the addition of a temporal node resulted in a relative error between the new total shear stress and spatially converged total shear stress that is greater than the prescribed tolerance, the solution is not converged and the process must be restarted with $N_0 = N$, $M_0 = M$, and $L_0 = L$.

Once a converged solution is obtained for a given Wi and De , that discretization scheme (N , M , and L) are employed as the starting point for a solution to (4.28) for the same r and either the same Wi and smaller De or the same De and larger Wi (in the $De \gg 1$ regime). This is schematically depicted in Figure 4.17. The process described here is repeated until the entirety of the $Wi - De$ parameter space has been investigated. For prolate spheroids of aspect ratio $r = 20$,

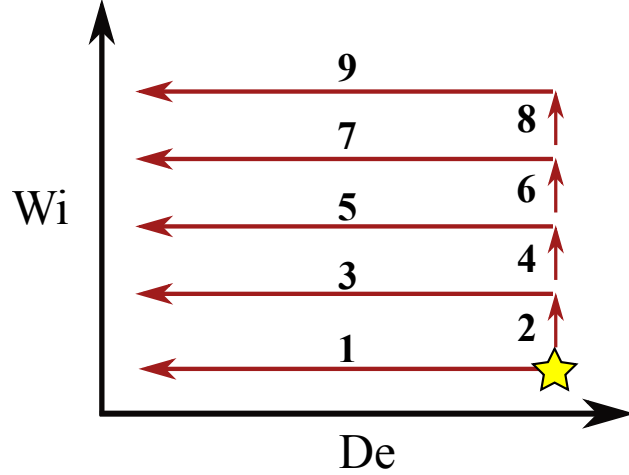


Figure 4.17: Schematic of the solution methodology for solving (4.28) for a fixed r over a range of Wi and De , which can be interpreted chronologically from 1 – 9, beginning at the yellow star. A solution is first obtained at small Wi ($Wi \sim 1$) and large De ($De > 10$). That discretization scheme is then used at the same Wi and smaller De . Once the entire range of De has been probed, the solution at the largest De is then used to probe the next value of Wi .

that parameter space is $Wi = [1, 20]$ and $De = [0.01, 100]$; little variation in mechanical response is observed outside of these ranges.

As mentioned in Section 4.3, the orientation distribution function in (4.14) can be expanded in the basis of spherical harmonics. This approach was utilized for a dilute, rigid dumbbell suspension ($B = 1$) in steady shear^{94,135} and the start-up of steady shear⁹⁶. Strand et al.⁹⁶ were limited by the system size (i.e. number of terms in the spherical harmonics expansion) and the value of Wi . For instance, Strand et al.⁹⁶ found that for $Wi = 10$ and 30 spherical harmonics terms (960 matrix elements), the condition number of the matrix system was $\approx 10^{16}$, which is ill-conditioned. A matrix is considered ill-conditioned if the condition number is larger than the reciprocal of floating-point accuracy; here that limit is $\approx 4.5 \times 10^{15}$. Conversely, the numerical approach detailed here is well-conditioned for significantly larger system sizes. Figure 4.18 shows the condition number for $Wi = 10$ as a function of De . As De decreases, the system size increases, mainly due to an increased number of terms required in the Fourier series expansion (L). At $De = 0.01$, which we have demonstrated to be in the quasi-steady viscoelastic regime, the condition number of our matrix system is roughly 10 orders of magnitude less than the reciprocal of floating-point accuracy (2×10^5 compared to 4.5×10^{15}), and is thus well-conditioned; here, our matrix system size is

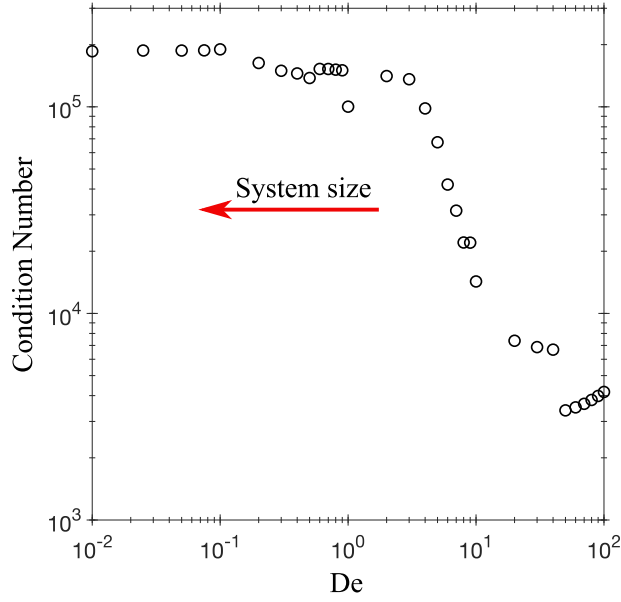


Figure 4.18: Condition number for $Wi = 10$ as function of De . As De decreases, the system size, $NM(L + 1)$, increases as does the condition number. However, the system remains well-conditioned as the condition number is, at minimum, 10 orders of magnitude less than the reciprocal of floating-point accuracy $\approx O(10^{15})$.

136,648 ($N = 58$, $M = 62$, and $L = 37$).

5. Summary

We calculate the transient rheology of a micro-mechanical model suspension of rigid, Brownian spheroids in a Newtonian fluid. The model suspension is homogeneous and dilute, such that interparticle hydrodynamic interactions are negligible. The microstructure, or orientation dynamics of the particles, is characterized via an orientation probability distribution function, which quantifies the likelihood of particle possessing a given orientation at an instance in time. The orientation distribution function satisfies the Fokker-Planck equation, which is a conservation equation balancing the effects of the memory of the material, advection from the flow, and rotary Brownian motion. From the statistical description of the microstructure, the macroscopic stress response of the model suspension is calculated via ensemble averages of the stresslet, weighted by the orientation distribution function. We solve the Fokker-Planck equation using regular perturbation theory and a numerical method to ultimately calculate the stress response of the model suspension under varying flow strengths and oscillation frequencies.

In Chapter 2²⁴ we calculated the linear viscoelasticity of a dilute suspension of self-propelled rigid spheroids under a SAOS deformation using regular perturbation theory. The microstructure of this material relaxes via two independent mechanisms: correlated tumbling events and rotational Brownian motion. This leads to an increased rate of stress relaxation, relative to a suspension that relaxes by either mechanism alone. We explicitly calculate the non-equilibrium orientation distribution function, which is a function of the SAOS deformation, rotational Brownian motion, and correlated tumbling events, via a regular perturbation expansion about $Wi \ll 1$. From this, we calculate the orientationally-averaged shear stress response in the linear viscoelastic regime, which arises from the imposed flow, rotational diffusion, and self-propulsion. Through a comparison of our linear viscoelastic results to a theoretical prediction of the steady shear viscosity of active, slender rods²⁵, we propose a modified Cox-Merz rule for active suspensions. Finally, we demonstrate that linear viscoelastic measurements of active suspensions can be used to determine the mechanism of self-propulsion (pusher or puller), the strength of self-propulsion (i.e. thrust force

generated), and correlation between tumbling events; this is achieved through a comparison of our linear viscoelastic results and experimental results for the steady shear viscosity of *E. coli*⁵², using the proposed modified Cox-Merz rule.

In Chapter 3³¹ we describe a framework for determining the first nonlinear, or MAOS, relaxation modulus of a viscoelastic material from a dual-frequency oscillatory shear deformation. Knowledge of the MAOS relaxation modulus of a material allows one to predict the weakly nonlinear stress response of the material through a memory integral expansion³⁰. We demonstrate this framework using the micro-mechanical model system of a dilute suspension of Brownian spheroids in a Newtonian medium. We determine the second normal stress difference of a simple viscoelastic fluid subject to a dual-frequency MAOS deformation from a co-rotational memory integral expansion. Next, the stress response of the model system is calculated through the ensemble average of the stresslet, wherein the orientation distribution function is calculated via a regular perturbation expansion about $Wi \ll 1$. An analytical expression for the MAOS relaxation modulus of the micro-mechanical system is resolved through a comparison of the second normal stress difference of the model system and the co-rotational memory integral expansion. Finally, we employ the MAOS relaxation modulus to reconstruct the stress response of the model system in the start-up and cessation of steady shear and uniaxial extension.

In Chapter 4 we numerically calculate the nonlinear viscoelasticity of a dilute suspension of Brownian spheroids subject to a LAOS deformation. The orientation distribution function is calculated by numerically solving the Fokker-Planck equation through a finite difference method in space and a Fourier series in time, thus quantifying the long-time periodic behavior of the material. The entire stress tensor and birefringence parameters, average orientation angle and linear dichroism, are then calculated. We apply our numerical method over a range of Wi and De for prolate spheroids of $r = 20$; however, our approach is general and applicable to other values of the aspect ratio. We showcase results in four viscoelastic regimes: linear viscoelastic ($Wi \ll 1$), quasi-linear viscoelastic ($Wi > 1$ and $Wi/De \ll 1$), quasi-steady viscoelastic ($Wi \gtrsim 1$ and $De \ll 1$), and the nonlinear viscoelastic regime ($Wi \gtrsim 1$ and $Wi/De \gtrsim 1$). In the nonlinear viscoelastic regime,

specifically $Wi \gg 1$ and $De \sim O(1)$, multiple overshoots are observed in the hydrodynamic stress response of the material. We demonstrate that the origin of these secondary (and potentially additional) overshoots are through microstructural rearrangements similar to a particle undergoing a Jeffery orbit under steady shear in the absence of Brownian motion; this is done by analyzing the microstructure, stress response, and birefringence parameters simultaneously for $Wi = 20$ and $De = 1$. In this example, the period of a Jeffery orbit is comparable to the period of an oscillation cycle, thus allowing sufficient time for a single Jeffery orbit to occur per oscillation cycle. Finally, we provide results for oblate spheroids of $r = 0.05$ and compare these to the results of $r = 20$. The Brownian stress of both suspensions is qualitatively similar, differing only by a scalar factor of roughly 5; this arises from the ratio of the relevant aspect ratio-dependent hydrodynamic coefficient, $F_H(r = 20)/F_H(r = 0.05) \approx 4.9$. However, a suspension of oblate spheroids tends to have a smaller hydrodynamic contribution to the viscoelastic stress compared to a suspension of prolate particles, indicating that the oblate spheroids create less of a disturbance to the imposed flow, compared to prolate spheroids with equal $|B|$.

5.1 Future Work

Simple shear is not the only linear flow that can be used to probe nonlinear viscoelasticity. One can also employ an extensional deformation, such as a planar or uniaxial extensional flow, where a viscoelastic material is stretched (or compressed), either in two or three dimensions^{17,150–152}. Extensional flows are highly efficient at stretching flexible polymer molecules and orienting rigid particles, as there is no rotational component to flow¹⁵¹. Thus, one would expect a markedly different response of a viscoelastic material under an extensional flow compared to a simple shear flow. A natural extension of this thesis would be to calculate the nonlinear viscoelasticity of the micro-mechanical model system detailed herein under a large amplitude oscillatory extensional (LAOE) deformation. This can be achieved by adapting the analysis described in Chapter 4 to an oscillatory uniaxial extensional flow with velocity field $\mathbf{v} = \dot{\epsilon}_0 \cos(De t) (-x \mathbf{e}_x - y \mathbf{e}_y + 2z \mathbf{e}_z)$, where $\dot{\epsilon}_0$ is the extension amplitude (analogous to the shear-rate amplitude). Thus, we can define

an extensional Weissenberg number, $Wi_E = \dot{\epsilon}_0/6D_r$. In steady extensional flow, a particle will align along the extensional axis, as it is a stable fixed point (attractor) in the orientation space. This is distinctly different from steady simple shear, where a (non-Brownian) particle undergoes a periodic Jeffery orbit, i.e. there are no fixed points in this case. Furthermore, oscillatory extension is fundamentally different from steady extension as the stable fixed points are destroyed as the velocity field oscillates. Thus, the nonlinear viscoelastic response of a suspension of rigid, axisymmetric particles in oscillatory extension will be markedly different from oscillatory simple shear and steady extension.

Another continuation of this work would be to expand the micro-mechanical model from rigid particles to a deformable microstructure that is capable of stretching, like a polymer molecule would. The extensibility of the microstructure is a new degree of freedom, in addition to the orientation distribution. For instance, the elastic dumbbell model describes a polymer molecule as two mass-less beads connected by a spring⁶; the dumbbell is orientable and able to stretch via the spring. The dynamics of polymer molecules in LAOE has been recently explored in the single polymer^{153,154} and semi-dilute polymer regimes^{155,156}, by optically measuring the extension of single-stranded DNA in an oscillatory planar extensional flow. A simple model of these experiments would be achieved by solving a conservation equation, analogous to the Fokker-Planck equation, for a probability distribution function, which quantifies the likelihood of the beads at a separation distance, r , where both the orientation and magnitude of r can vary. This conservation equation balances the memory of the material, orientation by the imposed flow, rotational Brownian motion, and now an entropic spring force, which quantifies the extensibility of the microstructure. A key goal would be to compare the cycle-averaged extension of a particle, or an ensemble of particles, predicted from this model to the above mentioned experiments.

References

- [1] Mewis, J.; Wagner, N. J. *Colloidal Suspension Rheology*; Cambridge University Press: New York, NY, 2012.
- [2] Mewis, J.; Metzner, A. B. *Journal of Fluid Mechanics* **1974**, *62*, 593.
- [3] Solomon, M. J.; Spicer, P. T. *Soft Matter* **2010**, *6*, 1391.
- [4] Jogun, S. M.; Zukoski, C. F. *Journal of Rheology* **1999**, *43*, 847–871.
- [5] Bird, R. B.; Warner, H. R.; Evans, D. C. *Fortschritte der Hochpolymeren-Forschung. Advances in Polymer Science*; Springer: Berlin, Heidelberg, 1971; Vol. 8; pp 1–90.
- [6] Bird, R. B.; Hassager, O.; Armstrong, R. C.; Curtiss, C. F. *Dynamics of Polymeric Liquids Vol 2: Kinetic Theory*, 1st ed.; John Wiley & Sons: New York, NY, 1977.
- [7] Bird, R. B.; Giacomin, A. J.; Schmalzer, A. M.; Aumate, C. *The Journal of Chemical Physics* **2014**, *140*, 074904.
- [8] Schmalzer, A.; Bird, R.; Giacomin, A. *Journal of Non-Newtonian Fluid Mechanics* **2015**, *222*, 56–71.
- [9] Jeffery, G. *Proceedings of the Royal Society of London* **1922**, *102*, 161–179.
- [10] Leal, L. G.; Hinch, E. J. *Journal of Fluid Mechanics* **1971**, *46*, 685–703.
- [11] Hinch, E. J.; Leal, L. G. *Journal of Fluid Mechanics* **1972**, *52*, 683–712.
- [12] Kim, S.; Karrila, S. J. *Microhydrodynamics: Principles and Selected Applications*; Dover: Mineola, New York, 2005.
- [13] Brenner, H.; Condiff, D. W. *Journal of Colloid and Interface Science* **1974**, *47*, 199–264.
- [14] Batchelor, G. K. *Journal of Fluid Mechanics* **1970**, *41*, 545–570.

- [15] Hinch, E. J.; Leal, L. G. *Journal of Fluid Mechanics* **1976**, *76*, 187–208.
- [16] Dealy, J. M.; Wang, J. *Melt Rheology and Its Role in Plastics Processing*, 2nd ed.; Springer Science+Business Media: New York, NY, 2013.
- [17] Macosko, C. *Wiley-VCG*, 1st ed.; Wiley-VCH: New York, 1994.
- [18] Ebbens, S. J.; Howse, J. R. *Soft Matter* **2010**, *6*, 726.
- [19] Hong, Y.; Velegol, D.; Chaturvedi, N.; Sen, A. *Phys. Chem. Chem. Phys.* **2010**, *12*, 1423–1435.
- [20] Patra, D.; Sengupta, S.; Duan, W.; Zhang, H.; Pavlick, R.; Sen, A. *Nanoscale* **2013**, *5*, 1273–1283.
- [21] Dey, K. K.; Wong, F.; Altemose, A.; Sen, A. *Current Opinion in Colloid & Interface Science* **2016**, *21*, 4–13.
- [22] Schwarz-Linek, J.; Arlt, J.; Jepson, A.; Dawson, A.; Vissers, T.; Miroli, D.; Pilizota, T.; Martinez, V. A.; Poon, W. C. *Colloids and Surfaces B: Biointerfaces* **2016**, *137*, 2–16.
- [23] Teo, W. Z.; Pumera, M. *Chemistry - A European Journal* **2016**, 1–10.
- [24] Bechtel, T. M.; Khair, A. S. *Rheologica Acta* **2017**,
- [25] Saintillan, D. *Experimental Mechanics* **2010**, *50*, 1275–1281.
- [26] López, H. M.; Gachelin, J.; Douarche, C.; Auradou, H.; Clément, E. *Physical Review Letters* **2015**, *115*, 028301.
- [27] Kalman, D. P.; Merrill, R. L.; Wagner, N. J.; Wetzel, E. D. *ACS Applied Materials & Interfaces* **2009**, *1*, 2602–2612.
- [28] Cwalina, C. D.; McCutcheon, C. M.; Dombrowski, R. D.; Wagner, N. J. *Composites Science and Technology* **2016**, *131*, 61–66.

- [29] Melito, H. S.; Daubert, C. R.; Foegeding, E. a. *Journal of Food Process Engineering* **2013**, *36*, 521–534.
- [30] Bird, R. B.; Armstrong, R. C.; Hassager, O. *Dynamics of Polymeric Liquids. Volume 1: Fluid Mechanics*, 2nd ed.; Wiley-Interscience Publications: New York, NY, 1987.
- [31] Bechtel, T. M.; Khair, A. S. *Journal of Rheology* **2017**, *61*, 67–82.
- [32] Grosso, M.; Maffettone, P. L. *Journal of Non-Newtonian Fluid Mechanics* **2007**, *143*, 48–58.
- [33] Hyun, K.; Baik, E. S.; Ahn, K. H.; Lee, S. J.; Sugimoto, M.; Koyama, K. *Journal of Rheology* **2007**, *51*, 1319–1342.
- [34] Sugimoto, M.; Suzuki, Y.; Hyun, K.; Hyun Ahn, K.; Ushioda, T.; Nishioka, A.; Taniguchi, T.; Koyama, K. *Rheologica Acta* **2006**, *46*, 33–44.
- [35] Klein, C. O.; Spiess, H. W.; Calin, A.; Balan, C.; Wilhelm, M. *Macromolecules* **2007**, *40*, 4250–4259.
- [36] Férec, J.; Heuzey, M.; Ausias, G.; Carreau, P. *Journal of Non-Newtonian Fluid Mechanics* **2008**, *151*, 89–100.
- [37] Gurnon, A. K.; Wagner, N. J. *Journal of Rheology* **2012**, *56*, 333.
- [38] Dimitriou, C. J.; Casanellas, L.; Ober, T. J.; McKinley, G. H. *Rheologica Acta* **2012**, *51*, 395–411.
- [39] Rogers, S. A.; Calabrese, M. A.; Wagner, N. J. *Current Opinion in Colloid & Interface Science* **2014**, *19*, 530–535.
- [40] Calabrese, M. A.; Rogers, S. A.; Porcar, L.; Wagner, N. J. *Journal of Rheology* **2016**, *60*, 1001–1017.

- [41] Neidhofer, T.; Sioula, S.; Hadjichristidis, N.; Wilhelm, M. *Macromolecular Rapid Communications* **2004**, *25*, 1921–1926.
- [42] Kline, T. R.; Paxton, W. F.; Mallouk, T. E.; Sen, A. *Angewandte Chemie* **2005**, *117*, 754–756.
- [43] Dhar, P.; Cao, Y.; Kline, T.; Pal, P.; Swayne, C.; Fischer, T. M.; Miller, B.; Mallouk, T. E.; Sen, A.; Johansen, T. H. *The Journal of Physical Chemistry C* **2007**, *111*, 3607–3613.
- [44] Sundararajan, S.; Lammert, P. E.; Zudans, A. W.; Crespi, V. H.; Sen, A. *Nano Letters* **2008**, *8*, 1271–1276.
- [45] Tjhung, E.; Cates, M. E.; Marenduzzo, D. *Soft Matter* **2011**, *7*, 7453–7464.
- [46] Stenhammar, J.; Marenduzzo, D.; Allen, R. J.; Cates, M. E. *Soft Matter* **2014**, *10*, 1489–1499.
- [47] Takatori, S. C.; Yan, W.; Brady, J. F. *Physical Review Letters* **2014**, *113*, 028103.
- [48] Spagnolie, S. E., Ed. *Complex Fluids in Biological Systems*; Biological and Medical Physics, Biomedical Engineering; Springer New York: New York, NY, 2015.
- [49] Lauga, E.; Powers, T. R. *Reports on Progress in Physics* **2009**, *72*, 096601.
- [50] Rafai, S.; Jibuti, L.; Peyla, P. *Physical Review Letters* **2010**, *104*, 098102.
- [51] Mussler, M.; Rafai, S.; Peyla, P.; Wagner, C. *Europhys. Lett.* **2013**, *101*, 54004.
- [52] Gachelin, J.; Miño, G.; Berthet, H.; Lindner, A.; Rousselet, A.; Clément, É. *Physical Review Letters* **2013**, *110*, 268103.
- [53] Sokolov, A.; Aranson, I. S. *Physical Review Letters* **2009**, *103*, 148101.
- [54] Turner, L.; Ryu, W. S.; Berg, H. C. *Journal of Bacteriology* **2000**, *182*, 2793–2801.

- [55] Haines, B. M.; Aronson, I. S.; Berlyand, L.; Karpeev, D. A. *Physical Biology* **2008**, *5*, 046003.
- [56] Hatwalne, Y.; Ramaswamy, S.; Rao, M.; Simha, R. A. *Physical Review Letters* **2004**, *92*, 118101.
- [57] Bozorgi, Y.; Underhill, P. T. *Rheologica Acta* **2014**, *53*, 899–909.
- [58] Cox, W. P.; Merz, E. H. *Journal of Polymer Science* **1958**, *28*, 619–622.
- [59] Al-Hadithi, T. S. R.; Barnes, H. A.; Walters, K. *Colloid & Polymer Science* **1992**, *270*, 40–46.
- [60] Subramanian, G.; Koch, D. L. *Journal of Fluid Mechanics* **2009**, *632*, 359.
- [61] S., C.; T, C. *The Mathematical Theory of Non-Uniform Gases*; Cambridge University Press, 1991.
- [62] DA, M. *Statistical Mechanics*; University Science Books, 2000.
- [63] Saintillan, D.; Shelley, M. J. *Physics of Fluids* **2008**, *20*, 123304.
- [64] Abdel-Khalik, S. I.; Hassager, O.; Bird, R. B. *The Journal of Chemical Physics* **1974**, *61*, 4312–4316.
- [65] Bird, R. B. *Annual Review of Physical Chemistry* **1977**, *28*, 185–206.
- [66] Chattopadhyay, S.; Moldovan, R.; Yeung, C.; Wu, X. L. *Proceedings of the National Academy of Sciences* **2006**, *103*, 13712–13717.
- [67] Trueba, F. J.; Woldringh, C. L. *Journal of bacteriology* **1980**, *142*, 869–78.
- [68] Wu, M.; Roberts, J. W.; Kim, S.; Koch, D. L.; DeLisa, M. P. *Applied and Environmental Microbiology* **2006**, *72*, 4987–4994.

- [69] Barnes, H.; Hutton, J.; Walters, K. *An Introduction to Rheology*; Elsevier Science Publishers: Amsterdam, The Netherlands, 1993; Vol. 1.
- [70] Hyun, K.; Kim, S. H.; Ahn, K. H.; Lee, S. J. *Journal of Non-Newtonian Fluid Mechanics* **2002**, *107*, 51–65.
- [71] Hyun, K.; Wilhelm, M.; Klein, C. O.; Cho, K. S.; Nam, J. G.; Ahn, K. H.; Lee, S. J.; Ewoldt, R. H.; McKinley, G. H. *Progress in Polymer Science* **2011**, *36*, 1697–1753.
- [72] Swan, J. W.; Zia, R. N.; Brady, J. F. *Journal of Rheology* **2014**, *58*, 1–41.
- [73] Khair, A. S. *Journal of Rheology* **2016**, *60*, 257–266.
- [74] Pearson, D. S.; Rochefort, W. E. *Journal of Polymer Science: Polymer Physics Edition* **1982**, *20*, 83–98.
- [75] Bae, J.-E.; Cho, K. S. *Journal of Rheology* **2015**, *59*, 525–555.
- [76] Langela, M.; Wiesner, U.; Spiess, H. W.; Wilhelm, M. *Macromolecules* **2002**, *35*, 3198–3204.
- [77] Oelschlaeger, C.; Gutmann, J. S.; Wolkenhauer, M.; Spiess, H.-W.; Knoll, K.; Wilhelm, M. *Macromolecular Chemistry and Physics* **2007**, *208*, 1719–1729.
- [78] Zhou, L.; Cook, L.; McKinley, G. H. *Journal of Non-Newtonian Fluid Mechanics* **2010**, *165*, 1462–1472.
- [79] DePuit, R. J.; Squires, T. M. *Journal of Physics: Condensed Matter* **2012**, *24*, 464106.
- [80] Goddard, J. D. *Transactions of the Society of Rheology* **1967**, *11*, 381–399.
- [81] Noll, W. *Archive for Rational Mechanics and Analysis* **1958**, *2*, 197–226.
- [82] Giesekus, H. *Journal of Non-Newtonian Fluid Mechanics* **1982**, *11*, 69–109.
- [83] Bharadwaj, N. A.; Ewoldt, R. H. *Journal of Rheology* **2014**, *58*, 891–910.

- [84] Swan, J. W.; Furst, E. M.; Wagner, N. J. *Journal Of Rheology* **2014**, *58*, 307–337.
- [85] Helmholtz, H. *On the Sensations of Tone*; Dover: Mineola, New York, 1957.
- [86] Roederer, J. G. *The Physics and Psychophysics of Music*, 4th ed.; Springer Science+Business Media: New York, NY, 2008.
- [87] Parthasarathy, M.; Klingenberg, D. J. *Journal of Non-Newtonian Fluid Mechanics* **1999**, *81*, 83–104.
- [88] Hyun, K.; Nam, J. G.; Wilhelm, M.; Ahn, K. H.; Lee, S. J. *Rheologica Acta* **2006**, *45*, 239–249.
- [89] Zhao, Y.; Haward, S. J.; Shen, A. Q. *Journal of Rheology* **2015**, *59*, 1229–1259.
- [90] Green, A. E.; Rivlin, R. S.; Spencer, A. *Archive for Rational Mechanics and Analysis* **1959**, *3*, 82–90.
- [91] Coleman, B. D.; Noll, W. *Reviews of Modern Physics* **1961**, *33*, 239–249.
- [92] Pipkin, A. C. *Reviews of Modern Physics* **1964**, *36*, 1034–1041.
- [93] Bird, R. B.; Hassager, O.; Abdel-Khalik, S. I. *AIChE Journal* **1974**, *20*, 1041–1066.
- [94] Stewart, W. E.; Sorensen, J. P. *Transactions of the Society of Rheology* **1972**, *16*, 1–13.
- [95] Leal, L. G.; Hinch, E. J. *Journal of Fluid Mechanics* **1972**, *55*, 745–765.
- [96] Strand, S. R.; Kim, S.; Karrila, S. J. *Journal of Non-Newtonian Fluid Mechanics* **1987**, *24*, 311–329.
- [97] Swan, J. W.; Gurnon, A. K.; Wagner, N. J. *Journal of Rheology* **2016**, *60*, 241–255.
- [98] Brady, J. F. *The Journal of Chemical Physics* **1993**, *99*, 567–581.
- [99] Khair, A. S.; Bechtel, T. M. *Journal of Rheology* **2015**, *59*, 429–471.

- [100] Batchelor, G. K. *Journal of Fluid Mechanics* **1976**, *74*, 1–29.
- [101] Baek, S.-G.; Magda, J. J. *Journal of Rheology* **2003**, *47*, 1249–1260.
- [102] Honerkamp, J.; Weese, J. *Rheologica Acta* **1993**, *32*, 65–73.
- [103] Baumgaertel, M.; Winter, H. H. *Rheologica Acta* **1989**, *28*, 511–519.
- [104] Kamath, V.; Mackley, M. *Journal of Non-Newtonian Fluid Mechanics* **1989**, *32*, 119–144.
- [105] Alcoutlabi, M.; Baek, S. G.; Magda, J. J.; Shi, X.; Hutcheson, S. A.; McKenna, G. B. *Rheologica Acta* **2009**, *48*, 191–200.
- [106] Schweizer, T.; Schmidheiny, W. *Journal of Rheology* **2013**, *57*, 841–856.
- [107] Adams, N.; Lodge, A. *Philosophical Transactions of the Royal Society of London. Series A, Mathematical and Physical Sciences* **1964**, *256*, 149–184.
- [108] Bracewell, R. *Fourier Analysis and Imaging*; Springer, 2003.
- [109] Pipkin, A. In *Lectures on Viscoelasticity Theory*, 2nd ed.; John, F., Marsden, J., Sirovich, L., Eds.; Springer Science+Business Media: New York, NY, 1986.
- [110] Dimitriou, C. J.; McKinley, G. H.; Venkatesan, R. *Energy & Fuels* **2011**, *25*, 3040–3052.
- [111] Dao, M. M.; Domach, M. M.; Walker, L. M. *Journal of Rheology* **2017**, *61*, 237–252.
- [112] Egres, R. G.; Nettekheim, F.; Wagner, N. J. *Journal of Rheology* **2006**, *50*, 685–709.
- [113] Calabrese, M. A.; Wagner, N. J. *Wormlike Micelles*; Royal Society of Chemistry: Cambridge, 2017; pp 193–235.
- [114] Deyrail, Y.; Huneault, M. A.; Bousmina, M. *Journal of Polymer Science Part B: Polymer Physics* **2009**, *47*, 1467–1480.
- [115] Kotula, A. P.; Meyer, M. W.; De Vito, F.; Plog, J.; Hight Walker, A. R.; Migler, K. B. *Review of Scientific Instruments* **2016**, *87*.

- [116] Atalik, K.; Keunings, R. *Journal of Non-Newtonian Fluid Mechanics* **2004**, *122*, 107–116.
- [117] Hatzikiriakos, S. G.; Dealy, J. M. *Journal of Rheology* **1991**, *35*, 497–523.
- [118] Adrian, D. W.; Giacomin, A. J. *Journal of Rheology* **1992**, *36*, 1227–1243.
- [119] Graham, M. D. *Journal of Rheology* **1995**, *39*, 697–712.
- [120] Wilhelm, M. *Macromolecular Materials and Engineering* **2002**, *287*, 83–105.
- [121] Ewoldt, R. H.; Hosoi, a. E.; McKinley, G. H. *Journal of Rheology* **2008**, *52*, 1427.
- [122] Cho, K. S.; Hyun, K.; Ahn, K. H.; Lee, S. J. *Journal of Rheology* **2005**, *49*, 747–758.
- [123] Rogers, S. A.; Erwin, B. M.; Vlassopoulos, D.; Cloitre, M. *Journal of Rheology* **2011**, *55*, 435.
- [124] Giacomin, A.; Bird, R.; Johnson, L.; Mix, A. *Journal of Non-Newtonian Fluid Mechanics* **2011**, *166*, 1081–1099.
- [125] Saengow, C.; Giacomin, A. J.; Kolitawong, C. *Macromolecular Theory and Simulations* **2015**, *24*, 352–392.
- [126] Giacomin, A. J.; Bird, R. B. *Rheologica Acta* **2011**, *50*, 741–752.
- [127] Vlahovska, P.; Blawdziewicz, J.; Loewenberg, M. *Journal of Fluid Mechanics* **2002**, *463*, 1–24.
- [128] Leahy, B. D.; Koch, D. L.; Cohen, I. *Journal of Fluid Mechanics* **2015**, *772*, 42–79.
- [129] Leahy, B. D.; Koch, D. L.; Cohen, I. *Journal of Rheology* **2017**, *61*, 979–996.
- [130] Khair, A. S. *Journal of Fluid Mechanics* **2016**, *791*, R5.
- [131] Bretherton, F. P. *Journal of Fluid Mechanics* **1962**, *14*, 284.
- [132] Brenner, H.; Condiff, D. W. *Journal of Colloid and Interface Science* **1972**, *41*, 228–274.

- [133] Rahnama, M.; Koch, D. L.; Shaqfeh, E. S. G. *Physics of Fluids* **1995**, *7*, 487–506.
- [134] Giesekus, H. *Rheologica Acta* **1962**, *2*, 50–62.
- [135] Bird, R. B.; Warner Jr., H. *Journal of Rheology* **1971**, *15*, 741–750.
- [136] Prager, S. *Transactions of the Society of Rheology* **1957**, *1*, 53–62.
- [137] Hinch, E. J.; Leal, L. G. *Journal of Fluid Mechanics* **1973**, *57*, 753–767.
- [138] Frattini, P. L.; Fuller, G. G. *Journal of Colloid and Interface Science* **1984**, *100*, 506–518.
- [139] Frattini, P. L.; Fuller, G. G. *Journal of Fluid Mechanics* **1986**, *168*, 119–150.
- [140] Fuller, G. G. *Optical rheometry of complex fluid interfaces*; 1995; Vol. 2.
- [141] Vermant, J.; Yang, H.; Fuller, G. G. *AIChE Journal* **2001**, *47*, 790–798.
- [142] Brenner, H. *Journal of Colloid and Interface Science* **1970**, *34*, 103–125.
- [143] Ewoldt, R. H.; McKinley, G. H. *Rheologica Acta* **2010**, *49*, 213–219.
- [144] Kim, Y.; Bénard, A.; Petty, C. A. *Industrial & Engineering Chemistry Research* **2015**, *54*, 4497–4504.
- [145] López-Barrón, C. R.; Porcar, L.; Eberle, A. P. R.; Wagner, N. J. *Physical Review Letters* **2012**, *108*, 258301.
- [146] Ewoldt, R. H.; Winter, P.; Maxey, J.; McKinley, G. H. *Rheologica Acta* **2010**, *49*, 191–212.
- [147] Duvarci, O. C.; Yazar, G.; Kokini, J. L. *Journal of Food Engineering* **2017**, *208*, 77–88.
- [148] Jeyaseelan, R. S.; Giacomini, A. J. *Journal of Non-Newtonian Fluid Mechanics* **2008**, *148*, 24–32.
- [149] Leygue, A.; Bailly, C.; Keunings, R. *Journal of Non-Newtonian Fluid Mechanics* **2006**, *136*, 1–16.

- [150] Anna, S. L.; McKinley, G. H.; Nguyen, D. a.; Sridhar, T.; Muller, S. J.; Huang, J.; James, D. F. *Journal of Rheology* **2001**, *45*, 83–114.
- [151] McKinley, G. H.; Sridhar, T. *Annual Review of Fluid Mechanics* **2002**, *34*, 375–415.
- [152] Odell, J.; Carrington, S. *Journal of Non-Newtonian Fluid Mechanics* **2006**, *137*, 110–120.
- [153] Zhou, Y.; Schroeder, C. M. *Macromolecules* **2016**, *49*, 8018–8030.
- [154] Zhou, Y.; Schroeder, C. M. *Physical Review Fluids* **2016**, *1*, 053301–17.
- [155] Hsiao, K.-W.; Sasmal, C.; Ravi Prakash, J.; Schroeder, C. M. *Journal of Rheology* **2017**, *61*, 151–167.
- [156] Sasmal, C.; Hsiao, K.-W.; Schroeder, C. M.; Ravi Prakash, J. *Journal of Rheology* **2017**, *61*, 169–186.